# NMR Investigation of Quantum Thermodynamics and Quantum Correlations

A thesis

Submitted in partial fulfillment of the requirements of the degree of

## Doctor of Philosophy

by

**Soham Pal**

Registration ID-20142023



Department of Physics

INDIAN INSTITUTE OF SCIENCE EDUCATION AND RESEARCH

PUNE-411008, India

June 18, 2021

# Certificate

Certified that the work incorporated in the thesis entitled **"NMR Investigation of Quantum Thermodynamics and Quantum Correlations"** submitted by **Soham Pal** was carried out by the candidate, under my supervision. The work presented here or any part of it has not been included in any other thesis submitted previously for the award of any degree or diploma from any other university or institution.

Date: June 7, 2021

Prof. T.S. Mahesh

(Supervisor)

# Declaration

I declare that this written submission represents my ideas in my own words and where others ideas have been included, I have adequately cited and referenced the original sources. I also declare that I have adhered to all principles of academic honesty and integrity and have not misrepresented or fabricated or falsified any idea/data/fact/source in my submission. I understand that violation of the above will be cause for disciplinary action by the Institute and can also evoke penal action from the sources which have thus not been properly cited or from whom proper permission has not been taken when needed.

Date: June 18, 2021

Soham Pal

(20142023)

# Acknowledgments

I would like to start by thanking my supervisor, Prof. T. S. Mahesh, for his almost unconditional support in academics for the past six years. His unending zeal for science and research, and his overall attitude towards life is something that I can confidently say inspires everyone in our NMR-QIP lab. He is a kind of mentor who brings out the best in his students. I consider myself fortunate to have had him as my supervisor.

I would like to thank my Research Advisory Committee members, who are also my collaborators, Dr. Bijay Kumar Agarwalla and Dr. G. J. Sreejith, for all their support and help. Dr. Bijay has been like a second mentor to me, and I thank him for teaching almost everything I know about quantum thermodynamics. His door is always open for a student with question and I plead guilty of taking advantage of this. He is truly a remarkable teacher and researcher. I am grateful to Dr. G. J. Sreejith for all the curious discussions we had on non-equilibrium systems. His immense knowledge and concepts in condensed matter physics have been a huge help during my PhD. It was a pleasure collaborating with Dr. Rejish Nath and Prof. Tomesz Paterek (Uniwersytet Gdański). Their expertise in their respective fields was indispensable in the projects we undertook and I thank them for being very patient and considerate with me. I would also like to thank my first collaborator, Prof. Anil Kumar (IISc, Bangalore), under whose guidance I undertook my first PhD research project.

I have had the pleasure of sharing NMR-QIP lab with some of the very kind and helpful labmates one can hope for. Seniors like Dr. Abhishek Shukla, Dr. Rupak Bhattacharya, Dr. Sudheer, Dr. V. S. Anjusha and Dr. Deepak Khurana have always been there extending a helping hand whenever needed. I am also glad to have shared the lab with very kind and bright colleagues like V. R. Krithika, Priya Batra, Conon Alexander, Arijit Chatterjee and Jitendra Joshi. Thanks to the NMR facility technicians Nitin Dalvi and Dr. Sandeep for their tireless effort in maintaining a pristine NMR facility and helping with hardware whenever needed.

PhD life can at times be a bit too much, but if one surrounds him/herself with the right people, he/she is guaranteed to have some of the most cherished memories in life. I had the pleasure of

# Abstract

Thermodynamics provides a systematic study of the thermal properties of macroscopic systems by establishing relationships between various physical quantities like heat, temperature, internal energy, entropy, etc. These relations help one quantify the various thermal attributes of the system in question and enable us to design and control systems of our choice. But with the advent of quantum mechanics the size of the system of interest is shrinking, and with this it is imperative that we understand the behaviour of the above mentioned thermodynamic quantities in the quantum regime as well. Quantum thermodynamics tries to bridge the gap between two fields of physics, thermodynamics and quantum mechanics, which are separated by a period of about a century in their origin.

One can say, the field of modern thermodynamics started with Sadi Carnot's work on engine efficiency in his publication "Reflection on the Motive Power of heat" in 1824. Quite similarly, it can be argued that the study of contemporary quantum thermodynamic started in 1959, when Scovil and Schulz found the equivalence of a three-level maser with Carnot heat engine. This was followed by people trying to define and understand the various thermodynamic quantities in the quantum domain. Today, with the advancements of experimental techniques in quantum mechanics it is possible to probe and control a wide variety of quantum systems with ever increasing size and complexities. One can now use experimental systems, like NV centres, trapped atoms/ions, Nuclear Magnetic Resonance (NMR) etc., to study the thermodynamic properties like heat, work, entropy in a wide range of quantum mechanical systems, giving way to experimental realization and investigation of quantum thermodynamics.

This thesis is based on the use of ensemble nuclear magnetic resonance of molecular spin registers with sizes varying from two to thirty-seven qubits, to understand the thermodynamic properties, like time-crystalline behaviour, and thermodynamic relations, like heat-exchange fluctuation relation and thermodynamic uncertainty relations (TURs), of out of equilibrium quantum systems, their quantum many-body effects and their interplay with quantum correlations. It has now long been known that quantum information can be used as a resource to perform work on

quantum systems. Here we try to experimentally observe the kind of effect these quantum correlations can have in the process of heat flow between two qubits, and investigate its localization in a classically mediated quantum correlation transfer. We also use the NMR spin registers to investigate the newly discovered time crystalline behaviour and show the robust period-two oscillations of the spins under error-some driving.

# Synopsis

With the advancements in the experimental techniques in quantum mechanical systems, it is now possible to probe and control a wide variety of quantum systems with ever increasing sizes and complexities. One can now use these experimental systems, like Nitrogen Vacancy (NV) centres, trapped atoms, Nuclear Magnetic Resonance (NMR) etc., to study the thermodynamic properties like heat, work, entropy in a wide range of quantum mechanical systems, giving way to the experimental realisation and investigation of the field of Quantum thermodynamics. Quantum thermodynamics tries to bridge the gap between two independent theories of physics: Quantum Mechanics and Thermodynamics. In this thesis we report the experiments done using NMR spin Qubits, of varying sizes, to better understand the relationship between the, above mentioned, thermodynamic quantities in the quantum regime and their interplay with quantum correlations and quantum information. We also explore the recently discovered and interesting property of many-body thermodynamic property of stability of discrete time-crystalline order in driven many-body quantum systems, known as the *Time crystals*, and localization of entanglement in some quantum-classical systems.

## Chapter 1 − Introduction

In chapter 1 we introduce the concepts and terminology we use in this thesis describing the quantum information processing (QIP) and its implementation in Nuclear Magnetic resonance to realise the quantum thermodynamic phenomena discussed in the subsequent chapters. We start with defining a quantum bit, or a *qubit*, which forms the basic building block of quantum information processing. This is followed by a more thorough discussion of a qubit's properties, form and various ways one can manipulate it. Further, we delve into the role played by information in thermodynamics and some of the basic concepts involved. Finally we end the chapter with demonstration of the NMR implementation of some quantum information processing techniques.

## Chapter 2 − Quantum heat-exchange fluctuation relation

Most of the equalities we come across between thermodynamic quantities are for systems which are at equilibrium or very near to equilibrium. In 1996, Christopher Jarzynski put forward an equality, relating the difference in free energy and exponential average of the work performed on an out-of-equilibrium system. Since then a number of such equalities have been put forward for non-equilibrium thermodynamic systems. These relations are collectively referred to the *fluctuation relations* (FR). These FRs are valid under certain assumptions made about the transient system in question. In this chapter we experimentally explore the validity of one such fluctuation, called the Jarzynski and Wójcik FR for heat-exchange between two quantum systems using liquid-state NMR setup. We further introduce quantum correlations into the system and show the apparent reversal of flow of heat.

## Chapter 3 − **Thermodynamic Uncertainty Relations**

Heisenberg's uncertainty relation provides a lower bound to the extent to which we can measure observables like position and momentum simultaneously. Along the same lines one can also think of a bound for thermal fluctuations in heat flow between quantum systems. These bounds are now called the Thermodynamic Uncertainty Relations (TURs). In the last few years people have extensively explored these theoretical bounds quantifying the extent of fluctuations entailed in the quantum heat exchange process. In this chapter, we experimentally study a few of these TURs in a two-qubit system, for the first time, using a liquid-NMR setup and explore the regions of validity and violation of these relations in various parameter regimes.

## Chapter 4 − **Experimental localisation of quantum entanglement through monitored classical mediator**

lIn recent works (e.g. PRL 119, 240401 or PRL 119, 240402) entanglement gain between two objects interacting via mediator has been proposed as a witness of the non-classical mediator. In chapter 4 we show that this conclusion depends on the initial state of the whole tripartite system. Using nuclear magnetic resonance techniques on a nuclear spin quantum register, we experimentally prepare an initial state whose later dynamics give rise to entanglement gain via a classical mediator. To emphasize the strong notion of classicality we have also dephased the mediator during dynamics. We are convinced this work will have major implications in quantum optome-

chanics, quantum biology, and quantum gravity.

**Chapter 5 − Discrete Time Crystalline behaviour in NMR spin systems**

One of the very curious properties of out-of-equilibrium driven quantum systems is their recently discovered robust period two oscillation of the magnetization, which led to the observation of a new phase of matter known as the *Time crystals*. Since its conception in 2012 by the Frank Wilczek, tremendous amount of work, both theoretically and experimentally, has been done towards understanding this exotic behaviour. In this chapter we experimentally study the response of star-shaped clusters of initially unentangled nuclear spin-$\frac{1}{2}$ moments in solid and liquid NMR samples to an inexact $\pi$-pulse sequence, and show that an Ising coupling between the centre and the satellite spins in the liquids and long-range dipolar coupling in solids, result in robust period-two magnetization oscillations.

# List of Publications

1. **Soham Pal**, Naveen Nishad, T S Mahesh, and G J Sreejith , *Temporal Order in Periodically Driven Spins in Star-Shaped Clusters,* Phys. Rev. Lett. 120, 180602 (2018).

2. **Soham Pal**, T. S. Mahesh, and Bijay Kumar Agarwalla,  *Experimental demonstration of the validity of the quantum heat-exchange fluctuation relation in an NMR setup*Phys. Rev. A 100, 042119 (2019).

3. **Soham Pal**, Sushant Saryal, Dvira Segal, T. S. Mahesh, and Bijay Kumar Agarwalla *Experimental study of the thermodynamic uncertainty relation,* Phys. Rev. Research 2, 022044(R) (2020).

4. **Soham Pal**, Priya Batra, Tanjung Krisnanda, Tomasz Paterek, and T. S. Mahesh, *Experimental localisation of quantum entanglement through monitored classical mediator,* Quantum 5, 478 (2021)

5. **Soham Pal**, Saranyo Moitra, V S Anjusha, Anil Kumar, and T S Mahesh , *Hybrid scheme for factorisation: Factoring 551 using a 3-qubit NMR quantum adiabatic processor,* Pramana volume 92, Article number: 26 (2019).

6. V. R. Krithika, **Soham Pal**, Rejish Nath, and T. S. Mahesh, *Observation of interaction induced blockade and local spin freezing in a NMR quantum simulator*, arXiv:2005.04445 (2020). Accepted in *Phys. Rev. Res.*.

7. B. Sharmila, V. R. Krithika, **Soham Pal**, T. S. Mahesh, S. Lakshmibala and V. Balakrishnan, *Tomographic entanglement indicators from NMR experiments,*, arXiv:2105.08555 (2021).

# Contents

# CHAPTER 1

## Introduction

*Necessity is the mother of inventions*, and quantum mechanics is no exception to this. Quantum mechanics came about at the turn of the twentieth century, as a theory to rescue the troubled souls from a plethora of inconsistencies in the physical theories, like '*ultraviolet catastrophe*', electrons in an atom spiralling down into its nucleus, etc. And with it also came our potential to understand and manipulate the *very very small* physical systems with astounding accuracy. Richard Feynman, in his exemplary 1959 seminar at the annual meeting of American Physical Society, [1], talked about what it meant to go down to the atomic levels, how the laws there are nothing like ours at large scale and how one can use the *quantisation* of energy levels and the interactions between these quantum particles, like *spins*, to make things like a circuit and even a computer. In 1980s, he and Yuri Manin independently went even further and pointed out that a classical Turing machine would take exponentially long time and resources to simulate a quantum system and the right way to go about it would be to use a quantum system to do so. He famously said '*There is plenty of room at the bottom*', foreshadowing the marvels that were to be achieved in the next half a century.

Today almost all the tech. giants of the world are spearheading their research and development to realize a universal quantum computer, to declare a clear *quantum supremacy* [2]. But why do we need a quantum computer? The answer very much depends upon whom you ask, but for a scientists interested in understanding the dynamics of quantum systems, a quantum computer is a tool to simulate quantum systems to learn and thus develop new quantum technologies. These quantum technologies use the fundamental laws of quantum mechanics, governing these sub atomic systems, to realize devices which in turn have far reaching practical implications in real world. One such area of research is the study of the thermodynamic properties of these quantum systems, which help us to not only answer some very fundamental questions about the connection between the two completely different theories in Physics, quantum mechanics and thermodynamics, but it also paves the way to realize various thermodynamic machines and tech-

nologies, like heat engine, refrigerators, thermal diodes, batteries, etc. in the quantum domain. Trapped ions, neutral atoms, quantum dots, super-conducting qubits, nitrogen vacancy centres, are some of the experimental architectures today being used as a test bed to simulate and study quantum systems and their behaviours. The two main requirements for an experimental architecture to be a possible test bed for quantum simulations are, long *coherence time* and good accessibility to the quantum system or the *qubits*. Although a long coherence time needs the system to be sufficiently decoupled from the surrounding environment, for sufficient control over the qubits, initial state preparation and read-out the system needs to be well coupled to external controls. Nuclear Magnetic Resonance (NMR) is one such experimental test bed, with comparably large coherence time and sufficient accessibility to the qubits, which has been accepted as a suitable platform to perform and incorporate quantum algorithms and tasks [3, 4].

In this thesis we explore some of the thermodynamic properties of these quantum system using the nuclear magnetic resonance (NMR) quantum information processing (QIP) techniques and further see how information and/or *quantum correlations* play the role of resource in these quantum thermodynamic systems. We begin with a brief discussion and pre-requisites for QIP and NMR in this chapter, followed by elaborate descriptions of each project undertaken in subsequent chapters.

## 1.1 Quantum information processing (QIP)

Following Feynman's idea, QIP can be thought of as using the rules set by quantum mechanics, instead of classical physics, to build a framework for handling and manipulating information. Instead of performing operations on a classical bit of information, QIP works with a generalised concept of a bit of information in the quantum world, a quantum bit (Qubit). This way of processing information can be shown not only to be more efficient than its classical analogue, in certain cases [5, 6], but also provides a better and more efficient way to simulate quantum systems. This helps us understand and study the various quantum phenomena, like quantum entanglement, measurement disturbance, particle number statistics etc., and further utilise it in real world. In this section we will start with the notion of quantum bits and how we manipulate them to perform various operations on it.

### 1.1.1 Qubits

In today's digital world we process and store information in bits, which can take only two values. This we assign as the logical 0 and logical 1. Physically this can be realized in any system with two distinct states like two voltage nodes or a transistors two different regions of operation or alignment of a magnetic material. We know that a quantum system with spin-1/2 also has two distinct states. The quantum state of $|0\rangle$ corresponds to logical 0 and $|1\rangle$ corresponds to logical 1. But in contrast to a classical bit, which can take only 0 or 1 state, a quantum two level system, qubit, exhibits the property of *quantum superposition*. Because of this a qubit can exist in a superposition of the two eigenstates $|0\rangle$ and $|1\rangle$. A general state of a qubit can be written as

$$|\psi\rangle = a|0\rangle + b|1\rangle, \tag{1.1}$$

where *a* and *b* are the complex numbers, called the superposition coefficients. These coefficients are such that the state $|\psi\rangle$ is always normalised, $|a|^2 + |b|^2 = 1$. The overall phase of $|\psi\rangle$ is irrelevant as it practically can not be revealed by any experiment. The state can then be written as

$$|\psi\rangle = \cos\frac{\theta}{2}|0\rangle + e^{i\phi}\sin\frac{\theta}{2}|1\rangle, \tag{1.2}$$

which is helpful in visualizing a qubit as a point on the Bloch sphere. Here $\theta$ and $\phi$ are the polar and azimuthal angles as shown in Fig. 1.1. By convention $|0\rangle$ is taken in the +ve *z*-direction. Using $\theta = \pi/2$, for two values of $\phi = 0$ and $\pi/2$ in Eq. 1.2 one can write two important single qubit states, $\frac{|0\rangle+|1\rangle}{\sqrt{2}}$ and $\frac{|0\rangle+i|1\rangle}{\sqrt{2}}$, as shown in Fig. 1.1 as point A and B respectively. It is important to understand that such superposition states are fundamentally different from a classical state in the sense that, instead of pointing along a particular direction a quantum superposition state is both $|0\rangle$ and $|1\rangle$ at the *same time*. This gives rise to *quantum parallelism* which is one of the reasons for the quantum advantage that QIP makes possible. Given the full quantum state, Eq. 1.2, one can write the density matrix which encodes all the information about the state as

$$\begin{aligned}
\rho &= |\psi\rangle\langle\psi| \\
&= \begin{bmatrix} \cos^2\frac{\theta}{2} & \cos\frac{\theta}{2}\sin\frac{\theta}{2}e^{-i\phi} \\ \cos\frac{\theta}{2}\sin\frac{\theta}{2}e^{i\phi} & \sin^2\frac{\theta}{2} \end{bmatrix}.
\end{aligned} \tag{1.3}$$

3

Using trigonometric identities, the above relation can be expressed in terms of Pauli matrices as

$$\rho = \frac{1}{2}(\mathbb{1} + \sin\theta\cos\phi\sigma^x + \sin\theta\cos\phi\sigma^y + \cos\theta\sigma^z)$$
$$= \frac{1}{2}(\mathbb{1} + \hat{n}\cdot\vec{\sigma}), \tag{1.4}$$

where $\hat{n}$ is a unit vector in the Bloch sphere. This is the reason one can imagine a pure state residing on the surface of the Bloch sphere.
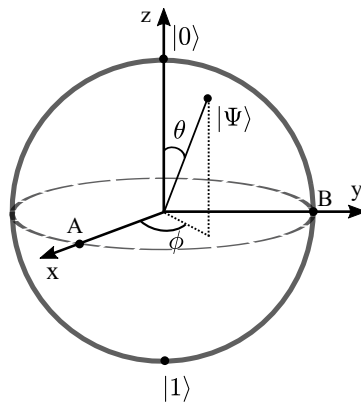


**Figure 1.1:** Bloch sphere representation of the state of a qubit, $|\Psi\rangle$.

#### 1.1.1.1 Multi qubit system

Bloch sphere is an intuitive way to visualize a single qubit state using two variables, $\theta$ and $\phi$. But when dealing with a multi qubit system, where each qubit is in an arbitrary superposition state, one can no longer think of the state as a point sitting on the Bloch sphere. Considering two qubits in their arbitrary normalised states, $|\psi_1\rangle = a_1|0\rangle + b_1|1\rangle$ and $|\psi_2\rangle = a_2|0\rangle + b_2|1\rangle$, one can write the combined two qubit state as the *kronecker product* of the two as

$$|\psi_{12}\rangle = |\psi_1\rangle \otimes |\psi_2\rangle$$
$$= a_1a_2|00\rangle + a_1b_2|01\rangle + b_1a_2|10\rangle + b_1b_2|11\rangle, \tag{1.5}$$

where we have abbreviated $|0\rangle \otimes |0\rangle$ as $|00\rangle$ and so on. The coefficients $a_1a_2$, $a_1b_2$ and others are all arbitrary complex numbers. Along with this, writing the basis state $|00\rangle$, $|01\rangle$ etc. in the

decimal form one can simplify Eq. 1.5 as

$$|\psi_{12}\rangle = \sum_{j=0}^{2^n-1} c_j|j\rangle. \tag{1.6}$$

Here $c_j$ are the complex coefficients, amplitudes, satisfying the condition, $\sum_{j=0}^{2^n-1} |c_j|^2 = 1$. It is very instructive to observe that these amplitudes can take infinitely many values ($c_j \in \mathbb{C}$) and still satisfy the equality in the previous line. This is in stark contrast to the classical case where one can operate only with discrete bits. Thus, in theory, one can store and process exponentially more information using a qubit. We visualise a *n*-qubit quantum state as a point in the $2^n$ dimensional *Hilbert space*, which is an extension of the Block sphere.

### 1.1.1.2 Pure and mixed quantum states

Till now we dealt with quantum systems which are in definite quantum states like, $\psi_i = a_i|0\rangle + b_i|1\rangle$. Such a state is called a pure state as there is no ambiguity about it being in any other state. But if to the best of our knowledge a quantum system is in one of the many pure state, $|\psi_i\rangle$, or is an ensemble of such states with a non-zero probability $p_i$, such a system is said to be in a mixture of pure states, and is called a mixed state. In other words, mixed states are statistical mixture of pure quantum states. When dealing with such mixed quantum states, one often represents the state of the system in the density operator formalism as shown below.

$$\rho = \sum_i p_i|\psi_i\rangle\langle\psi_i|. \tag{1.7}$$

Here $\langle\psi_i|$ is the Hermitian conjugate of the pure state $|\psi_i\rangle$. Naturally the probabilities, $p_i$, satisfy the conditions, $0 \leq p_i \leq 1$ and $\sum_i p_i = 1$. A pure state density matrix can also be written similarly as $\rho = |\psi\rangle\langle\psi|$. A density matrix satisfies the relation $\text{Tr}[\rho] = 1$, as $\text{Tr}[\rho] = \sum_i p_i\text{Tr}[|\psi\rangle\langle\psi|] = \sum_i p_i$. Furthermore, all the eigenvalues, $\lambda_i$ of the density operator have to be positive. Using Eq. 1.6 and 1.7 one can write the decomposition of the density matrix as follows,

$$\rho = \sum_i p_i|\psi_i\rangle\langle\psi_i| = \sum_i p_i \sum_{j,k} c_j c_k^*|j\rangle\langle k| = \sum_{j,k} \overline{c_j c_k^*}|j\rangle\langle k|, \tag{1.8}$$

where $c_k^*$ is the complex conjugate of $c_k$ and $\overline{c_j c_k^*}$ represents ensemble average and are the populations and coherences (discussed later) present in the system. $|j\rangle$ and $|k\rangle$ are orthogonal eigenstates of $\rho$. The spectral decomposition of $\rho$ can further be written in terms of its eigenvalues, $\lambda_i$, as

$$\rho = \sum_i \lambda_i |i\rangle\langle i|. \tag{1.9}$$

This expression shows us that a quantum system in state $\rho$ is basically in a state $|i\rangle$ with probability $\lambda_i$. Mathematically one can distinguish between a pure and a mixed state by noting that, a pure state has only one non-zero eigenvalue (necessarily being 1) and a mixed state has more than one non-zero eigenvalue. A convenient way to distinguish between a pure state and a mixed state is by computing $\mathrm{Tr}[\rho^2]$. If this value comes out to be 1, the system is in a pure quantum state. But if $\mathrm{Tr}[\rho^2] < 1$ the system is in a mixed quantum state. Another important property of the density operator is that it is Hermitian, $\rho^\dagger = \rho$. It can be shown that just as in Eq. 1.4, the single qubit mixed state can still be represented as

$$\rho = \frac{1}{2}(\mathbb{1} + \boldsymbol{n} \cdot \overrightarrow{\boldsymbol{\sigma}}). \tag{1.10}$$

But here the $n$ is no longer a unit vector and the state vector lies inside the Bloch sphere. Thus, where as a single qubit pure state is represented by a point on the Bloch sphere, a single qubit mixed state can be visualized as a point inside the Block sphere.

When dealing with a composite system, $\rho_{AB}$, it is often desirable to look at only a subsystem, say $\rho_A$. The density operator formalism provides a suitable way to do so, maintaining the correct definition of the observables and their measurement statistics for the subsystem, with the help of *reduced density operators*. The reduced density operator does so by defining a map of operators known as the *partial trace*. Consider we have a composite system $\rho_{AB}$, of which we are only interested in the state of $A$. In that case, one writes the reduced density operator for system $A$ as,

$$\rho_A = \mathrm{Tr}_B[\rho_{AB}] = \mathrm{Tr}_B[\sum_{ijkl} c_{ijkl}|a_i\rangle\langle a_j| \otimes |b_k\rangle\langle b_l|]$$

$$= \sum_{ijkl} c_{ijkl}|a_i\rangle\langle a_j|\mathrm{Tr}[|b_k\rangle\langle b_l|] = \sum_{ijk} c_{ijkk}|a_i\rangle\langle a_j|. \tag{1.11}$$

Here we have used the the expression $\mathrm{Tr}[|b_k\rangle\langle b_l|] = \langle b_l|b_k\rangle = \delta_{kl}$. Another use of reduce density operator comes in quantifying the amount of quantum entanglement (discussed in later sections)

in pure composite states. If such a system is in a separable state, the reduced density operator of its subsystems also turn out to be pure states. Whereas, if we have an entangled state, tracing out one of the subsystem reduces the purity of the rest of the system.

### 1.1.1.3 Populations and coherences

In the previous section we saw that density operator formalism provides a convenient way to deal with mixed ensemble of quantum states. The matrix representation of such a density operator is shown in Eq. 1.8. The coefficients, $\overline{c_j c_k^*}$, are the various components of such a density matrix. The diagonal entries can be written as $\sum_j \overline{|c_j|^2} |j\rangle\langle j|$. These real and positive coefficients, $\overline{c_j c_j^*}$, represent the populations of the $j^{th}$ eigenstate, satisfying the relation $\sum_i \overline{c_i c_i^*} = 1$. As all spin-1/2 particles have an intrinsic magnetic moment associated with them, the difference of the population in the two eigenstates of an ensemble of spin-1/2 particles represent the net magnetic polarization, dictated by the direction of the eigenstates. It is important to understand here that the population of an eigenstate does not represent the fraction of spin-1/2 particles in that state. In-fact most of the particles in the ensemble are in the superposition of the eigenstates. This brings us to the discussion of the coherences present in these quantum states. The coefficient of the off-diagonal terms in the density matrix, $\overline{c_j c_k^*}$ where $j \neq k$ represent the average component of the magnetic moment for the particles in the ensemble, orthogonal to the eigenbasis in which the density matrix is represented. These off-diagonal coefficients are called the coherences. Mathematically $kj^{th}$ component of these coefficients can be represented as $\langle k|\rho|j\rangle = \overline{c_j c_k^*}$. Given the Hermiticity of the density operator, coherences satisfy the condition $\langle k|\rho|j\rangle = \langle j|\rho^*|k\rangle$.

These quantum coherences can be classified in terms of their quantum numbers, called *coherence order*. Here we give a very brief discussion of the same. Let us consider $ij^{th}$ coherence term, $\rho_{ij}$, in a quantum state of $\rho$. For simplicity, lets say the system is in a pure state. Thus the coherence term can be written as

$$\rho_{ij} = \langle i|\rho|j\rangle = \langle i||\psi\rangle\langle\psi||j\rangle \tag{1.12}$$

Such a system placed in a high $z$-magnetic field has well-defined eigenstates with eigenvalues, $S_z|i\rangle = M_i|i\rangle$ and $S_z|j\rangle = M_j|j\rangle$. The order of coherence, $m_{ij}$, for $(ij)^{th}$ component of the coherence in such a system is then defined as the difference of the $z$-angular momentum of these

connected $i^{th}$ and $j^{th}$ state. Mathematically this can be written as $m_{ij} = M_i - M_j$.

## 1.1.2 Quantum gates

Any processing require a sequence of steps, which finally achieves a desired effect. In quantum information processing these steps performing a specific task and is referred to as *Quantum Gates*. Since in quantum mechanics, evolution of a quantum state is done by operation of a unitary, which in turn is generated by the Hamiltonian of the system, quantum gates are just unitary evolutions [7, 8]. Just as we have gates in classical information processing like NOT, OR, NOR, XOR etc. which perform their respective operations on a bit or multiple bits, the quantum analogue of such gates operating on quantum states and performing corresponding operations is called a Quantum Gate. In this section we briefly mention the single and two-qubit quantum gates used in this thesis, as it has been shown in [9] that a set of single and two-qubit gates can perform arbitrary multi-qubit unitary operations.

### 1.1.2.1 Single-qubit gates

Single qubit gates are the simplest building blocks of quantum information processing. All single qubit gates can be written as a rotation in the Bloch sphere, $R_{\hat{n}}(\theta)$. This $R_{\hat{n}}(\theta)$ represents a rotation by an angle $\theta$ about a direction $\hat{n} = (n_x, n_y, n_z)$ in the Block sphere, which we define in terms of the Pauli matrices

$$\sigma^x = \begin{bmatrix} 0 & 1 \\ 1 & 0 \end{bmatrix}, \ \sigma^y = \begin{bmatrix} 0 & -i \\ i & 0 \end{bmatrix}, \ \sigma^z = \begin{bmatrix} 1 & 0 \\ 0 & -1 \end{bmatrix}. \tag{1.13}$$

These matrices follow the relations,

$$\sigma^x \sigma^y = i\sigma^z, \ \sigma^y \sigma^z = i\sigma^x, \ \sigma^z \sigma^x = i\sigma^z,$$

$$(\sigma^x)^2 = (\sigma^y)^2 = (\sigma^z)^2 = \sigma_{\mathbb{1}} = \begin{bmatrix} 1 & 0 \\ 0 & 1 \end{bmatrix} \tag{1.14}$$

Using $\vec{\sigma} = (\sigma^x, \sigma^y, \sigma^z)$ we define the rotation operator as

$$R_{\hat{n}}(\theta) = \exp\left(\frac{-i\hat{n}.\vec{\sigma}\theta}{2}\right) = \cos(\theta/2)\sigma_{\mathbb{1}} - i\sin(\theta/2)[n_x\sigma^x + n_y\sigma^y + n_z\sigma^z]. \tag{1.15}$$

One of the simplest but most extensively used single qubit gates is the NOT gate. This gate maps the $|0\rangle$ to $|1\rangle$ and vice versa. In terms of rotation, NOT gate is a $180°$ rotation about $\hat{x}$-axis, up to an overall global phase, which is irrelevant. The matrix representation of NOT gate is

$$U_{NOT} = \begin{bmatrix} 0 & 1 \\ 1 & 0 \end{bmatrix} \tag{1.16}$$

Another important single qubit gate is the *Hadamard* gate, $H$, which when operated on the computational basis states, produces superposition states, as shown below.

$$|0\rangle \xleftrightarrow{H} \frac{|0\rangle + |1\rangle}{2}, \ |1\rangle \xleftrightarrow{H} \frac{|0\rangle - |1\rangle}{2}.$$

A single qubit Hadamard gate is a $180°$ rotation about the direction half way between +ve $\hat{z}$ and +ve $\hat{x}$ axis on a Bloch sphere. The matrix representation of $H$ is shown below

$$H = \frac{1}{\sqrt{2}} \begin{bmatrix} 1 & 1 \\ 1 & -1 \end{bmatrix}. \tag{1.17}$$

#### 1.1.2.2   Multi-qubit gate

One of the most widely used two-qubit gate in quantum information processing is the *controlled-NOT gate* or CNOT gate. The action of $CNOT_{ij}$ is to apply a NOT gate on the target qubit, qubit $j$, only if the the control qubit, qubit $i$, is in state $|1\rangle$. The truth table for such a gate is represented below

$$
CNOT_{12} = 
\begin{array}{c|c}
\text{In} & \text{Out} \\
\hline
00 & 00 \\
01 & 01 \\
10 & 11 \\
11 & 10 \\
\end{array}
\ , \qquad
CNOT_{21} = 
\begin{array}{c|c}
\text{In} & \text{Out} \\
\hline
00 & 00 \\
01 & 11 \\
10 & 10 \\
11 & 01 \\
\end{array}
$$

One can write an arbitrary two-qubit quantum state, $\psi = a|00\rangle + b|01\rangle + c|10\rangle + d|11\rangle$, in its matrix representation as

$$|\psi\rangle = \begin{bmatrix} a \\ b \\ c \\ d \end{bmatrix}$$

The two qubit gate, CNOT, can also be written as a $4 \times 4$ matrix as follows

$$\text{CNOT}_{12} = \begin{bmatrix} 1 & 0 & 0 & 0 \\ 0 & 1 & 0 & 0 \\ 0 & 0 & 0 & 1 \\ 0 & 0 & 1 & 0 \end{bmatrix}, \qquad \text{CNOT}_{21} = \begin{bmatrix} 1 & 0 & 0 & 0 \\ 0 & 0 & 0 & 1 \\ 0 & 0 & 1 & 0 \\ 0 & 1 & 0 & 0 \end{bmatrix}.$$

Just as we defined a CNOT gate where a NOT operation was performed on the target qubit, only if the control was in the $|1\rangle$ state, one can also think of similar control operation in which NOT gate is operated on the target qubit only when the control qubit is in $|0\rangle$ state. The natural extension of such a controlled gate is a controlled-$U$ gate, where the unitary operation, $U$, is performed on the target qubit instead of a NOT gate. Here we mention another two-qubit gate called the SWAP gate, which as the name suggests *swaps* the state of the two qubits. The matrix representation of it is shown below.

$$U_{\text{SWAP}} = \begin{bmatrix} 1 & 0 & 0 & 0 \\ 0 & 0 & 1 & 0 \\ 0 & 1 & 0 & 0 \\ 0 & 0 & 0 & 1 \end{bmatrix}$$

## 1.2   Quantum Thermodynamics and Information

Computation and communication (Quantum and classical), both deal with processing of information. This information in turn can take many forms. But as discussed before, whatever the form of the information it is always processed, stored and transformed in terms of 0's and 1's. And we need physical systems to represent these 0's and 1's, in order to do something meaningful with

this information. In doing so the abstract notion of information becomes a subject of physical laws and in turn has a very close connection to thermodynamics.

Let us take an example of four coins. These four coins can have 16 configurations: 6 configurations for two heads and 2 tails, 4 configurations each for both 3 tails and 1 head, and 3 heads and 1 tail. Finally, there is only 1 configuration each for 4 heads and 4 tails. One can thus assign respective probability, $p_i$, for these events. It is easy to verify that $\sum_i p_i = 1$. But what is interesting to note is that, if we toss all the four coins simultaneously with our eyes closed we have very little information about the outcome of the toss. As soon as we open our eyes we know the state of the system for sure. So in the process of going from closed eyes to open eyes, we gained information about the system. The lack of the information about the system when our eyes are closed is quantified by the so-called *Shannon Entropy* [8] and is defined as below

$$H = -\sum_i p_i \log_2 p_i. \tag{1.18}$$

For the case of the 4 coins, before we open our eyes, the Shannon entropy can be seen to be around 2.03. Where as, as soon as we open our eyes we exactly know which event has occurred ( or state the system is in) and thus all values of $p_i$ become 0, except one. From this it is easy to see that the lack of information, quantified by the Shannon entropy, is 0. It is for this reason, entropy is also thought of as the measure of the disorder in the system. In this sense Shannon entropy can be regarded as the average amount of surprise in the system. One can similarly quantify information in quantum domain using *von Neumann entropy* as will be seen the subsequent subsections.

We mentioned earlier that as the information is being stored in physical systems, it comes to obey the physical laws, dictating the system, and the second law of thermodynamics is one of the most pious laws in Physics which has stood the test of time over and again. Although we give a detailed discussion of this in the next sections, here we give a brief flavour of the same. If we consider a collection of spin-1/2s in a bath. In the absence of any external magnetic field all the spins are randomly oriented and thus the system can be said to be disordered. But as soon as one switches on a static magnetic field, there is a slight bias of the spin orientations toward the applied magnetic field. Thus the spins on an average are oriented along the static field. After switching on the field we know more about the system (their average orientation) as a result the system can be said to be less disordered. In other words the entropy of the system reduced. Entropy also has

a role in thermodynamics, and second law of thermodynamics tells us the reduction of entropy has to be accompanied by energy being pumped into the system by, say, the environment. Thus one can see the direct connection between information and thermodynamic variables, like heat and work.

## 1.2.1 Landauer's principle and implications
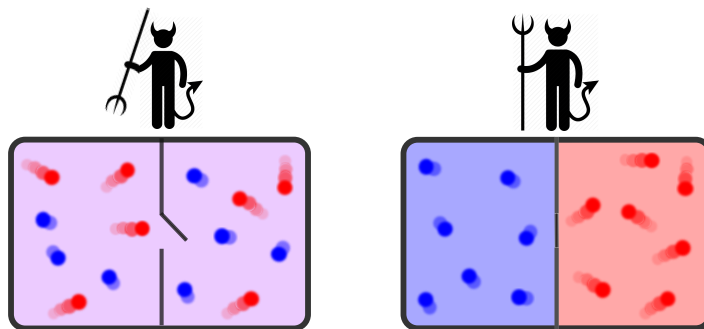


**Figure 1.2:** Schematic for Maxwell's demon.

Landauer in his 1961 seminal paper, [10] showed that, erasure of 1 bit of information always entails *at least* $k_B T \ln 2$ amount of energy cost and reduces the entropy of the system by an amount $k_B \ln 2$. Here $k_B$ is the Boltzmann constant.

Landauer's principle helped put the age old problem of *Maxwell's Demon* to rest. Maxwell in 1871, proposed a hypothetical experiment, in which we have a gas at thermal equilibrium with its environment. This gas is partitioned in the middle with a an elastic wall with a small massless window operated by a *very smart* demon, know as the Maxwell's demon. This demon operates this window such that only the fast moving gas particles are allowed to cross the window from one side and the slow moving from the other side. The problem with this setup is that it seems to violate our *very precious* second law of thermodynamics. Due to the selective passage of gas particles from one side to other, mediated by the demon, one can obtain a separation of gas at two different temperatures, thereby reducing the entropy of the whole system, without performing any work. There were many attempts at resolving the inconsistency, but this problem was finally put to bed by Charles Bennett, using Landauer's principle [11–13]. He showed that the reduction in total entropy occurs at the expense of a 1 bit of memory, which is at the demon's disposal to store the information about the speed of the particles. For the use of this memory for subsequent

measurements the demon needs to erase this memory to reset it, which from Landauer's principle we know entails an energy cost. This energy is dissipated into the heat bath. In the next section we give a quantitative and simpler example of information to work/heat conversion.

### 1.2.2 Szilard Engine
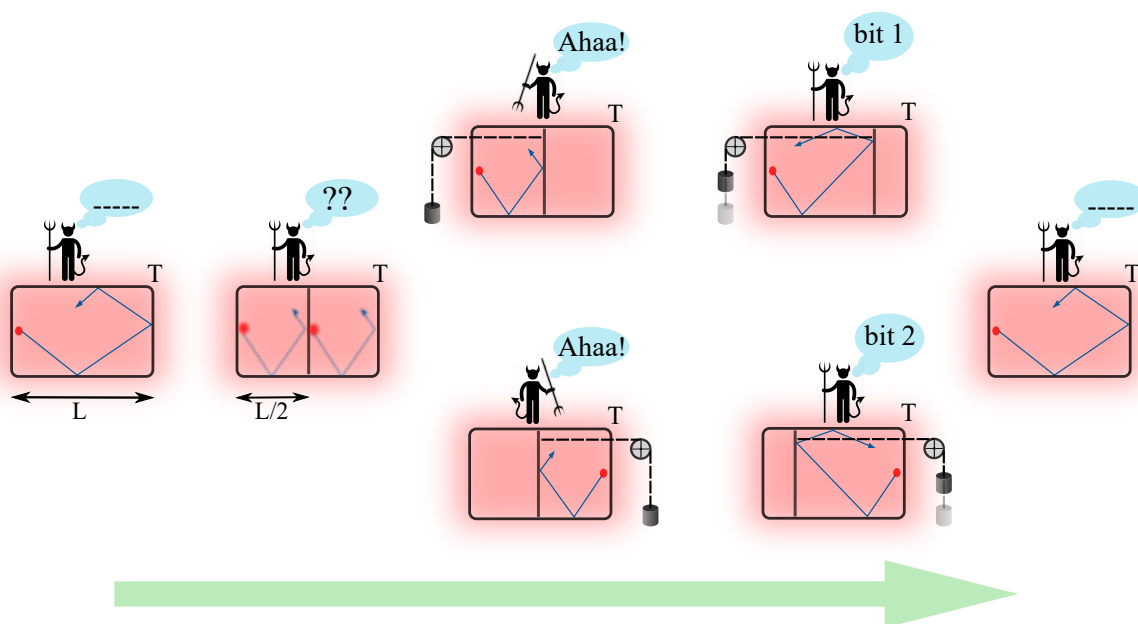


**Figure 1.3:** Schematic of Szilard engine.

The role played by information in thermodynamics is well illustrated by the working of single particle *Szilard Engine* [14], proposed by Leo Szilard in 1929. Let us consider a box with volume V, length L and elastic walls, in thermal contact with a surrounding environment maintained at temperature, T at all times (see Fig. 1.3). Inside this box we have an ideal gas particle bouncing around with a constant kinetic energy of $k_B$T ($k_B$ is the Boltzmann's constant). This box is under continuous supervision by a *Maxwell's demon*. Since this system is at thermal equilibrium with the environment, from Clausius statement of second law of thermodynamics, which states that it is only possible for heat to flow from higher to lower temperature reservoir on it's own [15], it is evident that no amount of work can be extracted from this system. At some instant, the demon introduces a movable wall in the middle of this box, as shown in Fig. 1.3. It can be so assumed,

that the wall has infinitesimally small mass and thus the work needed to introduce the wall can be neglected. At this point the demon has no information about the position of the gas particle in the box. The particle can either be in left (bit value 0) or right (bit value 1) of the introduced wall, with the same probability. The demon at this point measures the position of the particle and stores this information. The demon then utilises this information gained, to appropriately attach a pulley-weight system to the movable wall at the centre, see Fig. 1.3. As the particle is trapped in one side of the movable wall, the particle pushes the wall in the direction depending upon its position and lifts the weight attached to it performing work. If the wall was introduced in the middle of the box one can calculate the work performed/extracted in the expansion as

$$W = \int_{V_i}^{V_f} P dV = \int_{V/2}^{V} P dV = \int_{V/2}^{V} \frac{k_B T}{V} dV$$
$$= k_B T \ln 2 \tag{1.19}$$

Here we have used the ideal gas equation for a single particle, $PV = k_B T$, to get the value of work, W. Finally when the system has expanded to the volume V,the movable wall is removed from one of the ends of the box. It seems as if the system has returned to its initial state and the cycle is complete, but we would be wrong to assume this. Initially the demon started off with a single bit of *empty* memory. But when the measurement was performed, the demon either stored $0 = $ left or $1 = $ right (depending upon the outcome of the measurement) into its one bit memory. To make sure that the entire system, which also includes the demon returns to its initial state thus completing the cycle, we need to make sure that the memory of demon should also me restored, in other words, we need to erase the memory containing the information about the measurement performed. But from *Landauer's principle* we know that an energy cost of atleast $k_B T \ln 2$ is required to erase one bit of information. Comparing with Eq. 1.19 we see that this is precisely the amount of work we extracted. Thus what we saw was conversion of information, gained by measurement, (along with heat) into work. This thought experiment gives us a taste of information being as physical as other thermodynamic variables like heat and work. Just like these thermodynamic variables, information can be used as a resource. People have experimentally realised variants of such engine in the past decade [16, 17].

It is instructive to mention it here that the above mentioned protocol was completely classical and did not take into account the *quantumness* of the gas particle. People have extended

such a classical information engine to quantum scenario, where the particle is now considered to be de-localised inside a potential [18]. A few major differences in the quantum case are: i) the introduction of the wall (here a potential) changes the boundary conditions of the box, thus requiring work, ii) the particle statistics is quite different and iii) The memory of the demon can be entangled with particle [19]. Extending this work people have also realised engines driven by information [20, 21].

### 1.2.3 Quantum correlations

*Quantum correlation* can be thought of as the quantification of the connection between the two systems states, expressed in terms of the impossibility to completely divide the measurement outcomes of the corresponding states into independent non-overlapping sets. Quantum correlations are often used as a resources in quantum information processing to our benefit. There are quite a few kinds of quantum correlations. In this section we will briefly touch upon a few of them which will be used in this thesis.

#### 1.2.3.1 Quantum discord

There are more than one agreed upon definitions of quantum discord [22]. In this thesis we will use the definition proposed by Zurek et. al. [23] in 2001. We first give qualitative explanation of quantum discord. For this we first consider a bipartite *quantum-classical state* of the form

$$\rho_{QC} = \sum_i p_i \rho_A \otimes |b_i\rangle\langle b_i|, \tag{1.20}$$

where $\{b_i\}$ forms the orthonormal basis for the classical system, $B$. Here $A$ is taken as the quantum state, which can generally be disturbed by performing quantum measurements. Whereas, $B$ is considered to be in a classical state because a classical state should be represented by orthogonal states and thus be distinguishable, and there exists a measurement on the $B$, $\Pi_i = |b_i\rangle\langle b_i|$, such that the entire state of the system remains unchanged, $\sum_i \Pi_B^i \rho_{QC} \Pi_B^i = \rho_{QC}$ and the measurement satisfies the condition $\sum_i \Pi_B^i = 1$. Any bipartite state which can not be written out in the form of Eq. 1.20, must have quantum discord in it. This qualitative definition makes it clear that separability does not imply absence of quantum correlation and since quantum discord depends upon the measurement performed on a subsystem, quantum discord is not symmetric.
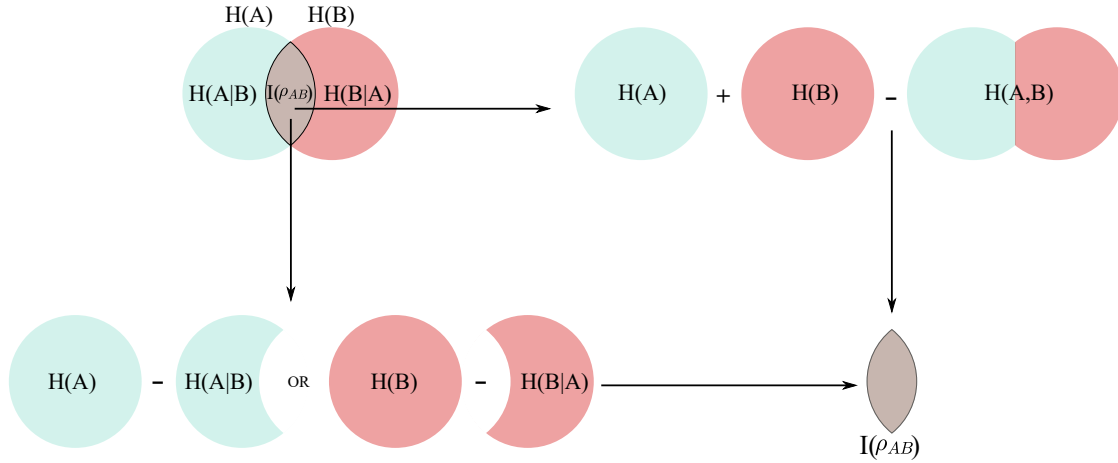
**Figure 1.4:** Venn diagram for the information in terms of Shannon entropy. This diagram pictorially represents that the two classical definitions of mutual information lead to the same value.

Zurek and Ollivier in their 2001 seminal paper, [23], quantified quantum discord in terms of the difference between the two definitions of *mutual information*, in quantum regime. It is often instructive to use an information Venn diagram when discussing quantum mutual information. Information is measured in terms of Shannon entropy of a state. Mutual information between two subsystems $A$ and $B$, $I(A:B)$, is the common information shared between them. For a classical system this is written in terms of the Shannon entropy as follows,

$$I(A:B) = H(A) + H(B) - H(A,B). \tag{1.21}$$

$H(A,B)$ is the joint Shannon entropy [24] of the combined system $AB$. Another way of defining mutual information is in terms of the conditional entropy, $H(A|B)$ and $H(B|A)$, which involves measurements on $B$ and $A$, respectively, and is defined as

$$H(A|B) = \sum_i p(B=b_i)H(A|B=b_i) = -\sum_{i,j} p(B=b_i)p(A=a_j|B=b_i)ln[p(A=a_j|B=b_i)].$$
$$\tag{1.22}$$

At this point we use Bayes rule of condition probability, $p(A=a_j|B=b_i) = p(A=a_j, B=$

$b_i)/p(B = b_i)$, in equation 1.22 to obtain

$$H(A|B) = -\sum_{i,j} p(A = a_j, B = b_i)ln[p(A = a_j, B = b_i)] + \sum_{i,j} p(A = a_j, B = b_i)ln[p(B = b_i)]$$

$$= H(A, B) - H(B). \tag{1.23}$$

Thus, along with Eq. 1.21 one can very easily see that the classical mutual information shared between system $A$ and $B$ can also be written as

$$I(A : B) = H(A) - H(A|B) = H(B) - H(B|A). \tag{1.24}$$

Fig. 1.4 explains these two definitions of mutual information pictorially. As we know quantum systems are immensely sensitive to measurements, things are not quite the same in quantum mechanics. Information in quantum state, $\rho$, is measured using quantum von Neumann entropy [25] $S(\rho) = -\sum_i \lambda_i log_2 \lambda_i$, where $\lambda_i$ are the states eigenvalues. In 2001, Henderson and Vedral [26] showed that the maximum classical correlation in a system can be expressed as the maximum value of

$$\mathcal{J}(A : B) = S(A) - S(A|B) = S(A) - \sum_i p_i S(A|B = b_i), \tag{1.25}$$

where the maximisation is performed over orthonormal measurements on $B$, $\Pi_B^i$. Quantum mutual information, which includes all classical and quantum correlations, is defined as

$$\mathcal{I}(A : B) = S(A) + S(B) - S(A, B). \tag{1.26}$$

Thus one can find the non-classical correlations in a system as the difference

$$D(A|B) = \mathcal{I}(A : B) - \max_{\Pi_B^i} \mathcal{J}(A : B). \tag{1.27}$$

This difference is the mathematical definition of *Quantum Discord* that we use in this thesis. From here it is easy to see that Discord is not symmetric, i.e. $D(A|B) \neq D(B|A)$.

### 1.2.3.2 Quantum entanglement

Quantum entanglement is a restricted subsection of quantum correlations, possessed by systems whose states can not be written as a product of two states. In this thesis we will only be dealing with bipartite quantum entanglement. A pure composite quantum state is said to be entangled, if

it can not be written in a separable form

$$|\psi_{AB}\rangle = |\psi_A\rangle \otimes |\psi_B\rangle. \tag{1.28}$$

For the mixture of product states separability is defined as

$$\rho_{AB} = \sum_i p_i \rho_A^i \otimes \rho_B^i, \tag{1.29}$$

where the $p_i$ are the probability of the product states. Any state which can not be written in this form is said to have entanglement. Entanglement is extensively used in quantum information processing as a resource. Like discord, quantum entanglement also has a number of quantifiers, but in this thesis we are only interested in *Entropy of Entanglement* and *Negativity* as the measure of Entanglement for pure and mixed states, respectively.

Using Schmidt decomposition, one can write the generalised state of a bipartite pure state as,

$$\rho_{AB} = \sum_i \lambda_i |a_i\rangle |b_i\rangle. \tag{1.30}$$

Here $\lambda_i$s are the Schmidt's coefficients and in a sense contain the information about the quantum entanglement in the system. The entropy of such a pure state is always *zero*, i.e. $S(AB) = 0$. On this state if one performs *partial trace*, see Eq. 1.11, over one of the sub-systems, the individual states of the remaining sub-systems can be written as

$$\rho_A = \text{Tr}_B[\rho_{AB}] = \sum_i |\lambda_i|^2 |a_i\rangle\langle a_i|$$
$$\rho_B = \text{Tr}_A[\rho_{AB}] = \sum_i |\lambda_i|^2 |b_i\rangle\langle b_i|. \tag{1.31}$$

It is instructive to convince one-self here that for certain values of $\lambda_i$ in Eq. 1.30, the reduced density matrix of the subsystems, Eq. 1.31, can represent a *mixed state*. This decrease in the purity of a state under partial trace can be seen as measure of inseparability of a quantum state and is quantified by the von Neumann entropy of the remaining sub-system obtained after partially tracing out the other sub-system, i.e.

$$E_{A:B} = S(A) = S(B). \tag{1.32}$$

Here, $E_{A:B}$ is called the *entropy of entanglement* and $S(A)$ and $S(B)$ are the von Neumann en-

tropy of the corresponding subsystems.

The above definition of quantum entanglement can not be extrapolated for mixed states. It was shown by A. Peres in [27] that the eigenvalues of partial transpose of a separable composite state, w.r.t it's subsystem is always positive. As entanglement is the measure of non-separability of a quantum state, one can imagine quantifying quantum entanglement in terms of the negative eigenvalues of the partial transpose of the bipartite system, w.r.t it's subsystem. Mathematically we define this quantifier as

$$N(\rho_{AB}) = \frac{||\rho_{AB}^{T_A}|| - 1}{2},$$ 

(1.33)

where, $||\rho_{AB}^{T_A}||$ is the trace norm of partial transpose of the composite state $\rho_{AB}$ w.r.t to subsystem $A$ [28].

### 1.2.4 Work and Heat in quantum systems
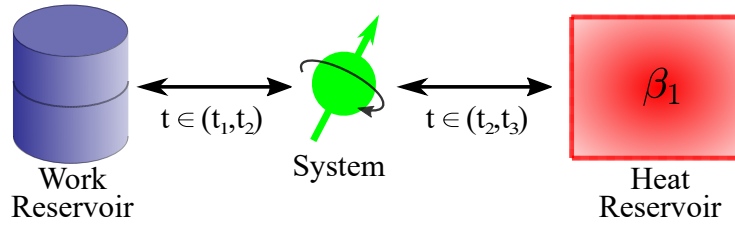


**Figure 1.5:** Schematic for temporally separated heat and work exchange. The quantum system, here represented by a spin-1/2 particle, exchanges energy in the form of work with the *work reservoir* for time $t \in (t_1, t_2)$. Followed by this, for time $t \in (t_2, t_3)$ the system exchanges energy in the form of heat with a heat reservoir maintained a constant inverse temperature, $\beta_1$.

Measuring and distinguishing work and heat in quantum processes are non-trivial tasks. The reason for this is, a quantum state $\rho$ may not always be in one of the eigenstates of the Hamiltonian. As a result measurement of the energy causes the quantum state to collapse onto one of the eigenstates of the Hamiltonian thereby disturbing the system. Moreover, the measurement of the average energy, E = $\langle H \rangle = \text{Tr}[H\rho]$, involves averaging over many trials. Here H corresponds to the Hamiltonian of the system. Depending upon the system in question, there are many accepted protocols to measure heat and work. One of the definitions involve separating heat and work exchange temporally and then measuring the change in the internal energy $\Delta$E. As shown in the Fig. 1.5 the quantum system's interaction with the heat and work reservoirs are separated

in time. In doing so we can account for the energy change associated with each process, quantifying the amount of work or heat exchange. One major drawback of such temporal separation of the processes is that it can not handle situations in which both heat and work exchange occur simultaneously, among others.

Instead of separating heat and work in time, we can define work in terms of the control parameters and heat in terms of the state of the quantum system. The internal energy, $E(t)$, of a quantum system, in a state $\rho(t)$, can be written in terms of the expectation value of Hamiltonian, H, as $E(t) = \langle H(t) \rangle = \text{Tr}[H(t)\rho(t)]$. Using this relation one can write

$$dE(t) = \text{Tr}[\rho(t)dH(t)] + \text{Tr}[H(t)d\rho(t)]$$
$$= dW(t) + dQ(t). \tag{1.34}$$

The first and second term in the above equation are identified as the the work and heat energy exchanged by the system, respectively. The work exchanged term only includes the energy associated with the change of the control parameter, namely the Hamiltonian. Where as, the heat term corresponds to the energy exchange due to the change in the state of the system. For example, it we consider the case of a single spin-1/2 particle in a static magnetic field, $B(t)\hat{z}$. In the presence of such a magnetic field the spin-1/2 particle undergoes *Zeeman splitting*, with energy gap between the eigenstates proportional to the magnitude of the field applied. Now if one increases the strength of static magnetic field very slowly, *quantum adiabatic theorem* [29] tells us that the state of the system remains unchanged. The energy pumped into the system due to the adiabatic increase of the magnetic field, $B(t)$, solely corresponds to the work done on the system. Similarly, if under certain operation the Hamiltonian of the system remains unchanged and just the state of the system changes, the energy exchanged by the system is then identified as Heat. In this thesis we will be considering only these definitions of work and heat.

### 1.2.5   Some quantum thermodynamic phenomena

The thermodynamic processes we are going to deal with in this thesis are for systems out of equilibrium. Such *non-equilibrium* thermodynamic processes deal with thermodynamic systems in transient processes, driven systems, steady state systems, etc. and establishes relationships between the various thermodynamic quantities like heat, work, entropy, free energy etc. for such

out of equilibrium processes. Most of the equalities that we come across in phenomenological thermodynamics are for systems in equilibrium with its environment. Although multiple transient fluctuation theorems were introduced in early 1990s, [30–32], for entropy production *Jarzynski-Crooks'* fluctuation relation was the first equality proposed for a transient system and relates the free energy of an out of equilibrium system to the exponential average of the work performed on it [33, 34]. The quantum version of the same was soon put forward by Hal Tasaki [35]. In Chap.2 we will see the quantum version of such a fluctuation relation for the case of heat exchange in great details. Further we examine the bounds on the uncertainty of the heat flow between two quantum systems in Chap.3. One of the many interesting properties of driven many-body quantum systems is the stability of discrete time-crystalline order. Just as crystals spontaneously break the translational symmetry of the space, certain driven quantum systems break the symmetry of their underlying periodically driving Hamiltonian, thereby breaking the time translational symmetry , and oscillate with a specific frequency which is an integer multiple of the driving frequency. These oscillating quantum systems exhibit remarkable stability even when errors are introduced in the driving Hamiltonian. Driven systems exhibiting such a many-body behaviour are called *Time Crystals* and have been used to study quantum thermodynamic properties of out-of-equilibrium systems like quantum thermalisation [36] and dissipative systems [37]. In the last chapter we will delve deeper into the experimental realization of this exotic behaviour.

## 1.3  Quantum information processing using NMR

Nuclear Magnetic Resonance, NMR, for long has been considered as an attractive and insightful test-bed for studying and implementing quantum computations, information processing and various other quantum phenomena. Although in the past few decades extensive work has been done to use the sophisticated technology developed for NMR to investigate various quantum computation and information processing problems, because of the very small magnetic moment associated with the nuclei, resulting in weak detection, and its thermal nature, as it operates in the room temperature, NMR is not considered the ideal choice for developing a realizable quantum computer. Nonetheless, it remains to be one of the most versatile and well studied topics which still remains relevant in exploring and demonstrating various quantum phenomena. In this section we will briefly go through the workings of NMR qubits and how to manipulate them to perform the
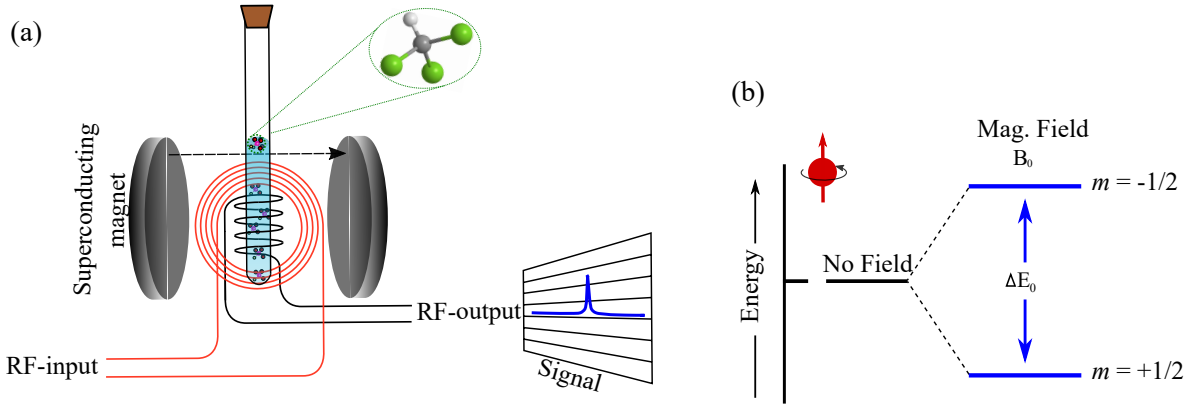
desired operations.

## 1.3.1 NMR qubits



**Figure 1.6:** (a) Schematic for NMR setup. The NMR tube holds the ensemble of molecules consisting of spin-1/2 nuclei, which act as qubits. These spins are manipulated and read-out using Radio-Frequency (RF) pulses. (b) Zeeman splitting of the nuclear spin-1/2 particle.

The basic requirements for a quantum system to realize a qubit are that it should posses two distinct energy levels, can be well characterised and can be manipulated enough, by an external perturbation, to realize the initial states and perform operations. NMR spin-1/2 systems in a strong static magnetic field, fulfil these requirements [7]. NMR qubit is an ensemble of spin systems. As will be shown, these spin systems can be in solid, liquid or even *liquid-crystal* phase. Typically an NMR sample consists of around $\approx 10^{15}$ molecules, say Chloroform ($CHCl_3$), in an NMR tube placed inside a superconducting magnet with a static field of $\sim 10T$ (see Fig. 1.6(a)). The NMR active nuclei in the molecule ($^1H$ in $CHCl_3$) posses the inherent property of *spin*. These spins have a net angular momentum associated with them, $\hat{\mathbf{S}}$, which takes discrete values of the form $\hbar\sqrt{S(S+1)}$ for a spin-$S$ particle. As these spins are also associated with a net magnetic moment, depending upon the angular momentum as $\mu = \gamma\hbar\hat{\mathbf{S}}$, in the presence of a net magnetic field they undergo *Zeeman* splitting (see Fig. 1.6(b)). For the magnetic field ($\mathbf{B}$) oriented in the $z$-direction the Zeeman Hamiltonian can be written as,

$$H = -\mathbf{B} \cdot \mu = -\gamma\hbar B_0 S^z = \hbar\omega S^z, \tag{1.35}$$

where $S^z = \sigma^z/2$ is the Pauli $z$-spin operator, $B_0$ is the strength of the applied magnetic field and

$\gamma$ is the gyromagnetic ratio, characterising the nuclei. One can imagine $\omega$ as the *Larmor frequency* of the magnetic moment associated with the spin, precessing about the applied magnetic field. For our case, the precession frequency is in hundreds of MHz. The eigenvalues of the Hamiltonian, $H$, takes discrete values of $-m\hbar\gamma B_0$. Here $m$ is the magnetic quantum number and takes integer or half-integer values separated by 1 in the range of $[-S, S]$. Thus for a spin-1/2 particle we have two distinct states, with magnetic quantum number $|m = 1/2\rangle$, $|m = -1/2\rangle$ (see Fig. 1.6(b)). We can label $|m = 1/2\rangle$ as logical *zero*, $|0\rangle$ and $|m = -1/2\rangle$ as logical *one*, $|1\rangle$, which correspond to one bit of information.
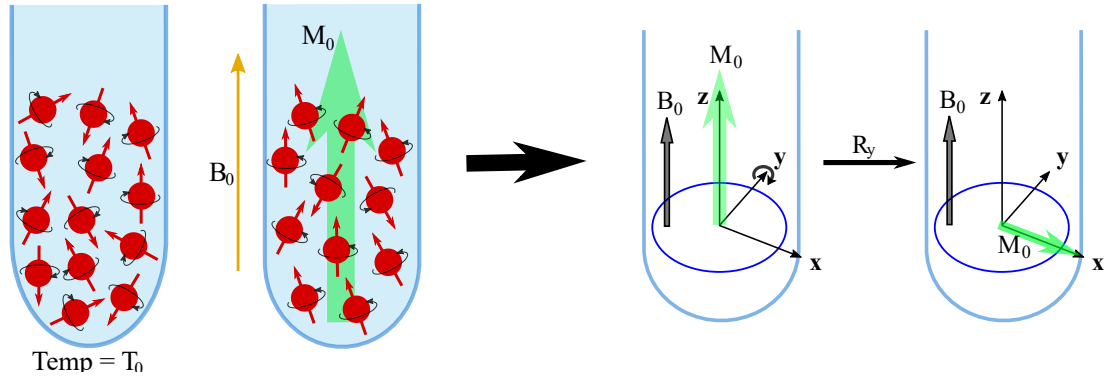


**Figure 1.7:** Schematics of net magnetic moment ($M_0$) in an NMR sample inside a static magnetic field $B_0$ and its dynamics under the operation of 90° pulse about *y*-axis, $R_y$.

For simplicity if we consider an ensemble of non-interacting spin-1/2 particles at temperature $T_0$, initially in the absence of any external field the magnetic moment of these *tiny magnets* (spins) are all randomly oriented. If we now switch on a static magnetic field (say along *z*-axis), these magnetic dipoles re-orient partially towards this external bias, giving rise to a finite net *magnetic moment* $M_0$, as shown in Fig. 1.7. In the sample, the local magnetic field experienced by the nuclei is slight different from the applied field. This is because of the different chemical environment experienced by the nuclei due to the shielding introduced by the electron cloud. The effective Zeeman Hamiltonian for $j^{th}$ spin under secular approximation can be re-written as

$$H_j = -\gamma(1 - \overline{\delta_j(\Theta)})B_0\hbar S_j^z = \hbar\omega_j^0 S_j^z, \tag{1.36}$$

where $\overline{\delta_j(\Theta)}$ is the secular *chemical shift tensor* averaged over the molecular orientation due to motional averaging (as will be seen later, this averaging is not considered in the case of Solids)

under high magnetic field and $\omega_j^0$ is the *chemically shifted Larmor frequency* of the $j^{th}$ spin. At room temperature in the presence of external magnetic field the spin ensemble follow Boltzmann distribution with a slight excess of population in the ground state. The density operator corresponding to the thermal state can then be written as

$$\rho_{eq} = \frac{e^{-H/k_b T_0}}{\text{Tr}[e^{-H/k_b T_0}]}. \tag{1.37}$$

Under the assumption of $\hbar\omega_0 << k_B T_0$ (high temperature approx.), the above form can be written in the matrix form as below

$$\rho_{eq} \approx \begin{bmatrix} \frac{1}{2} + \frac{\hbar\gamma B_0}{4k_B T_0} & 0 \\ 0 & \frac{1}{2} - \frac{\hbar\gamma B_0}{4k_B T_0} \end{bmatrix}. \tag{1.38}$$

Where the diagonal elements correspond to the populations of $|0\rangle$ and $|1\rangle$ eigenstates respectively. This can further be simplified to write the equilibrium density matrix as,

$$\rho_{eq} \approx \frac{1}{2}\mathbb{1}_2 + \epsilon\rho_{dev} = \frac{1}{2}\mathbb{1}_2 + \frac{\epsilon}{2}\sigma_z. \tag{1.39}$$

Here $\rho_{dev}$ is called the traceless deviation part of the equilibrium density matrix and $\epsilon = \hbar\gamma B_0/2k_B T_0$ is called the *purity factor*. Eq. 1.39 can be seen as containing two parts, a uniform background ($\mathbb{1}_2$) which does not evolve under unitary operations and thus contributes to no signal and a deviation part, which evolves under the unitary evolutions, from which we get the signal. It is easy to see that this state is highly mixed as $\text{Tr}[(\rho_{eq})^2] << 1$ for $\epsilon \sim 10^{-5}$ (see Sec. 1.3.3.3). The net magnetization, $M_0$, at room temperature, $T_0$, is proportional to the population difference of the two levels [38, 39]. The RF pulses can then be used to implement rotations. These RF pulses are linearly polarised pulses with two circularly polarised components. One of the components can be neglected and thus the interaction Hamiltonian of the spin with the RF pulse can be written as,

$$H_{RF}(t) = \gamma B_n \hbar(S^x \cos(\omega_{RF}t + \phi) + S^y \sin(\omega_{RF}t + \phi)), \tag{1.40}$$

where $B_n$ is the strength of the RF pulse, $\omega_{RF}$ is the carrier frequency and $\phi$ is the phase of the applied RF field. In the rotating frame of the RF field the total Hamiltonian of the system can be written as

$$\mathcal{H}_\phi = -(\omega_0 - \omega_{RF})\hbar S^z + \gamma B_n\big(S^x \cos(\phi) + S^y \sin(\phi)\big). \tag{1.41}$$

$\gamma B_n$ is often referred as the *nutation frequency* and $(\omega_0 - \omega_{RF})$ is the effective chemical shift (precession frequency) of the spins in the rotating frame. As shown in Fig. 1.7 when the state at thermal equilibrium, $\rho_{eq}$ is subjected to $R_y(\pi/2) = \exp[-i\frac{\pi}{2}S^y]$ rotation, the magnetic moment, $M_0$, comes in *x-y* plane. The expression

$$\rho = R_y\left(\frac{\pi}{2}\right)\rho_{eq}R_y^\dagger\left(\frac{\pi}{2}\right), \tag{1.42}$$

represents such a density matrix which now has off-diagonal elements or *coherences*. In the presence of the external magnetic field, $B_0$, this magnetic moment precesses about the *z*-axis (se Fig. 1.8). Inside the NMR spectrometer there are coils, through which the magnetization cuts to induce electromagnetic flux called the *free induction decay*, FID. The transverse component of the magnetization can be thought to have two components,

$$M_x(t) = -M_0\cos(\omega_0 t)e^{-\lambda t}$$
$$M_y(t) = M_0\sin(\omega_0 t)e^{-\lambda t} \tag{1.43}$$

where, $\lambda$ is the transverse decay rate. These two are all we need for our NMR signal and can be obtained by noting that $M_x = \langle\sigma_x\rangle/2$ and $M_y = \langle\sigma_y\rangle/2$. But, since $\sigma_x$ and $\sigma_y$ do not commute with each other, it is quite evident that we can not measure them simultaneously. This problem is overcome by using the technique of *quadrature detection* (Ap.5 [40]) in which the NMR signal is mixed with a *reference* radio-frequency signal in the receiver to produce two phase shifted outputs. These two outputs can be thought of as the real and imaginary parts of a complex signal as shown below.

$$s(t) \propto s_x(t) + is_y(t)$$
$$\propto \langle\sigma_x\rangle + i\langle\sigma_y\rangle. \tag{1.44}$$

The operator of interest here is thus $D = \sigma^x + i\sigma^y$, the expectation value of which is the signal we obtain from the Fourier transform of the FID,

$$\langle D\rangle = \text{Tr}[D\rho]. \tag{1.45}$$

Here $\rho$ is the density operator of the system we are measuring. This gives us the net magnetization in the transverse plane, from which one can obtain the diagonal elements of the density matrix.

To find all the elements of the density matrix one needs to use *quantum state tomography* [41, 42], discussed below.
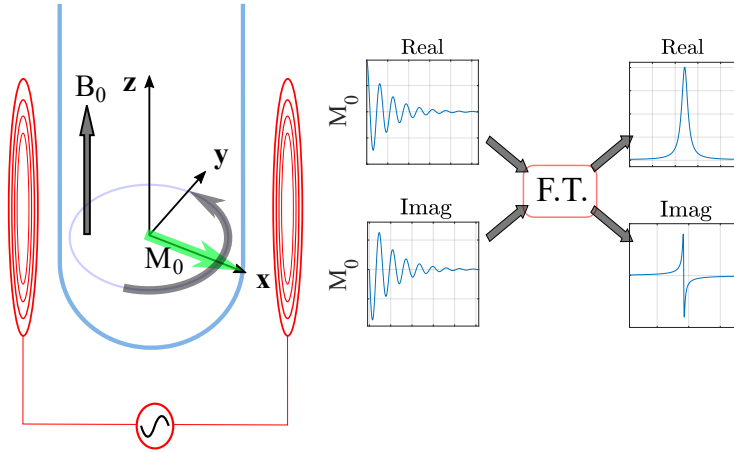


**Figure 1.8:** Detection of NMR signal. The red coils pick up the electromagnetic induction generated as the magnetic moment, $M_0$, cuts through it while precessing about the static magnetic field, $B_0$. The time domain real and imaginary part of the signal are Fourier transformed to get the frequency domain spectrum.

Initialization and executing quantum protocols are the indispensable part of quantum information processing. But it is often useful to test the preparation of the initial state, estimate the quantum error introduced by application of quantum gates and finding the fidelity of the final quantum state, among other things, while performing a quantum protocol. And for these quantifications one needs to characterise the full state density matrix of the quantum state. One way of characterising the full density matrix is by using *quantum state tomography*. It involves performing measurements on the quantum state of interest and reading them out. For example, if we have a quantum state $\rho$ which we need to tomograph, the measurement of operators, $U_{a_i} = |a_i\rangle\langle a_i|$ on the state gives us all the diagonal terms in the density matrix, in the basis $\{a_i\}$. But not all elements of the density matrix can be obtained from single measurements in the same basis. For other elements one needs to perform measurement on the same state in different basis. This process of characterizing the whole density matrix is called the *quantum state tomography*.

In the case of liquid NMR, which is what we are going to consider for most of the work taken up in this thesis, the diagonal entries can be inferred by reading out the NMR signal, see Eq. 1.45. As mentioned before, for the off-diagonal elements we need measurements in different basis. But the measurement along another basis, is just a unitary transformation in the form of rotation

followed by a measurement in this rotated basis. As it can be shown

$$\text{Tr}[\rho U^\dagger |a_i\rangle\langle a_i| U] = \text{Tr}[U^\dagger \rho U |a_i\rangle\langle a_i|], \tag{1.46}$$

rotation of the measurement basis is equivalent to the rotation of the quantum state being measured. These rotations can be realised using RF-pulses, before being measured in *z*-basis. Thus NMR quantum state tomography consists of performing a set of unitaries, realised by RF pulses and *J*-coupling (see Sec. 1.3.2) between the spins [43].

## 1.3.2 Interacting NMR qubits

Till now we have considered ensemble of non-interacting spin-1/2 systems. Chloroform, CHCl$_3$, molecule in a solvent is one such example in which $^1$H nuclei is the only NMR active nuclei and in which, further due to the *motional averaging*, the inter-molecular interactions are suppressed. In this section we consider NMR systems with more than one spin-1/2 nuclei with inter as well as intra molecular interactions. These systems are thus multi qubit systems and we will see how we can use the various interactions between these qubits along with the external RF field to realise various quantum gates and operations.

For simplicity we consider the interaction Hamiltonian between two spin-1/2 nuclei. The interactions considered in this thesis are mainly of two types, *i*) electron mediated indirect coupling, also known as the *J*-coupling, and *ii*) direct dipolar coupling, which is mediated through space. The most general Hamiltonian for two interacting spin-1/2 nuclei can be written as,

$$\mathcal{H}^0_{12} = \omega_0^1 S_1^z + \omega_0^2 S_2^z + 2\pi J_{12} \mathbf{S}_1 \cdot \mathbf{S}_2 + D_{12}(3S_1^z S_2^z - \mathbf{S}_1 \cdot \mathbf{S}_2). \tag{1.47}$$

where, $\mathbf{S}_i = S_i^x \hat{i} + S_i^y \hat{j} + S_i^z \hat{k}$ are Pauli spin operators on $i^{th}$ spin and $\omega_0^i = -\gamma_i B_0(1 - \overline{\delta_i(\Theta)})$ are the chemical shifted Larmor frequency of $i^{th}$ nuclei with $\overline{\delta_i(\Theta)}$ being their corresponding secular motional averaged chemical shift (see Eq. 1.36). The first two terms correspond to the Zeeman field experienced by the two nuclei. The third term is the isotropic electron mediated indirect scalar *J*-coupling term with $J_{12}$ being the strength of the coupling (usually in Hz). Generally $\mathbf{J}_{ij}$ is a $3 \times 3$ tensor, but as will be made clear below in this thesis we deal with only the isotropic part of this term. The fourth term in Eq. 1.47 is the secular direct dipolar coupling term obtained by neglecting the non-secular part of the total Hamiltonian in high magnetic field (see Appendix

6 of [40]). $D_{12}$ is the *secular* dipolar coupling strength which has form of

$$D_{12} = \frac{\mu_0}{8\pi} \frac{\gamma_1 \gamma_2 \hbar}{r_{12}^3} \big(3\cos^2(\Theta_{12}) - 1\big). \tag{1.48}$$

Where $r_{ij}$, $\gamma_i$ and $\mu_0$ are the distance between the $i^{th}$ and $j^{th}$ spin, gyromagnetic ratio of the $i^{th}$ spin and the magnetic constant ($\mu_0 = 4\pi \times 10^{-7}\text{H m}^{-1}$) respectively. The angle $\Theta_{ij}$ corresponds to the angle between the unit vector joining $i^{th}$ and $j^{th}$ spin, $\hat{\mathbf{r}}_{ij}$, and the static magnetic field $B_0$.

In a solid sample all the spin-1/2 nuclei in the sample interact with all the other spin-1/2 nuclei. In this case the anisotropic part of *J*-coupling survives. This anisotropic part is negligibly small as compared to direct dipolar coupling and thus can be neglected or can even be included in the dipolar term as they both have the same from. Thus, using Eq. 1.47 the total Hamiltonian of a solid sample can be written as,

$$\mathcal{H}_{solids} = \sum_{i<j} \mathcal{H}_{ij}^0, \tag{1.49}$$

where now the $\omega_0^i(\Theta) = -\gamma_i B_0\big(1 - \delta_i(\Theta)\big)$, has dependence on the atomic orientation, $\Theta$, with applied magnetic field. As a result the solid state samples have a plethora of disorder in the system.

Anisotropic liquids, *liquid crystals*, have a favourable spatial direction (referred as the *director* in liquid crystal literature) and thus the translational and rotational mobility of the molecules are not isotropic. This makes liquid crystals very different from isotropic liquids. Due to the partial motional averaging in a favoured direction the chemical shift for such an anisotropic liquid is obtained by averaging over the molecular orientation, $\Theta$, with their corresponding probabilistic weights. Similarly, due to the translational diffusion of the molecules in a liquid crystal the short-term inter-molecular dipolar interactions are averaged out. Although the long range inter-molecular interactions are not averaged out, their strength is so weak that they can be safely ignored. In liquid crystals, due to the preferred molecular orientation (which can be oriented away from the applied static magnetic field), the secular part of the intra-molecular dipolar interactions are not averaged out. The total Hamiltonian for such an anisotropic liquid can then be written as

$$\mathcal{H}_{lc} = \sum_{i<j} \omega_0^i S_i^z + \omega_0^j S_j^z + \overline{D}_{ij}(3S_i^z S_j^z - \mathbf{S}_i \cdot \mathbf{S}_j). \tag{1.50}$$

Here $\omega_0^k$ has the same meaning as in Eq. 1.47. Also the overbar in the secular dipolar interaction $\overline{D}_{ij}$ corresponds to the average of Eq. 1.48 over all the molecular orientations, $\Theta$, with their corresponding probability. Note that here we have dropped the scalar *J*-coupling term as explained in the case of solids.

For the case of isotropic liquids things become relatively simpler as the molecules tumble around freely in every direction and orientation with equal probability. The secular dipolar coupling is thus averaged out and the chemical shift takes isotropic average of $\delta_i(\Theta)$. The only interaction that survives in a liquid sample is the intra-molecular scalar *J*-coupling term, which is further simplified in the weak coupling limit. The net Hamiltonian of a liquid sample in high magnetic field and weak coupling limit ($|J_{ij}| << |\omega_0^i - \omega_0^j|$) can be written as,

$$\mathcal{H}_{liq} = \sum_{i<j} \omega_0^i S_i^z + \omega_0^j S_j^z + J_{ij} S_i^z S_j^z. \tag{1.51}$$

In the next section we use these coupling Hamiltonians along with the interaction with RF field (see Eq. 1.40) to realize some quantum gates and demonstrate the preparation of multi-qubit pseudo-pure state (PPS).

### 1.3.3   NMR quantum gates and PPS

Quantum computation and information processing are based on a set of universal quantum gates and operations, just like the classical information processing. These gates and operations are the building-blocks of quantum simulations and executing quantum algorithms. These quantum gates are nothing but unitary operations on the spins to generate the desired effects. NMR has a long history of manipulating large spin systems using RF pulses, spin-spin interactions and precession under the static magnetic field. In this section we will see the NMR implementation of a few of these universal single and multi qubit gates and operations using the RF rotations on the spins and interactions between the spins discussed in the previous section.

#### 1.3.3.1   Single qubit gates

As will be seen, most of the simple single qubit gates are realised as rotations about a direction in the Bloch sphere using RF pulses. The action of RF pulse with an amplitude of $B_n$ on a spin

for a time $t$ is of the form

$$(\theta)_\phi = \exp\left(-i\theta S_\phi\right) = \exp\left(-i\omega_n t S_\phi\right). \tag{1.52}$$

Where $\omega_n = \gamma B_n$ is the *nutation frequency* and depends upon the RF amplitude, $B_n$, and $S_\phi = S_x \cos(\phi) + S_y \sin(\phi)$ is the spin operator with phase, $\phi$. This operation performs the rotation of the spin by an angle of $\theta$ about a direction dictated by the phase $\phi$ in the Bloch sphere. We now see how this is used to realise some single qubit gates.

One of the simplest but extensively used gate is the **X** or **NOT** gate. This gate flips $|0\rangle \rightarrow |1\rangle$ and has a matrix representation as follows

$$\mathrm{X} = \begin{bmatrix} 0 & 1 \\ 1 & 0 \end{bmatrix}. \tag{1.53}$$

In NMR this can be realised simply by performing a $\pi$ angle rotation about $x$-axis as follows

$$(\pi)_x = -i \begin{bmatrix} 0 & 1 \\ 1 & 0 \end{bmatrix}. \tag{1.54}$$

The global phase factor of $-i$ can be neglected.

Another useful gate is the *Hadamard* gate, which produces an equal superposition of $|0\rangle$ and $|1\rangle$ when operated on $|0\rangle$. The matrix form for it is shown below

$$\mathrm{H} = \frac{1}{\sqrt{2}} \begin{bmatrix} 1 & 1 \\ 1 & -1 \end{bmatrix}. \tag{1.55}$$

This quantum gate can again be realised as follows

$$(\pi)_x \left(\frac{\pi}{2}\right)_y = \frac{1}{\sqrt{2}} \begin{bmatrix} 1 & 1 \\ 1 & -1 \end{bmatrix}. \tag{1.56}$$

Note that the pulses are time ordered from right to left.

The various phase gates like

$$Z = \begin{bmatrix} 1 & 0 \\ 0 & -1 \end{bmatrix}, \quad S = \begin{bmatrix} 1 & 0 \\ 0 & i \end{bmatrix}, \quad T = \begin{bmatrix} 1 & 0 \\ 0 & e^{i\pi/4} \end{bmatrix}, \tag{1.57}$$

are obtained by the application of the pulse sequence

$$R(\theta) = \left(\frac{\pi}{2}\right)_x (\theta)_y \left(\frac{\pi}{2}\right)_{-x}. \tag{1.58}$$

From the above expression one can get back the form of $Z$, $S$ and $T$ gates by putting $\theta = \pi$, $\pi/2$ and $\pi/4$ in Eq.1.58.
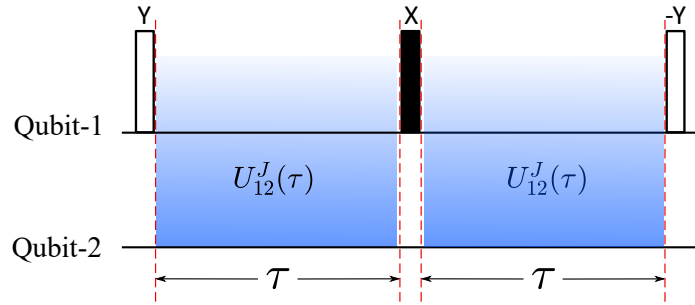
### 1.3.3.2 Multi qubit gates and operations



**Figure 1.9:** Pulse sequence for refocussing the *J*-coupling between two spin-1/2 particles. The pulses are time ordered from left to right. The black and white narrow bars represent $\pi$ and $\pi/2$ angle pulses about the axis mentioned above them. $\tau$ is the time for each evolution under the interaction Hamiltonian given Eq. 1.51. The blue shaded region represent the evolution under the *J*-coupling Hamiltonian represented by $U_{12}^J(\tau)$.

Here we will discuss a few important multi-qubit gates and their implementation in NMR. For this we are going to use liquid NMR system as an example as this is the system pre-dominantly used in this thesis. Thus the interactions used to prepare the gates will be of the form shown in Eq. 1.51. Before moving on to these examples it is instructive to consider a very important method used in NMR to 'turn off' the *J*-coupling (see Sec. 1.3.2) between two spin-1/2 particles in a liquid NMR system. This method is called *refocussing*, for reasons which will become clear as we move along. For simplicity we consider two different species of spin-1/2 nuclei, coupled to each other in a molecule in a liquid sample, each initialised in the *z*-direction. The refocussing pulse sequence is shown in Fig. 1.9. Starting from the left, qubit 1 initialised along *z*-axis of the Bloch sphere is subjected to $(\pi/2)_y$ pulse which takes it along the *x*-axis. After this the two spins are allowed to interact with each other by *J*-coupling, of the form shown in the figure, for a time $\tau$. This is followed by a $(\pi)_x$ pulse on the $1^{st}$ qubit and followed by again an evolution under the coupling as shown. This second evolution along with the $(\pi)_x$ pulse on the first qubit undo

the effect of the first evolution and one can think of it as the refocussing of the state. As a result, before application of the final $\pi/2$ pulse the system returns to the same state as after application of only the first $\pi/2$ pulse. The final $\pi/2$ pulse just brings back the state along $z$-axis. Thus we see that although the system evolved under the coupling for a total time of $2\tau$, the state of the system remained unchanged. we are going to see the use of this in method when making PPS and some multi qubit gates.

Controlled NOT (CNOT) gate is one of the most useful gates in quantum information processing and computing. The matrix form of this gate is written as

$$
\mathrm{CNOT}_1 =
\begin{bmatrix}
1 & 0 & 0 & 0 \\
0 & 1 & 0 & 0 \\
0 & 0 & 0 & 1 \\
0 & 0 & 1 & 0
\end{bmatrix}, \quad
\mathrm{CNOT}_2 =
\begin{bmatrix}
1 & 0 & 0 & 0 \\
0 & 0 & 0 & 1 \\
0 & 0 & 1 & 0 \\
0 & 1 & 0 & 0
\end{bmatrix}.
\tag{1.59}
$$

Where $\mathrm{CNOT}_1$ and $\mathrm{CNOT}_2$ are controlled NOT gate with control on the $1^{st}$ and $2^{nd}$ qubit respectively. Such a controlled (non-local) gate can be realised in NMR setup using pulse sequences shown below.

$$
U_{\mathrm{CNOT}_1} = \left(\frac{\pi}{2}\right)_z^{S_1} \left(\frac{-\pi}{2}\right)_z^{S_2} \left(\frac{\pi}{2}\right)_x^{S_2} U_{12}^J \left(\frac{1}{2J_{12}}\right) \left(\frac{\pi}{2}\right)_y^{S_2}
$$
$$
U_{\mathrm{CNOT}_2} = \left(\frac{\pi}{2}\right)_z^{S_2} \left(\frac{-\pi}{2}\right)_z^{S_1} \left(\frac{\pi}{2}\right)_x^{S_1} U_{12}^J \left(\frac{1}{2J_{12}}\right) \left(\frac{\pi}{2}\right)_y^{S_1}.
\tag{1.60}
$$

Here the pulse sequences have been time ordered from right to left.

### 1.3.3.3 Pseudo-pure state

In Sec. 1.1.1.2 we discussed about what it means for a system to be in a pure state and mixed state. NMR system is largely in a highly mixed state as preparation of a pure state requires either application of very high static magnetic field, $B_0$, or reducing the temperature of the system to extremely low temperatures. This can further be seen in Eq. 1.39, where we present the highly mixed state of an NMR system. Rewriting the thermal state of an ensemble of non-interacting spin-1/2 NMR system, given in Eq. 1.39, as

$$
\rho_{eq} = \left(\frac{1-\epsilon}{2}\right) \mathbb{1}_2 + \epsilon |0\rangle\langle 0|
\tag{1.61}
$$

one obtains the *pseudo-pure state* (PPS), which mimics the behaviour of a pure state [44]. Here $\epsilon$ is the purity factor as mentioned before and takes a value of $\sim 10^{-5}$ for an ensemble of $^1$H nuclei in a static magnetic field of $B_0 = 10$T. As many of the quantum information processing protocols require initializing the systems in pure state (we will see this in subsequent chapters), PPS provides a way to simulate such protocols in a highly mixed experimental system like NMR. From this mixed system signal is obtained only from the deviation part, which is smaller by a factor of $\epsilon$ than if the system was in a pure state. In other words, if the deviation part of a mixed ensemble state ($\rho_{eq}$) is pure (see Eq. 1.61), the state is called a *pseudo-pure state*. Such proposal for simulating a pure state using an effective pure state was first put forward by Cory et al [44] and Chuang et al [45] in 1997. People have extensively used these states since then to simulate quantum information processing and computation in NMR for the last three decades [46]. As one can observe, a single qubit system is always in a pseudo-pure state. It has been established that for multi-qubit systems such pseudo-pure states can not be obtained from their corresponding thermal equilibrium states using only unitary operators. There are a number of procedures used to prepare PPS for multi-qubit systems. Here we describe two-qubit PPS preparation in detail.
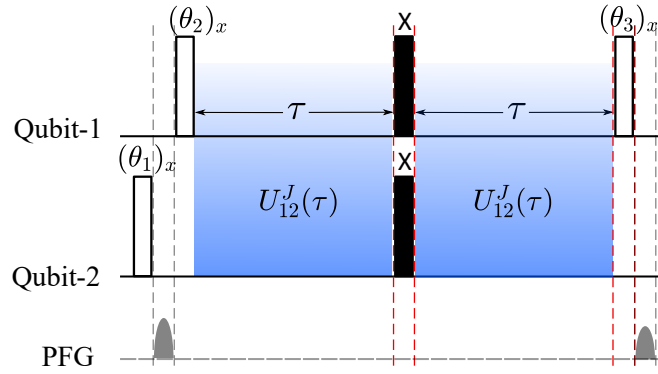


**Figure 1.10:** Pulse sequence for preparing two-qubit pseudo pure state. The pulses are time ordered from left to right. The black narrow bar represents $\pi$ angle pulse about the axis mentioned above it. The white narrow bars correspond to $\theta_i$ angle pulse about the axis mentioned in the subscript. $\tau = 1/2J_{12}$ is the time for each evolution under the interaction Hamiltonian given Eq. 1.51. The blue shaded region represent the evolution under the *J*-coupling Hamiltonian represented by $U_{12}^J(\tau)$. The dashed line corresponds to Pulse Field Gradient (PFG) to destroy *x-y* magnetization.

Considering two nuclear spins with gyromagnetic ratios $\gamma_1$ and $\gamma_2$, we wish to prepare a pseudo pure state from the thermal equilibrium state. Here using the deviation density matrix representation of the states, thermal equilibrium state and the PPS can be written as $\gamma_1 S_1^z + \gamma_2 S_2^z$

and $S_1^z + S_2^z + 2S_1^z S_2^z$ respectively. The pulse sequence for preparation of two qubit PPS is shown in Fig. 1.10. The values of $\theta_i$ depend upon the values of $\gamma_i$. For the case of $|\gamma_1/2| \leq |\gamma_2|$, $\theta_1 = \cos^{-1}(\gamma_1/2\gamma_2)$, $\theta_2 = \pi/4$ and $\theta_3 = \pi/4$. Where as if $|\gamma_1/2| > |\gamma_2|$, $\theta_1 = 0$, $\theta_2 = (1/2)\sin^{-1}(2\gamma_2/\gamma_1)$ [47]. One can find the experimental implementation of three and more qubit PPS in [48].

# CHAPTER 2

# Quantum heat-exchange fluctuation relation

**Abstract**

In this chapter we experimentally explore the validity of the Jarzynski and Wójcik quantum heat-exchange fluctuation relation (FR) by implementing an interferometric technique in liquid-state nuclear magnetic resonance setup and study the heat-exchange statistics between two coupled spin-1/2 quantum systems. We experimentally emulate two models—(i) the XY-coupling model, containing an energy conserving interaction between the qubits, and (ii) the XX-coupling model—and analyse the regimes of validity and violation of the fluctuation symmetry when the composite system is prepared in an uncorrelated initial state with individual spins prepared in local Gibbs thermal states at different temperatures. We further extend our analysis for heat exchange by incorporating correlation in the initial state. We support our experimental findings by providing exact analytical results. Our experimental approach is general and can be systematically extended to study heat statistics for more complex out-of-equilibrium many-body quantum systems.

## 2.1 Introduction

With the size of system that can be measured and controlled experimentally reaching the levels of single molecules or atoms, it is important to quantify thermal and quantum fluctuations in these nanoscale system from both fundamental and practical perspective [49]. People have tried to come up with theoretical frameworks, in the last few decades, to consistently describe these fluctuations. This has led to the development of so called *fluctuation relations* (FRs)

[30, 31, 33, 34, 50–62]. In quantum domain all the thermodynamic observables like work, heat, entropy etc. can be thought of as random variables, to which one can associate a probability distribution function. For these random variables, FRs provide relationship between their forward and time-reversed, backward probability distribution functions. These relations are universal and are found to hold in transient [33, 34, 52] as well as in steady-state regimes (i.e. equilibrium and non-equilibrium dynamics) [60, 61]. Different kinds of FRs have been proposed in the last two decades. The first such relation, given by Jarzynski, established a connection between the work in a classical non-equilibrium process and the produced free energy in the system. Later this was extended to quantum systems by Jarzynski and Crooks. A similar relation was proposed by Jarzynski and Wójcik for heat being exchanged between two quantum mechanical systems initialized at a thermal-equilibrium state at two different temperatures. This relation is called the Jarzynski-Wójcik heat *exchange fluctuation theorem* (XFT). In spite of the major theoretical work done in this field, experimental investigation and verification of such relations have been limited because of the challenge in measuring the *probability distribution functions* (PDFs) using two-point measurement technique, which relies on high fidelity projective measurements. In this work we use an interferometric technique to circumvent the projective measurement involved and, verify and study the quantum heat XFT.

## 2.2 Objectives

The objectives of this project was to explore validity of quantum version of Jarzynski-Wójcik XFT for two coherent quantum systems (qubits) using an ancilla based interferometric technique to extract the full heat exchange statistics [63–69] in an NMR architecture, for three different conditions:

- For energy preserving coupling Hamiltonian between the two heat exchanging quantum systems, which we call the $XY$-model.

- For energy non preserving coupling Hamiltonian, which we refer to as $XX$-model.

- And for correlated initial state.

These three conditions were chosen keeping in mind that while obtaining the expression for the XFT, Christopher Jarzynski and D. K. Wójcik in their work [52] assumed uncorrelated initial

states and weak coupling between the quantum systems exchanging heat. Interestingly it will be observed that for energy preserving coupling Hamiltonian i.e., when the coupling Hamiltonian commutes with the internal Hamiltonian of the system, XFT is valid for arbitrary coupling strength and that introducing a certain form of correlation into the system can cause spontaneous heat flow from cold to hot subsystem, thus displaying signatures of "Reversal of arrow of time".

## 2.3 Exchange Fluctuation Relation in Quantum Domain

Here we give a general explanation of the heat statistics and XFT for heat exchange between two quantum systems. We consider a bipartite system with internal Hamiltonians of the subsystems being, $H_1$ and $H_2$. Initially, $t = 0^-$, the two subsystems are not coupled to each other and are prepared in an uncorrelated pseudo thermal state, at respective inverse spin temperatures, $\beta_i$, $\rho_0 = \rho_1 \otimes \rho_2$ , where $\rho_i = exp[-\beta_i H_i]/Z_i$ is the Gibbs thermal state and $Z_i = \text{Tr}[exp[-\beta_i H_i]]$ represents the partition function of the subsystems, for $i = 1, 2$. At $t = 0$ the coupling Hamiltonian, $\mathcal{H}$, between them is switched on and the heat exchange is allowed for a duration of $t = \tau$. After which the interaction is switched off again. As we are dealing with evolution of quantum systems, the heat exchange is inherently nondeterministic and with the randomness in the initial state preparation, the heat exchange in this quantum scenario is a stochastic variable associated with a PDF. To find PDF of the heat exchange process one can use two-time projective measurement scheme [56, 57, 70], in which the system is measured once in the beginning and once in the end of the heat exchange process. One point to note here is that the two-time measurement scheme destroys any correlation in the initial state, thus taking care of uncorrelated initial state assumptions made by Jarzynski and Wójcik. For energy ($\Delta E_i$) exchanged between the two subsystems, the PDF can be written as

$$p_\tau(\Delta E_1, \Delta E_2) = \sum_{m,n} \Big( \prod_{i=1}^{2} \delta(\Delta E_i - (\epsilon_m^i - \epsilon_n^i)) \Big) p_{m|n}^\tau p_n^0. \tag{2.1}$$

Here $p_n^0 = \prod_{i=1}^{2} e^{-\beta_i \epsilon_n^i}/Z_i$ is the probability of finding the system initially in a common eigenstate $|n\rangle$ with eigenvalues $\epsilon_n^i$, after the first projective measurement. After the quantum evolution of the system under the unitary $\mathcal{U}(t, 0) = e^{-\frac{i}{\hbar}\mathcal{H}t}$, the second projective measurement is performed. The system thus collapses onto another set of common eigenstate, $|m\rangle$, with eigenvalue $\epsilon_m^i$ with

the probability $p^\tau_{m|n} = |\langle m|\mathcal{U}(\tau,0)|n\rangle|^2$. Using the form of Gibbs thermal state mentioned above and using the principle of micro-reversibility of quantum dynamics for autonomous system, i.e. $p^\tau_{m|n} = p^\tau_{n|m}$, we can rewrite Eq. 2.1 as

$$p_\tau(\Delta E_1, \Delta E_2) = e^{\beta_1 \Delta E_1 + \beta_2 \Delta E_2} \, p_\tau(-\Delta E_1, -\Delta E_2). \tag{2.2}$$

If the strength of coupling Hamiltonian between the two subsystems is much smaller than their internal Hamiltonian, i.e. *weak coupling regime*, the energy lost or gained by the two subsystems, $\Delta E_1 \approx -\Delta E_2 = Q$ can be interpreted as the heat exchanged between them. The Jarzynski and Wójcik quantum heat-exchange fluctuation relation can then be written as

$$p_\tau(Q) = \exp\left[(\beta_1 - \beta_2)Q\right] p_\tau(-Q). \tag{2.3}$$

It is this relation that we aim to experimentally verify for different regimes and initial condition. Rearranging the above equation and integrating both sides one can easily see that Eq. 2.3 can be written as $\langle e^{-\Delta\beta Q}\rangle_\tau = 1$, which is known as the integral form of the XFT, where $\langle ..\rangle_\tau$ represents the average over the distribution $p_\tau(Q)$ and $\Delta\beta = \beta_1 - \beta_2$. Experimentally it is quite challenging to obtain the PDFs directly, thus in this work the quantity of interest is the *characteristic function* (CF), which is defined as the Fourier transform of the PDF $p_\tau(Q)$ [71],

$$
\begin{aligned}
\chi_\tau(u) &= \int dQ \, e^{-iuQ} \, p_\tau(Q), \\
&= \mathrm{Tr}\Big[\mathcal{U}^\dagger(\tau,0)(e^{-iuH_1} \otimes 1_2)\mathcal{U}(\tau,0)(e^{iuH_1} \otimes 1_2)\rho_0\Big].
\end{aligned}
\tag{2.4}
$$

Here $u$ is the conjugate variable to $Q$, the heat energy exchanged. Experimentally we obtain the CF of the heat exchange between two quantum systems by using an ancilla based interferometric technique (see sec.2.4). The PDF is in turn obtained by the inverse Fourier transform of the CF. In what follows we describe the experimental implementation of this interferometric technique using NMR architecture to measure the CF and extract the PDF [67–69]. This experimentally obtained PDF is then used to investigate the XFT. As we will see, one of the advantages of using such an interferometric technique, over the previously used two-time measurement approach is that, it offers analysis of arbitrary initial state with correlations and even coherences, which is not possible with the two-time measurement approach. Along with this we are going to use the periodic property of the characteristic function, $\chi_\tau(u)$. Since $\chi_\tau(u)$ is the Fourier transform of

the PDF, one can write,

$$\chi_\tau(u) = \int dQ\, e^{-iuQ}\, p_\tau(Q) = \langle e^{-iuQ} \rangle.$$

$$= \langle e^{-iu(H_f - H_i)} \rangle.$$

$$= \langle \mathcal{U}^\dagger e^{-iuH_i} \mathcal{U} e^{iuH_i} \rangle. \tag{2.5}$$

Where we have used the interaction picture. As we will see in this work, the initial Hamiltonian of the subsystem is taken to be, $H_i = h\nu_0(\sigma^z/2)$. Using this one can write,

$$\chi_\tau(u + \frac{2\pi}{h\nu_0}) = \langle \mathcal{U}^\dagger e^{-iuH_i} e^{-i\pi\sigma^z} \mathcal{U} e^{iuH_i} e^{i\pi\sigma^z} \rangle.$$

$$= \langle \mathcal{U}^\dagger e^{-iuH_i} \mathcal{U} e^{iuH_i} \rangle. \tag{2.6}$$

Comparing Eq. 2.5 and 2.5 one can see $\chi_\tau(u) = \chi_\tau(u + \frac{2\pi}{h\nu_0})$ and thus characteristic function of the PDF of heat exchange between two quantum systems with product initial state is periodic.

## 2.4  System and Interferometric Technique

(a)                                    (b)



Hamiltonian Paramerters

| F$_1$ | F$_2$ | F$_3$ | Hz |
|---|---|---|---|
| 1000 | -128.3 | 69.9 | F$_1$ |
| | -16330 | 47.4 | F$_2$ |
| | | 12839 | F$_3$ |

1,1,2-Trifluoro-2-iodoethane
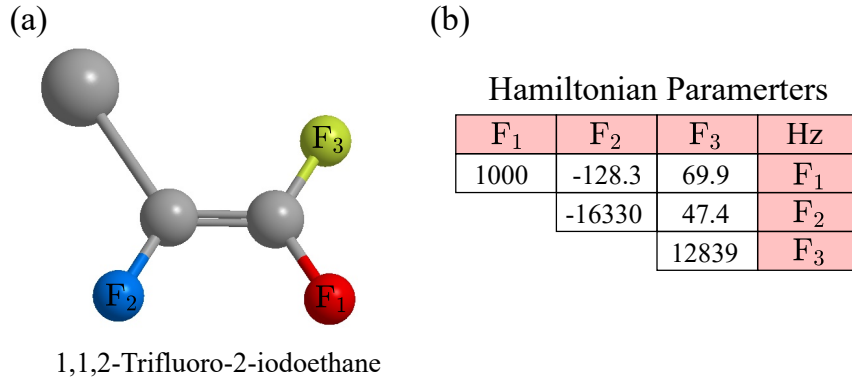
**Figure 2.1:** (a) Structure of the molecule 1,1,2-Trifluoro-2-iodoethane. (b) Parameters of the Hamiltonian in Eq. 2.7. The diagonal terms represent $\nu_i$ and the off-diagonal terms $J_{ij}$.

In our experiments, we use liquid-state NMR spectroscopy of three $^{19}$F nuclei (F$_1$, F$_2$ and F$_3$) in $1, 1, 2-$Trifluoro$-2-$iodoethane (TFIE) (Fig.2.1(a)), dissolved in Acetone as a test-bed to study the heat flow between quantum systems. All our experiments are performed in 500 MHz Bruker NMR spectrometer at an ambient temperature. Below we explain the experimental system

used and the interferometric protocol used to extract the CF of this heat flow.

## 2.4.1 Experimental Setup

The three NMR active $^{19}$F nuclei in the molecule, labelled as $F_1$, $F_2$ and $F_3$ and we identify $F_1$ as qubit 1, $F_2$ as qubit 2 and $F_3$ as the ancillary qubit. The molecules in the sample are all identical and sufficiently isolated [38, 40, 72] and all the dynamics and heat exchange processes are completed in the time scale of milliseconds, such that any relevant environmental effects can be neglected. Note that, the longitudinal and transverse relaxation time constants in our NMR setup are in fact of the order of few seconds.

The internal Hamiltonian ($H_{\text{int}}$) of the three spin system in the rotating frame of the radio frequency (RF) pulses can be written as (see ch.1)

$$H_{\text{int}} = \sum_{i=1}^{3} \frac{h\nu_i}{2}\sigma_i^z + \sum_{i<j=1}^{3} \frac{hJ_{ij}}{4}\sigma_i^z\sigma_j^z, \tag{2.7}$$

where $\nu_i$ is the off-set frequency of $i$-th nuclei and $J_{ij}$ being the scalar coupling between $i$-th and $j$-th nuclei. Values of these internal Hamiltonian parameters are shown in Fig. 2.1(b). The diagonal terms represent the value of $\nu_i$s and the off-diagonal terms are the scalar coupling, $J_{ij}$. $F_1$ and $F_2$ exchange heat by interacting under a constant coupling Hamiltonian. To study the heat flow between these two quantum systems we consider two different coupling models for which we go about investigating XFT. In the first model, net Hamiltonian is of the form,

$$\mathcal{H} = H_1 + H_2 + \frac{hJ}{4}\left(\sigma_1^x \otimes \sigma_2^y - \sigma_1^y \otimes \sigma_2^x\right), \tag{2.8}$$

We refer to this as $XY$-model. The other model, referred to as $XX$- model, is given by,

$$\mathcal{H} = H_1 + H_2 + \frac{hJ}{4}\sigma_1^x \otimes \sigma_2^x, \tag{2.9}$$

where $H_1 = \frac{-h\nu_0}{2}\sigma_1^z \otimes \mathbb{1}_2$, and $H_2 = \mathbb{1}_1 \otimes \frac{-h\nu_0}{2}\sigma_2^z$. $\sigma^i(i=x,y,z)$ is the $i$-th component of Pauli spin-1/2 operator.

Recall that, we are interested in extracting the statistics of heat flowing between the qubits $F_1$ and $F_2$ by measuring the CF, $\chi_\tau(u)$, as given in Eq. 2.4. The quantum circuit for doing so is shown in Fig. 2.2. For the first set of experiments for both these models we consider uncorrelated (product) initial state for the qubits. This is achieved by first initializing the three qubit system
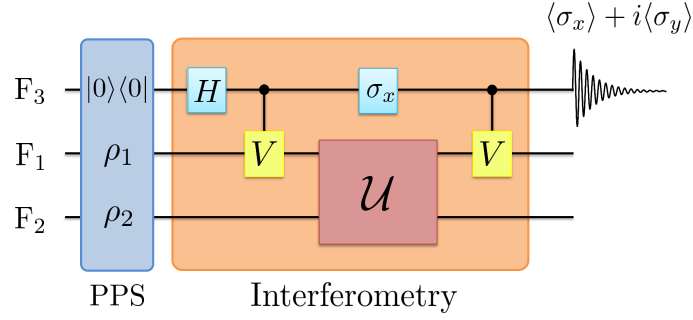
**Figure 2.2:** Circuit diagram for the interferometric technique to measure the CF of heat $\chi_\tau(u)$. Here, $H$ is the Hadamard gate applied on the ancillary qubit, initially prepared in the $|0\rangle\langle 0|$ state, followed by a control gate $V = \exp\left[-iuH_1\right] \otimes 1_2$ on the qubit $F_1$ and $\mathcal{U} = \exp\left[-i\mathcal{H}t\right]$ is the unitary propagator where $\mathcal{H}$ represents the Hamiltonian of the composite system for $XY$ model (Eq. 2.8) or for the $XX$ model (Eq. 2.9). $\rho_1, \rho_2$ are the initial states of $F_1$ and $F_2$, respectively. The readout of $\langle\sigma_x\rangle + i\langle\sigma_y\rangle$ component of the ancilla finally gives us the CF $\chi_\tau(u)$

in a pseudo-pure $|000\rangle\langle 000|$ state [47] (see Ch.1), followed by preparing $F_1$ and $F_2$ in a pseudo thermal-equilibrium state, $\rho_{in} = \rho_1 \otimes \rho_2$, where $\rho_i = \exp\left[-\beta_i H_i\right]/\mathcal{Z}_i$ being the Gibbs thermal state with inverse pseudo spin temperatures $\beta_i$. In our experiments, we realize different pseudo spin temperatures by applying RF pulses from 0 to $\pi/2$ that redistribute the population between the qubit states followed by a Pulsed Field Gradient (PFG) which destroys the coherences and produces a desired thermal initial state. Note that the pseudo spin temperature is different from the actual sample temperature which is always maintained at an ambient temperature.

With this initial state the interferometric protocol is implemented, as shown in the Fig. 2.2, to obtain the desired CF, $\chi_\tau(u)$, for heat exchange between $F_1$ and $F_2$ under the unitary evolution $\mathcal{U} = \exp\left[-\frac{i}{\hbar}\mathcal{H}t\right]$. The interferometric circuit in Fig. 2.2 maps the CF of the heat exchange onto the ancillary qubit $F_3$. Various gates used for this protocol such as the Hadamard gate $H$, controlled gate $V = \exp\left[-i\,u\,H_1\right] \otimes 1_2$ and $\mathcal{U}$, responsible for the heat exchange between the qubits, are prepared by utilizing the internal Hamiltonian, $H_{int}$, (Eq. 2.7) and the RF pulses (see Ch.1 for examples). For the realization of controlled gate, $V = \exp\left[-i\,u\,H_1\right] \otimes 1_2$, we use a Gradient Accent Pulse Engineering protocol [73] along with an optimization procedure (Genetic Algorithm) [74].
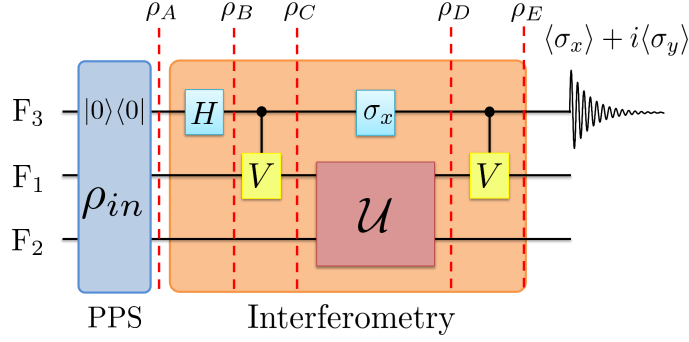
**Figure 2.3:** Circuit diagram for the interferometric technique to measure the CF of heat $\chi_\tau(u)$. $\rho_i, (i = A, B, C, D, E)$ represents the intermediate states of the global system (F$_1$, F$_2$, F$_3$) after gate operations.

## 2.4.2 Interferometric Protocol

Here we summarize the interferometric technique [64, 65] to obtain the CF for heat as given in Eq. 2.4. We begin with the initial state of the three qubit system $|0\rangle\langle 0| \otimes \rho_{\text{in}}$, where $\rho_{in}$ is an arbitrary initial state (may or may not include quantum correlations) for the two qubits, $F_1$ and $F_2$, that exchange heat and $|0\rangle\langle 0|$ is the state for the ancillary qubit. Following Fig. 2.3, the global density operator in the ancillary basis can thus be written as,

$$\rho_A = \begin{bmatrix} \rho_{\text{in}} & 0 \\ 0 & 0 \end{bmatrix}.$$

Next a Hadamard gate, $H$, is applied on the ancillary qubit. The density matrix can then be written as,

$$\rho_B = H\rho_A H^\dagger = \frac{1}{2} \begin{bmatrix} \rho_{\text{in}} & \rho_{\text{in}} \\ \rho_{\text{in}} & \rho_{\text{in}} \end{bmatrix}.$$

This is followed by application of a controlled gate $V = \exp\left[-i\,u\,H_1\right] \otimes 1_2$ on the qubit $F_1$. At this stage we get,

$$\rho_C = \frac{1}{2} \begin{bmatrix} \rho_{\text{in}} & \rho_{in}V^\dagger \\ V\rho_{\text{in}} & V\rho_{in}V^\dagger \end{bmatrix}$$

Following the circuit in Fig. 2.3 the system is evolved under the heat exchange unitary propagator $\mathcal{U}$, along with a $\sigma_x$ rotation on the ancillary qubit. This gives us

$$\rho_D = \frac{1}{2} \begin{bmatrix} \mathcal{U}V\rho_{\text{in}}V^\dagger\mathcal{U}^\dagger & \mathcal{U}V\rho_{\text{in}}\mathcal{U}^\dagger \\ \mathcal{U}\rho_{\text{in}}V^\dagger\mathcal{U}^\dagger & \mathcal{U}\rho_{\text{in}}\mathcal{U}^\dagger. \end{bmatrix}$$

In the final step, the controlled gate $V_1$ is applied once again on the qubit $F_1$. The final global density matrix can then be written as,

$$\rho_E = \frac{1}{2} \begin{bmatrix} \mathcal{U}V\rho_{\text{in}}V^\dagger\mathcal{U}^\dagger & \mathcal{U}V\rho_{\text{in}}\mathcal{U}^\dagger V^\dagger \\ V\mathcal{U}\rho_{\text{in}}V^\dagger\mathcal{U}^\dagger & V\mathcal{U}\rho_{\text{in}}\mathcal{U}^\dagger V^\dagger \end{bmatrix}$$

At this stage if we trace-out $F_1$ and $F_2$ qubit, the reduced density matrix for $F_3$ takes the form,

$$\rho = \text{Tr}_{1,2}[\rho_E] = \frac{1}{2} \begin{bmatrix} 1 & \text{Tr}\big[\mathcal{U}V\rho_{\text{in}}\mathcal{U}^\dagger V^\dagger\big] \\ \text{Tr}\big[V\mathcal{U}\rho_{\text{in}}V^\dagger\mathcal{U}^\dagger\big] & 1 \end{bmatrix}$$

The off-diagonal components of this density matrix are simply related to the expectation values of the $\sigma_x$ and $\sigma_y$ components for the ancilla. We can therefore write,

$$\langle\sigma_x\rangle_\rho + i\langle\sigma_y\rangle_\rho = \text{Tr}\big[V\mathcal{U}\rho_{in}V^\dagger\mathcal{U}^\dagger\big],$$
$$= \text{Tr}\big[V^\dagger\mathcal{U}^\dagger V\mathcal{U}\rho_{in}\big],$$
$$= \text{Tr}\big[\big(e^{iuH_1}\otimes 1_2\big)\mathcal{U}^\dagger\big(e^{-iuH_1}\otimes 1_2\big)\mathcal{U}\rho_{\text{in}}\big],$$
$$= \text{Tr}\big[\mathcal{U}^\dagger\big(e^{-iuH_1}\otimes 1_2\big)\mathcal{U}\rho_{\text{in}}\big(e^{iuH_1}\otimes 1_2\big)\big]. \tag{2.10}$$

Note that, the above final expression is not yet the CF of heat as obtained in Eq. 2.4, following the two-time measurement protocol. It is only when the initial state, $\rho_{in}$ for $F_1$ and $F_2$, is an uncorrelated (product) Gibbs state i.e., $\rho_{\text{in}} = \rho_0 = \exp[-\beta_1 H_1]/Z_1 \otimes \exp[-\beta_2 H_2]/Z_2$, implying $[\rho_0, H_1 \otimes 1_2] = 0$, that Eq. 2.10 reduces to

$$\langle\sigma_x\rangle_\rho + i\langle\sigma_y\rangle_\rho = \text{Tr}\big[\mathcal{U}^\dagger\big(e^{-iuH_1}\otimes 1_2\big)\mathcal{U}\big(e^{iuH_1}\otimes 1_2\big)\rho_0\big], \tag{2.11}$$

which is exactly the CF $\chi_\tau(u)$ in Eq. 2.4.

It is important to note here, even for arbitrary initial condition Eq. 2.10 may not deliver the correct PDF of heat, as it is not guaranteed to be always positive definite. As it will be shown, interestingly the CF at least produces the correct definition for the first moment i.e., the average

heat $\langle Q \rangle = \langle H_f \rangle - \langle H_i \rangle$, even if the initial state is not a separable product state.

## 2.5 Results and Discussion

In this section we finally show and discuss the experimental results for the two different type of couplings models, $XY$ and $XX$, for initially uncorrelated state and also for the special case of initially correlated state.

### 2.5.1 $XY$-coupling model
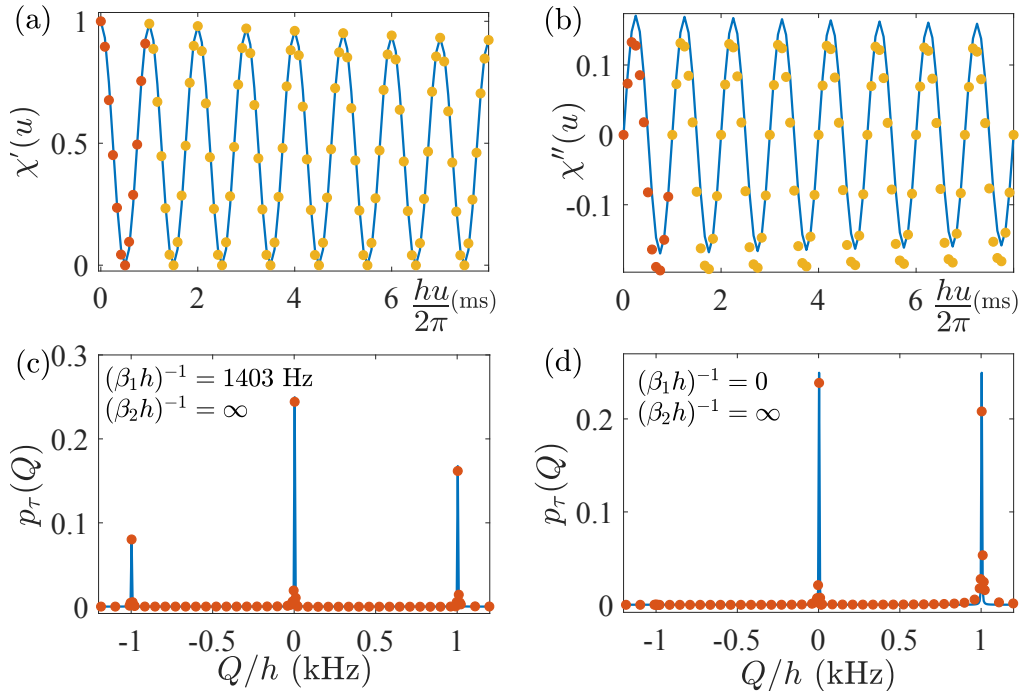


**Figure 2.4:** Results for the XY-model (a)-(b): Plots for the real ($\chi'_\tau(u)$) and imaginary ($\chi''_\tau(u)$) components of the CF $\chi_\tau(u)$. Solid (blue) lines and the dots correspond to theoretical and experimental results, respectively. (c)-(d): The PDF of heat exchange $p_\tau(Q)$ for two different values of $\beta_1$ as shown.

For this particular model, we set the frequency for the qubits $F_1$ and $F_2$ as $\nu_0 = 1$ kHz and the coupling $J$ is chosen as 1 Hz, which ensures the weak-coupling ($J \ll \nu_0$) between the qubits. For the initial state preparation, we initialize $F_2$ at infinite pseudo spin temperature [75], $(\beta_2 h)^{-1} = \infty$. This is achieved by applying a $\pi/2$ pulse on $F_2$ followed by a Pulsed Field Gradient (PFG). For $F_1$, we prepare the qubit at different pseudo spin temperatures by applying

RF pulses from 0 to $\pi/2$ followed by a PFG. We then measure $\chi_\tau(u)$ by allowing heat exchange between $F_1$ and $F_2$ for a time duration $\tau = \pi/J$, corresponding to the maximum average heat exchange between the two qubits. In Fig. 2.4(a-b) we display both experimental and theoretical results for the real and imaginary components of the CF $\chi_\tau(u)$ when F$_1$ is at a particular pseudo spin temperature $(\beta_1 h)^{-1} = 1403$ Hz. We take a set of measurements in one complete period of $u \in [0, \frac{2\pi}{h\nu_0}]$ (red dots in Fig.2.4(a-b)) and further take advantage of the periodicity of the CF $\chi_\tau(u) = \chi_\tau(u + \frac{2\pi}{h\nu_0})$ (see Eq. 2.5 and 2.5) to extrapolate (orange dots in Fig.2.4(a-b)) the obtained data for subsequent periods. We phenomenologically add a small constant damping factor to $\chi_\tau(u)$ with decay constant $10$ Hz in both theoretical and experimental data. The inverse Fourier transform of the obtained CF produces the desired PDF $p_\tau(Q)$ which shows three distinct peaks at $Q/h = \pm 1\,\text{kHz}$ and $Q/h = 0$ Hz and with finite widths proportional to the decay constant. The corresponding peak amplitudes reflect the probability of heat flowing from one qubit to another. The location of the peaks can be understood from the energy eigenvalues of the composite Hamiltonian $\mathcal{H}$ (Eq. 2.8). The $\pm 1$ kHz peaks corresponds to the transition between the zero energy states and the highest or lowest energy states. The corresponding probabilities are proportional to $\frac{1}{2}\sin^2\left(\frac{J\tau}{2}\right) \times 1/(\exp(\mp\beta_1 h\nu_0)+1)$ (see Eq. 2.14). The peak at $Q = 0$ represents no heat exchange process between the qubits and in this particular scenario, it's peak amplitude is independent of the pseudo spin temperatures and is proportional to $\frac{1}{2}\left(1 + \cos^2\left(\frac{J\tau}{2}\right)\right)$, (see Eq. 2.15). Note that, as per our convention, positive value of $Q$ corresponds to heat flowing from $F_2$ to $F_1$ and vice versa. Fig. 2.4(c) therefore confirms that on an average heat flows from hot qubit F$_2$ to cold qubit F$_1$ and thereby validates the second law of thermodynamics at the level of ensemble average. However, at the microscopic realm, a finite probability corresponding to heat flowing from cold to hot exists which contributes to negative entropy production. With reduction in the pseudo spin temperature $(\beta_1 h)^{-1}$ the peak value at $Q/h = -1$ kHz reduces and finally disappears completely for $(\beta_1 h)^{-1} = 0$ (Fig. 2.4(d)).

In contrast, as the temperature of $F_1$ increases (Fig. 2.5(a-c)) the probability of back-flow of heat from F$_1$ to F$_2$ increases, and the peak value at $Q/h = -1$ kHz increases which becomes exactly equal to the peak value at $Q/h = 1$ kHz at $(\beta_1 h)^{-1} = (\beta_2 h)^{-1} = \infty$ and thus ensuring zero net heat exchange. The temperatures of the two subsystems are given in Fig. 2.5(a-c). All the other parameters are kept the same as before. We next plot $\ln\left[p_\tau(Q)/p_\tau(-Q\right]$ against $Q$ for the
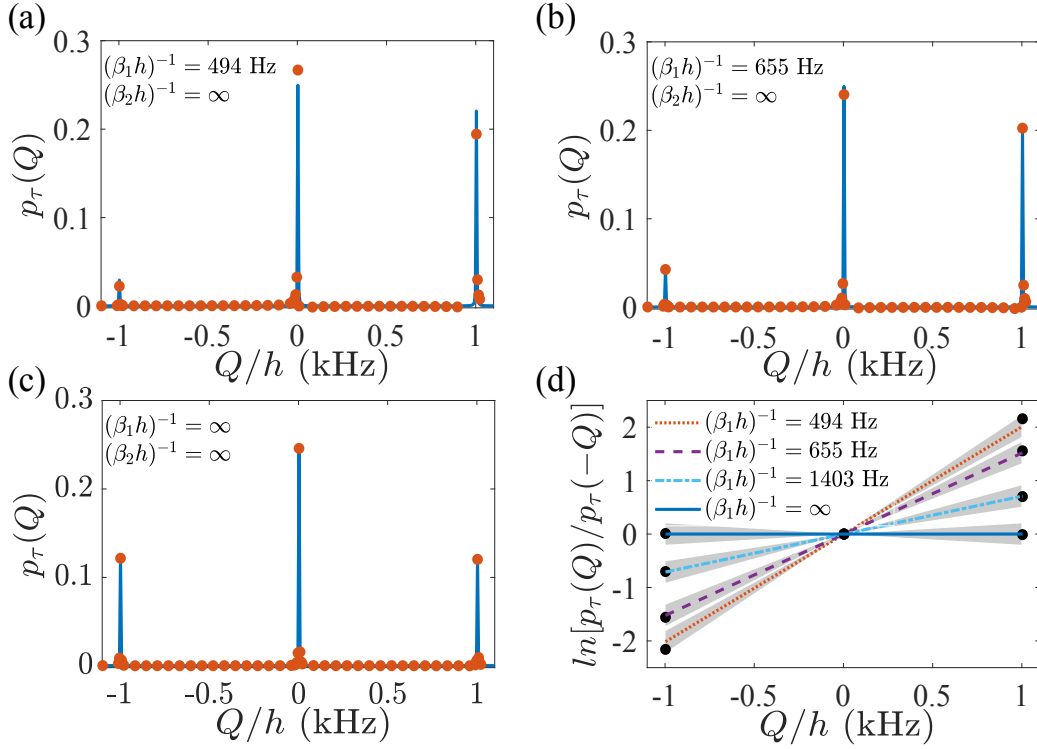
**Figure 2.5:** (a)-(c): PDF of heat exchange for XY-model for different spin temperatures of $F_1$. Solid (blue) lines and the red dots correspond to theoretical and experimental results, respectively. (d): Verification of Jarzynski and Wöjcik heat XFT– plots for $\ln\left[p_\tau(Q)/p_\tau(-Q)\right]$ as a function of $Q/h$ for four different temperatures of $F_1$. The shaded region indicate the simulated 5% pulse errors in the experiment. All other parameters are the same as in Fig. (2.4)

above four sets of pseudo spin temperatures to confirm the Jarzynski and Wöjcik XFT. Note that, as the coupling Hamiltonian in Eq. 2.8 is a constant one, $p_\tau(-Q)$ is obtained simply by flipping the forward PDF $p_\tau(Q)$. Fig. 2.5(d) shows excellent agreement between the theoretical and the experimentally obtained results with the expected slope equal to $\Delta\beta = \beta_1 - \beta_2$. The shaded regions indicate simulated results that involve $\pm 5\%$ random errors in all the RF pulses used in the interferometric technique as well as in the initial state preparation. In table 2.1 we tabulate both theoretical and experimentally extracted values of these slopes.

It is experimentally possible to further tune the coupling $J$ to explore the heat statistics and the corresponding XFT from moderate to strong coupling regime. However, for the $XY$ coupling model as has been mention earlier, the coupling Hamiltonian (Eq. 2.8) $H_{12} = \frac{hJ}{4}\left(\sigma_1^x \otimes \sigma_2^y - \sigma_1^y \otimes \sigma_2^x\right)$ commutes with the total bare Hamiltonian of the two qubits $H_1 + H_2$. Which implies that coupling Hamiltonian $H_{12}$ represents an energy preserving interaction and there is no energy cost involved

**Table 2.1:** Table containing theoretical and experimentally obtained values for the slope $\Delta\beta = \beta_1 - \beta_2, \beta_i = 1/k_B T_i$ from (d). All other parameters are the same as in Fig. (2.4).

| $(\beta_1 h)^{-1}$ **(Hz)** | **Theory** $\Delta\beta$ **(kHz)**$^{-1}$ | **Experiment** $\Delta\beta$ **(kHz)**$^{-1}$ |
|---|---|---|
| 494 | 2.02 | $2.15 \pm 0.08$ |
| 655 | 1.52 | $1.55 \pm 0.03$ |
| 1403 | 0.71 | $0.71 \pm 0.01$ |

in turning the interaction on or off between the two qubits. As a result the energy change in one subsystem, qubit 1, is equal and opposite to the change in the other subsystem, qubit 2, i.e., $\Delta E_1 = -\Delta E_2$. This is be further shown as below,

$$\mathcal{H} = H_1 + H_2 + H_{12}$$
$$\Rightarrow \frac{d\mathcal{H}}{dt} = \frac{dH_1}{dt} + \frac{dH_2}{dt} + \frac{dH_{12}}{dt} = 0$$
$$= \frac{dH_1}{dt} + \frac{dH_2}{dt} - \frac{i}{\hbar}[H_1 + H_2, H_{12}] = 0$$

where the Von Neumann equation has been used in the third line. Since $[H_1 + H_2, H_{12} = 0]$ one can clearly see that the energy change in qubit 1 and 2 are equal and opposite. The main reason for Christopher Jarzynski and D. K. Wójcik to assume weak coupling for XFT in their work [52] was to satisfy $\Delta E_1 \approx -\Delta E_2$. But with the energy preserving coupling Hamiltonian, as explained above, XFT for heat exchange is valid for any $J$ value. We now present here the proof by providing the exact analytical expression for the CF and the corresponding PDF $p_\tau(Q)$.

Following the form of the characteristic function in Eq. 2.4 and the Hamiltonian in Eq. 2.8, one can perform simple algebraic manipulations of the Pauli matrices to get an exact expression for $\chi_\tau(u)$ as,

$$\chi_\tau(u) = \left[ 1 + \sin^2\left(\frac{J\tau}{2}\right) \left\{ f_1(\nu_0)\left(1 - f_2(\nu_0)\right)\left(e^{ihu\nu_0} - 1\right) \right. \right.$$
$$\left. \left. + f_2(\nu_0)(1 - f_1(\nu_0))\left(e^{-ihu\nu_0} - 1\right) \right\} \right] \tag{2.12}$$

where the function $f_i(\nu_0) = 1/(\exp(\beta_i h\nu_0) + 1), i = 1, 2$ is evaluated at the inverse temperature $\beta_i$ and qubit frequency $\nu_0$. Since we take $(\beta_2 h)^{-1} = \infty$, it is easy to see that $f_2 = 1/2$. Note that, the CF has the periodicity $\chi_\tau(u) = \chi_\tau(u + \frac{2\pi}{h\nu_0})$. Furthermore, as pointed out before, the above $\chi_\tau(u)$ follows the fluctuation symmetry $\chi_\tau(u) = \chi_\tau(-u + i\Delta\beta)$ for arbitrary coupling strength

$J$ as well as for arbitrary values of $\beta_1, \beta_2$, and $\nu_0$.

The corresponding probability distribution function of heat $p_\tau(Q)$ can be simply extracted by performing the inverse Fourier transformation of $\chi_\tau(u)$,

$$
\begin{aligned}
p_\tau(Q) &= \int_{-\infty}^{\infty} du\, e^{iuQ}\, \chi_\tau(u) \\
&= p_{0,\tau} \int_{-\infty}^{\infty} du\, e^{iuQ} + p_{+,\tau} \int_{-\infty}^{\infty} du\, e^{iu(Q-h\nu_0)} + p_{-,\tau} \int_{-\infty}^{\infty} du\, e^{iu(Q+h\nu_0)} \\
&= p_{0,\tau}\delta(Q) + p_{+,\tau}\delta(Q-h\nu_0) + p_{-,\tau}\delta(Q+h\nu_0).
\end{aligned}
\tag{2.13}
$$

This expression clearly shows three distinct peaks for $p_\tau(Q)$ at $Q/h = 0, \pm\nu_0$, reflecting different heat exchange processes between the qubits. These results excellently corroborate with our experimental plots as displayed in Fig. 2.4 and 2.5. In Eq. 2.13 $p_{+,\tau}$ and $p_{-,\tau}$ corresponds to the probability of heat absorbed and heat released by qubit $F_1$, respectively, and are obtained from $\chi_\tau(u)$ as,

$$
\begin{aligned}
p_{+,\tau} &= \sin^2\left(\frac{J\tau}{2}\right) f_2(\nu_0)(1 - f_1(\nu_0)), \\
&= \frac{1}{2}\sin^2\left(\frac{J\tau}{2}\right) \times 1/(\exp(-\beta_1 h\nu_0) + 1) \\
p_{-,\tau} &= \sin^2\left(\frac{J\tau}{2}\right) f_1(\nu_0)(1 - f_2(\nu_0)) \\
&= \frac{1}{2}\sin^2\left(\frac{J\tau}{2}\right) \times 1/(\exp(\beta_1 h\nu_0) + 1),
\end{aligned}
\tag{2.14}
$$

where we have used the fact that $f_2 = 1/2$. Also since the total probability has to be conserved,

$$
\begin{aligned}
p_{0,\tau} &= 1 - p_{+,\tau} - p_{-,\tau} \\
&= 1 - \sin^2\left(\frac{J\tau}{2}\right)\left(f_1(\nu_0) + f_2(\nu_0) - 2f_1(\nu_0)f_2(\nu_0)\right) \\
&= 1 - \frac{1}{2}\sin^2\left(\frac{J\tau}{2}\right) \\
&= \frac{1}{2}(1 + \cos^2\left(\frac{J\tau}{2}\right)),
\end{aligned}
\tag{2.15}
$$

Here, $p_{0,\tau}$ corresponds to the probability of no heat exchange between the qubits. It is easy to check that $p_{+,\tau}$ and $p_{-,\tau}$ are related via the fluctuation symmetry $p_{+,\tau} = e^{(\beta_1 - \beta_2)h\nu_0}p_{-,\tau}$. To further connect these analytical results to our experimental findings, in the limit when $(\beta_2 h)^{-1} = \infty$ and $(\beta_1 h)^{-1} = 0$, one finds following Eq. 2.14 that $p_{-,\tau}$ vanishes which indicate no back flow of heat from $F_1$ to $F_2$. This outcome is confirmed in Fig. 2.4(d) as the absence of the peak

at $Q/h = -\nu_0$. With increasing $(\beta_1 h)^{-1}$, the probability of back flow increases and finally in equilibrium ($\beta_1 = \beta_2$) the forward and backward flow becomes identical ($p_{-,\tau} = p_{+,\tau}$) confirming zero net heat exchange between the qubits. These predictions are also reflected in Fig. 2.5(a-c).

In what follows, we experimentally emulate the XX model which lacks the energy preserving symmetry between the qubits and investigate it's consequence on heat statistics and corresponding XFT.
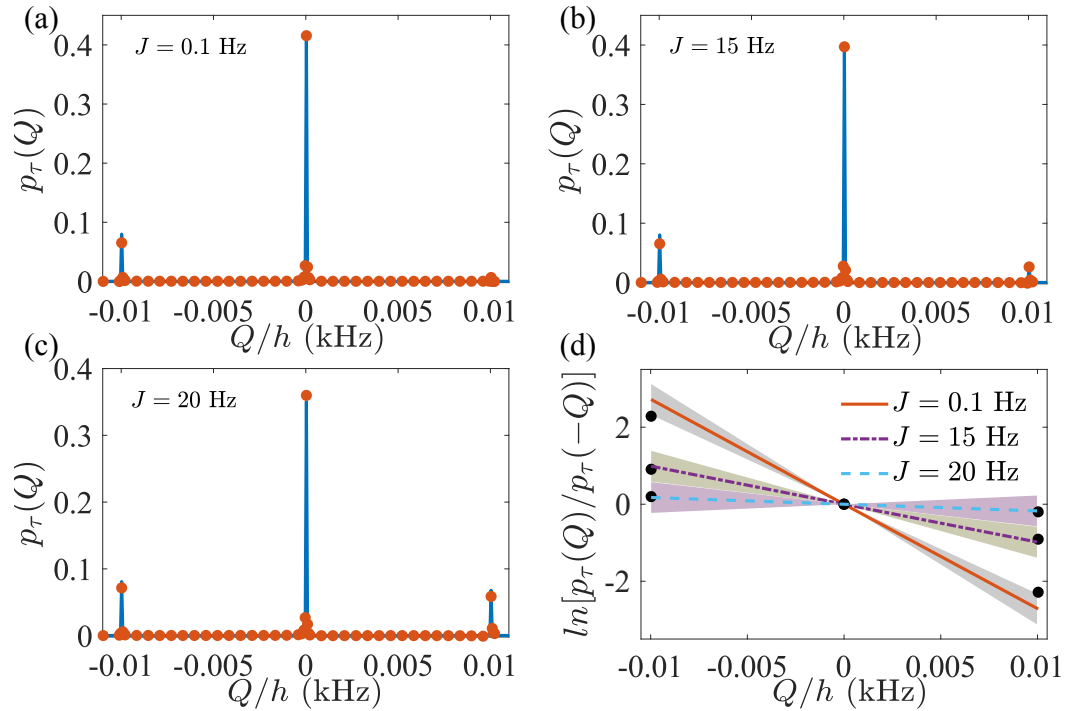
## 2.5.2  $XX$-coupling model



**Figure 2.6:** (a)-(c): PDF of heat exchange for XX-model for $\nu_0 = 10$Hz and for three different values of coupling strength, $J$ and for a fixed temperatures of the qubits. Solid (blue) lines and the dots correspond to theoretical and experimental results, respectively. (d): Plots for $\ln\left[p_\tau(Q)/p_\tau(-Q)\right]$ as a function of $Q$ for different coupling strengths. The shaded region indicates simulated $5\%$ pulse errors in the experiments.

In Fig. 2.6 the experimental results for the $XX$-model is shown. Unlike previous case the $XX$-model coupling Hamiltonian, Eq. 2.9, does not commute with the internal Hamiltonian of the system. As a result XFT for this model should only be valid in the weak coupling regime. As before, we follow similar experimental approach and set the frequency of the qubits to $\nu_0 = 10$ Hz but now tune $J$ from $0.1$ Hz upto $20$ Hz to simulate $p_\tau(Q)$ from weak to strong coupling regime for a fixed temperatures for the qubits exchanging heat, $(\beta_1 h)^{-1} = 1403$ Hz and $(\beta_2 h)^{-1} = 288$

Hz and obtain the $p_\tau(Q)$ corresponding to a fixed time duration $\tau = \pi/J$. The PDF's $p_\tau(Q)$ for different values of $J$ are shown in Fig. 2.6(a)-(c). The trend for the distribution is similar to the earlier case, with three distinct peaks at $Q = 0$, and $Q/h = \pm\nu_0$. Note that, as the temperature of the qubits exchanging heat is fixed, slope of the line in plot for $\ln\left[p_\tau(Q)/p_\tau(-Q)\right]$ against $Q$, should remain unchanged with the change in the coupling strength $J$ if the XFT holds. However, the corresponding plot for $\ln\left[p_\tau(Q)/p_\tau(-Q)\right]$ against $Q$ in Fig. 2.6(d) shows a clear violation of the XFT, except for the value of $J = 0.1$ Hz. For $J = 0.1$ Hz $\ll \nu_0 = 10$ Hz (weak coupling) the obtained slope from the experimental data (black dots) matches very closely to the expected $\Delta\beta$ value (solid line). However, for moderate ($J = 15$ Hz) to strong coupling, ($J = 20$ Hz), the experimental results (black dots) deviates significantly from the theoretical $\Delta\beta$ value (solid line) which is a clear indication of the breakdown of standard XFT. This breakdown can be attributed to the energy non-conserving coupling term in the XX model, as we show below.

To verify the XFT for this model, one can follow a similar approach as the XY model to obtain an analytical expression for the CF $\chi_\tau(u)$. However, instead of the CF, we provide here an expression for the deviation term of XFT i.e., $\langle e^{-\Delta\beta Q}\rangle_\tau - 1$ which captures the essential details about the violation. We receive,

$$\langle e^{-\Delta\beta Q}\rangle_\tau - 1 = -\frac{J^2}{J^2 + 16\,\nu_0^2}\sin^2\left(\frac{\tau}{4}\sqrt{J^2 + 16\,\nu_0^2}\right) h(\beta_1, \beta_2, \nu_0), \qquad (2.16)$$

where the function $h(\beta_1, \beta_2, \nu_0)$ is defined as

$$h(\beta_1, \beta_2, \nu_0) = \frac{1 + e^{\beta_1 h\nu_0} - e^{\beta_2 h\nu_0} - e^{(\beta_1 - \beta_2)h\nu_0}}{(e^{\beta_1 h\nu_0} + 1)}. \qquad (2.17)$$

Note that the standard version of XFT imply $\langle e^{-\Delta\beta Q}\rangle_\tau = 1$. The additional contribution in Eq. 2.16 therefore reflects the deviation from XFT. This term yield a negligible contribution only in the weak coupling limit $J \ll \nu_0$ which then reproduces the XFT for arbitrary $\tau$. However, from moderate ($J \approx \nu_0$) to strong coupling ($J \gg \nu_0$) this term dominates, leading to the breakdown of XFT as also observed experimentally. Note that, this deviation term is in fact related to the total change in energy of the two qubits, and thereby linked to the energy non-conserving coupling

term $H_{12} = \frac{hJ}{4}\sigma_x^1 \otimes \sigma_x^2$. We receive,

$$\langle\Delta E_1\rangle_\tau + \langle\Delta E_2\rangle_\tau = \frac{i}{h}\int_0^\tau dt \left\langle \left[H_{12}, H_1 + H_2\right]\right\rangle,$$

$$= h\nu_0 \frac{J^2}{J^2 + 16\,\nu_0^2}\,\sin^2\left(\frac{\tau}{4}\sqrt{J^2 + 16\,\nu_0^2}\right) g(\beta_1, \beta_2, \nu_0) \tag{2.18}$$

where $\langle\Delta E_i\rangle_\tau$ is the net energy change of $i$-th qubit in the time duration $\tau$ and the function $g(\beta_1, \beta_2, \nu_0)$ is given as,

$$g(\beta_1, \beta_2, \nu_0) = \frac{2\left(e^{(\beta_1+\beta_2)h\nu_0} - 1\right)}{\left(e^{\beta_1 h\nu_0} + 1\right)\left(e^{\beta_2 h\nu_0} + 1\right)}. \tag{2.19}$$

Comparison of Eq. 2.16 and Eq. 2.18 clearly shows the link between the energy non-conserving interaction and the deviation of XFT.

### 2.5.3   Correlated initial state
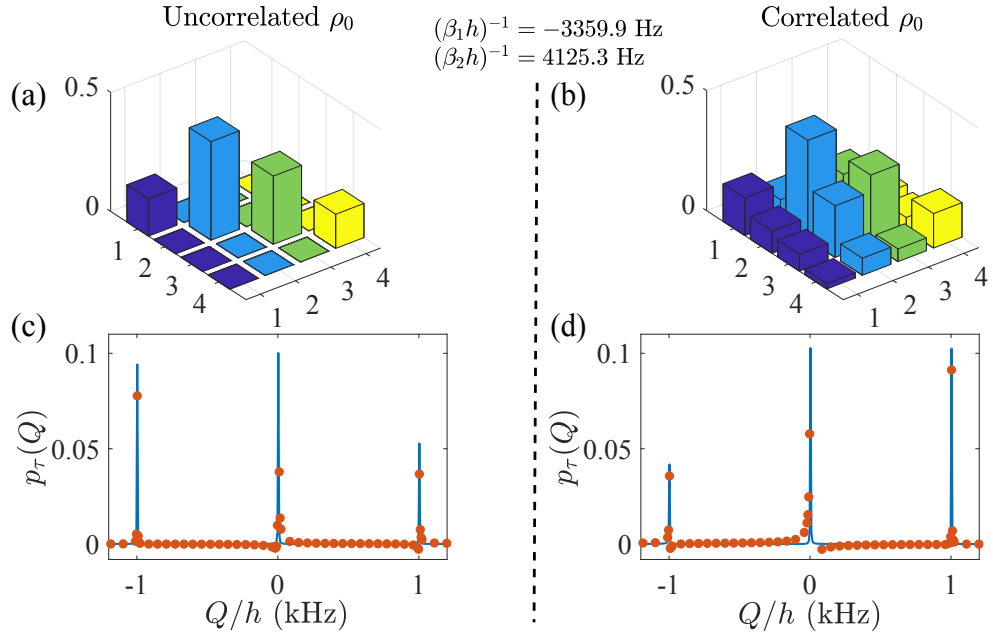


**Figure 2.7:** Absolute values for the density matrix elements for the composite system $F_1$ and $F_2$ for XY model for (a) uncorrelated ($\rho_0 = \rho_1 \otimes \rho_2$) and (b) correlated ($\rho_0 \neq \rho_1 \otimes \rho_2$) initial state. (c)-(d): Comparison between the corresponding heat exchange PDF's $p_\tau(Q)$. Solid (blue) lines and dots represent theoretical and experimental results, respectively.

We next direct our attention towards exploring heat statistics for correlated initial state. As mentioned earlier, the ancilla based techniques offers to capture the effect of arbitrary initial

correlation present in the composite system. Note that, in presence of such initial correlations the inverse FT of $\chi_\tau(u)$ may not correspond to the actual PDF of heat [76, 77]. Using the first part of Eq. 2.4 we can write $\chi_\tau(u) = \langle e^{-iuQ} \rangle$. Thus one can write $\langle Q \rangle = \langle H_f \rangle - \langle H_i \rangle$, where $H_i$ and $H_f$ are the initial and final Hamiltonian of the sub-system, and using the moment generating function as

$$
\begin{aligned}
\langle Q \rangle &= \left. \frac{d\chi_\tau(u)}{d(iu)} \right|_{u=0} \\
&= \left. \langle e^{iuH_f} H_f e^{-iuH_i} \rangle \right|_{u=0} - \left. \langle e^{iuH_f} e^{-iuH_i} H_i \rangle \right|_{u=0} \\
&= \langle H_f \rangle - \langle H_i \rangle,
\end{aligned}
\tag{2.20}
$$

where $\langle H_i \rangle = \text{Tr}[H_1 \rho_1(0)]$ and $\langle H_f \rangle = \text{Tr}[H_1 \rho_1(\tau)]$. Thus, it produces the correct definition for the first cumulant, the average heat [78] $\langle Q \rangle = \text{Tr}[H_1(\rho_1(\tau) - \rho_1(0))]$, where $\rho_1(\tau)$ being the reduced density matrix of $F_1$ at time $\tau$. In our experiment, we simulate the XY model and choose a particular uncorrelated initial state and introduce a finite amount of correlation, affecting only the off-diagonal elements of the composite density matrix as shown in Fig. 2.7(a-b), and measure $\chi_\tau(u)$ to extract the corresponding $p_\tau(Q)$. In Fig-2.7(c)-(d) we compare the probability distributions of the heat exchange between two qubits, obtained for the uncorrelated initial state, $\rho_0 = \rho_1 \otimes \rho_2$, and the corresponding correlated initial state, $\rho_0 \neq \rho_1 \otimes \rho_2$, with discord $D(1|2) = 0.68$. One thing to note here is that the initial temperature of one of the qubits exchanging heat is negative, $(\beta_1 h)^{-1} = -3359.9$ Hz and $(\beta_2 h)^{-1} = 4125.3$ Hz. It is well known that negative spin temperature is hotter than infinite spin temperature, meaning when such two systems are brought in contact thermal energy flows from the system at negative temperature to the system at infinite temperature. In the absence of any correlation this is exactly what we see experimentally (see Fig. 2.7(c)). Keep in mind our convention of positive heat, $Q$, is when it flows from $F_2$ to $F_1$. Since in this case $F_1$ is hotter than $F_2$, the heat flows from $F_1$ to $F_2$ and thus we see the net heat to be negative. But in the presence of finite correlation there is a crucial change in the statistics and thus provides evidence of reversal of heat flow (see Fig. 2.7(d)). This further implies the breakdown of the standard Jarzynski-Wójcik XFT. Similar effect for average heat flow has recently been studied experimentally for a two qubit system by measuring the qubit states following quantum state tomography [78].

# 2.6 Summary

In summary, we experimentally explore the validity of the quantum version of the transient heat XFT by implementing an interferometric approach in a three qubit liquid NMR architecture. We experimentally simulate two different heat exchange models. The experimental results show perfect agreement with the fluctuation symmetry when the composite system is weakly coupled and is prepared in the uncorrelated Gibbs thermal states with different temperatures. Interestingly, the XY-model satisfies the XFT for arbitrary coupling strength whereas for the XX-model we observe the breakdown of XFT in the strong coupling regime. Furthermore, inclusion of any finite amount of correlation in the initial state also leads to a breakdown of the fluctuation symmetry and interestingly reverses the direction of the heat flow against the temperature bias, thereby providing additional knob for controlling heat flow. We provide analytical results for these models and found excellent agreements with experiments. In the next chapter we are going to further investigate the quantum heat exchange process between two quantum systems using quantum state tomography, instead of the interferometric technique, to explore the newly obtained bound on the quantum heat fluctuations.

# CHAPTER 3

# Experimental study of Thermodynamic Uncertainty Relations

**Abstract**

A cost-precision trade-off relationship, the so-called thermodynamic uncertainty relation (TUR), has been recently discovered in stochastic thermodynamics. It bounds certain thermodynamic observables in terms of the associated entropy production. In this chapter, we experimentally study the TUR in a two-qubit system using an Nuclear Magnetic Resonance (NMR) setup. Each qubit is prepared in an equilibrium state, but at different temperatures. The qubits are then coupled, allowing energy exchange (in the form of heat). Using the quantum state tomography technique we obtain the moments of heat exchange within a certain time interval and analyze the relative uncertainty of the energy exchange process. We find that generalized versions of the TUR, which are based on the fluctuation relation, are obeyed. However, the specialized TUR, a tighter bound that is valid under specific dynamics, is violated in certain regimes of operation, in excellent agreement with analytic results. Altogether, this experiment-theory study provides a deep understanding of heat exchange in quantum systems, revealing favourable noise-dissipation regimes of operation.

## 3.1 Introduction to TURs

Obtaining universal bounds of experimentally accessible physical observables has been a fundamental topic in physics. Such bounds include the Heisenberg uncertainty relation of quantum mechanics, Carnot bound for the efficiency of heat engines and Landauer erasure principle stemming from the second law of thermodynamics. Also with the continuous progress in quantum

thermal devices like heat engines, refrigerators etc. it is high time that we try to understand the non-equilibrium systems better. The heat fluctuation relation discussed in the previous chapter is one such example. We saw that with the size of the system decreasing, the thermodynamic quantities are subjected to fluctuation. Entropy is one of these quantities, which plays a major role in better understanding non-equilibrium dynamics of the quantum systems. As a result, recently there has been an immense interest in identifying bounds on these fluctuations using entropy generated in these non-equilibrium processes. These bounds, which are trade-off relationships between the relative uncertainty of integrated currents, like heat and charge, and the associated entropy production are referred as the *Thermodynamic uncertainty relations* (TUR) [79–88, 88, 89, 89, 90, 90–98, 98–121]. If we consider a non-equilibrium process of heat exchange between two quantum systems, the integrated thermodynamic current quantity of interest is $Q$ and in that case the TUR trade-off relation reads

$$\frac{\langle Q^2 \rangle_c}{\langle Q \rangle^2} \geq \frac{2}{\langle \Sigma \rangle}, \tag{3.1}$$

where $\langle Q \rangle, \langle Q^2 \rangle_c$ are the average integrated current and its noise, respectively, and $\langle \Sigma \rangle$ is the net average entropy production in the heat exchange process, characterizing irreversibility, or how far the system is driven away from equilibrium. This bound can be thought of as a trade-off relation between the precision in measuring the heat flow, in terms of signal to noise ratio, and how fast the system can be being driven or how dissipative induced in the system, in terms of entropy production. In this thesis we refer to Eq. 3.1 as specialised-TUR or S-TUR. The S-TUR was first conjectured for continuous time, discrete state Markov process in steady state [80]. It was later proved with the large deviation technique [81, 85]. Since then, this relation has been generalized to discrete time, discrete state Markov process [86], finite time statistics [85, 88, 90, 110], Langevin dynamics [84, 87, 90, 90, 102, 105], periodically driven systems [93, 100], multidimensional system [90], molecular motors [113], biochemical oscillations [115], interacting oscillators [116], run-and-tumble process [114], measurement and feedback control [92, 117], broken time reversal symmetry systems [92, 94, 97, 104, 118], first passage times [89, 120] and quantum transport problems [98, 99, 106–108, 119]. Tighter bounds have also been reported for some stochastic currents [82]. More recently, following the fundamental nonequilibrium fluctuation relation [121], a generalized version of the TUR (G-TUR1) was derived, where the RHS of Eq. (3.1)

was modified to $\frac{\langle Q^2\rangle_c}{\langle Q\rangle^2} \geq \frac{2}{\exp\langle\Sigma\rangle-1}$, which is a looser bound compared to Eq. (3.1). In fact, a more tighter version of the generalized bound had been obtained following a slightly different approach by Timpanaro *et al.* [111] as $\frac{\langle Q^2\rangle_c}{\langle Q\rangle^2} \geq f(\langle\Sigma\rangle)$, where $f(x) = \operatorname{csch}^2(g(x/2))$ and $g(x)$ is the inverse function of $x\tanh(x)$. We refer to this bound as the G-TUR2. Interestingly, in the small dissipation limit, $\langle\Sigma\rangle \to 0$, both these generalized bounds reduce to the S-TUR of Eq. (3.1). Other weak-generalized bounds resulting from the fluctuation theorem were discussed in Ref. [112].

Even with the discovery of the G-TUR, there are compelling reasons to continue and investigate the S-TUR. (i) First and foremost, since the S-TUR is a tighter bound than the G-TUR, once satisfied it offers more definite information on performance. (ii) The S-TUR was proved for different classes of models, in particular discrete-state Markov processes. However, several quantum transport models [107, 108, 119] illustrate its validity in certain parameter regimes—albeit the underlying quantum dynamics cannot be simply-uniquely classified by its degree of Markovianity (for quantum systems, there is no agreement on the definition of non-Markovianity [122]). (iii) Notably, the S-TUR can be assessed from a fundamental nonequilibrium viewpoint, by studying its perturbative expansion, with the equilibrium value as the reference point [107, 119]. This series expansion approach does not rely on the notion of Markovianity, thus it allows a broader perspective on the validity of the S-TUR. Specifically, for the case of heat exchange between two quantum systems prepare in thermal equilibrium state at two different temperatures $\beta_1$ and $\beta_2$ in steady state the cumulants of the heat current can be expanded close to equilibrium in terms of the thermal affinity $\Delta\beta = \beta_1 - \beta_2$ around a fixed inverse temperature $\beta$,

$$
\begin{aligned}
\langle Q\rangle &= G_1\Delta\beta + G_2\frac{(\Delta\beta)^2}{2!} + G_3\frac{(\Delta\beta)^3}{3!} + \cdots \\
\langle Q^2\rangle_c &= S_0 + S_1\Delta\beta + S_2\frac{(\Delta\beta)^2}{2!} + \cdots \\
\langle Q^3\rangle_c &= R_1\Delta\beta + \cdots
\end{aligned}
\tag{3.2}
$$

Here $G_1$ is the linear transport coefficient and $S_0$ is the equilibrium noise. $G_2, G_3, \cdots$ $(S_1, S_2, \cdots)$ are higher order nonequilibrium transport (noise) coefficients. From the fluctuation relation or heat exchange process discussed in Eq. 2.3 in Ch. 2, one gets the exchange fluctuation symmetry for the characteristic function $\chi_\tau(u) = \chi_\tau(-u - i(\beta_1 - \beta_2))$. This fluctuation symmetry when used with the above mentioned equations Eq. 3.2, the following relations hold [60]: $S_0 = 2G_1$,

$S_1 = G_2$, $3S_2 - 2G_3 = R_1$, and so on. This leads to [119] ($\langle \Sigma \rangle = \Delta \beta \langle Q \rangle$),

$$\langle \Sigma \rangle \frac{\langle Q^2 \rangle_c}{\langle Q \rangle^2} = 2 + \frac{(\Delta \beta)^2}{6} \frac{R_1}{G_1} + \mathcal{O}(\Delta \beta)^3. \tag{3.3}$$

While the linear coefficient for the average heat exchange, $G_1$, is always positive, the skewness $R_1$ does not take a definite sign; when $R_1 \geq 0$, the S-TUR is valid to that order, $R_1 < 0$ indicates S-TUR violations.

## 3.2 Objective

In this chapter, we examine *experimentally and analytically* the S-TUR based on the perturbative expansion Eq. 3.3, beyond the classical, Markovian scenario. Despite intense theoretical efforts dedicated to derive and analyze the TUR, experimental studies of this trade-off relation are still limited to kinetic-network analysis of biological molecular motors [113] and charge transport in atomic-scale junctions [79]. Nevertheless, both studies concerned with problems that obey the S-TUR. We focus on the problem of quantum heat exchange between two initially thermalized qubits in a NMR setup, in the transient regime. Moments of heat exchange are obtained by performing quantum state tomography (QST) for the qubits. As expected, G-TURs are valid throughout. This agreement, while fundamentally important, does not offer any practical input for system performance or in the design of quantum heat machines. More interestingly, we identify regimes of *validity* for the S-TUR in this quantum system, and quantify its violation, thus pinpoint to favorable regimes of operation, with an excellent agreement between theory and measurements.

## 3.3 Cumulants of heat exchange

Consider two systems with their Hamiltonians $H_1$ and $H_2$ that are initially decoupled and separately prepared at their respective thermal equilibrium state. The initial composite density matrix is thus given as a product state, $\rho(0) = \rho_1 \otimes \rho_2$, with $\rho_i = \exp\left[-\beta_i H_i\right]/\mathcal{Z}_i, i = 1, 2$ the Gibbs thermal state with inverse temperature $\beta_i = 1/k_B T_i$ ($k_B$ is the Boltzmann constant) and $\mathcal{Z}_i = \text{Tr}\left[e^{-\beta_i H_i}\right]$ the corresponding equilibrium partition function. The coupling between the systems is suddenly switched on at $t = 0$ for a duration $\tau$ (total Hamiltonian $\mathcal{H}$), which allows energy exchange between the two systems. Due to the randomness of the initial thermal state and the inherent probabilistic nature of quantum mechanics, the exchanged energy is not a determin-

istic quantity, but rather quantified with a probability distribution function (PDF). In the quantum regime, this PDF is constructed by following a two-point projective measurement scheme [56, 57, 70]: The first projective measurement of the energy of the two systems is performed before they are coupled. A second projective measurement is done at the end of the energy exchange process (after the systems are separated). This procedure respects the fundamental Jarzynski and Wöjcik exchange fluctuation symmetry [52]. For the bipartite setup considered here, the joint PDF corresponding to energy change ($\Delta E_i, i = 1, 2$) between the systems, during a coupling interval $\tau$ can be written as

$$p_\tau(\Delta E_1, \Delta E_2) = \sum_{m,n} \Big( \prod_{i=1}^{2} \delta(\Delta E_i - (\epsilon_m^i - \epsilon_n^i)) \Big) p_{m|n}^\tau p_n^0. \tag{3.4}$$

Here, $p_n^0 = \prod_{i=1} 2e^{-\beta_i \epsilon_n^i}/\mathcal{Z}_i$ is the probability to find the decoupled systems in the eigenstate $|n\rangle = |n_1, n_2\rangle$ with energy eigenvalues $\epsilon_n^i$, $H_i|n_i\rangle = \epsilon_n^i|n_i\rangle$, after the first projective measurement. The second projective measurement after the evolution under the net Hamiltonian, $\mathcal{H}$ at $t = \tau$ collapses the system to the eigenstate, $|m\rangle = |m_1, m_2\rangle$, with energy eigenvalues $\epsilon_n^i$, $H_i|n_i\rangle = \epsilon_n^i|n_i\rangle$. The transition probability of the system starting in the state $|n\rangle$ after the first projective measurement and ending up in the state $|m\rangle$ after the second measurement is $p_{m|n}^\tau = |\langle m|\mathcal{U}(\tau, 0)|n\rangle|^2$, where $\mathcal{U}(t, 0) = e^{-i\mathcal{H}t/\hbar}$ is the unitary propagator with the total-composite Hamiltonian, $\mathcal{H}$. The principle of micro-reversibility of quantum dynamics for autonomous system demands, $p_{m|n}^\tau = p_{n|m}^\tau$. Following this relation and given the uncorrelated initial thermal condition of the composite system, we get the following universal symmetry for the joint PDF,

$$p_\tau(\Delta E_1, \Delta E_2) = e^{\beta_1 \Delta E_1 + \beta_2 \Delta E_2} p_\tau(-\Delta E_1, -\Delta E_2). \tag{3.5}$$

Using this relation we can write the expression for a characteristic function like quantity,

$$\begin{aligned}
\Big\langle \big(e^{-\beta_1 \Delta E_1 - \beta_2 \Delta E_2}\big)^z \Big\rangle_\tau &= \int d(\Delta E_1) d(\Delta E_2) p_\tau(\Delta E_1, \Delta E_2) e^{-z\beta_1 \Delta E_1 - z\beta_2 \Delta E_2} \\
&= \mathrm{Tr}\Big[\rho(0)^z \rho(\tau)^{1-z}\Big] \\
&= exp\Big\{(z-1)S_z\big[\rho(0)\|\rho(\tau)\big]\Big\}. \tag{3.6}
\end{aligned}$$

Till this point the analysis is exact. However it is reasonable to consider the limit $\Delta E_1 \approx \Delta E_2$ if the two systems exchanging heat are weakly coupled. Furthermore, if no energy cost is associated

with turning the interaction Hamiltonian on and off, $\Delta E_1 = -\Delta E_2$. One can then interpret the energy change in the individual systems as heat, i.e. $\Delta E_1 = -\Delta E_2 = |Q|$. In our convention, energy gained by the first system is taken as the positive heat. This changes the expression in Eq. 3.5 to $p_\tau(Q) = e^{[(\beta_1 - \beta_2)Q]} p_\tau(-Q)$, which in turn modifies Eq. 3.6 to

$$\left\langle \left( e^{-\Delta\beta Q} \right)^z \right\rangle_\tau = exp\left\{ (z-1) S_z \left[ \rho(0) || \rho(\tau) \right] \right\}. \tag{3.7}$$

Here $S_z \left[ \rho(0) || \rho(\tau) \right] = \left( 1/(z-1) \right) \ln\{ \mathrm{Tr}[\rho(0)^z \rho(\tau)^{(1-z)}] \}$ is the order-z Renyi divergence, a metric for the relation between states of a composite system at the initial ($t = 0$) and final ($t = \tau$) times. As a special case when $z = 1$, Eq. 3.7 gives us the integral form of the heat exchange fluctuation relation, $\langle e^{-\Delta\beta Q} \rangle = 1$, discussed in the previous chapter. Differentiating Eq. 3.7 $n$ times w.r.t $z$ and then using $z = 1$, one gets,

$$\langle Q^n \rangle_\tau = \frac{1}{(\Delta\beta)^n} \mathrm{Tr}[\rho(\tau) \mathcal{T}_n \left( \ln\rho(\tau) - \ln\rho(0) \right)^n]. \tag{3.8}$$

Here $n = 1, 2, \cdots$, and $\mathcal{T}_n$ is the time ordering operator which orders the operators from right to left as increasing value of time and $\Delta\beta = \beta_1 - \beta_2$. Thus we see that Eq. 3.8 provides a very powerful and unique way to obtain various moments of the heat exchange between two quantum systems by performing quantum state tomography at $t = 0$ and $t = \tau$ times. Alternatively, cumulants of the heat exchange can be obtained by implementing an ancilla-based interferometric technique [64–66, 123], as explained in the previous chapter. This method gives a direct access to the characteristic function (CF) of heat [71, 124], defined using the two-point measurement protocol (see Ch.1),

$$\begin{aligned}
\chi_\tau(u) &= \int dQ \, e^{iuQ} \, p_\tau(Q), \\
&= \mathrm{Tr}\left[ \mathcal{U}^\dagger(\tau, 0)(e^{iuH_1} \otimes 1_2) \mathcal{U}(\tau, 0)(e^{-iuH_1} \otimes 1_2) \rho(0) \right]. 
\end{aligned} \tag{3.9}$$

Here, $u$ is the variable conjugate to $Q$, and as before $\mathcal{U}(t, 0) = e^{-i\mathcal{H}t/\hbar}$ is the unitary propagator with the total Hamiltonian $\mathcal{H}$. In terms of CF, the exchange fluctuation relation translates to $\chi_\tau(u) = \chi_\tau\left( -u + i\Delta\beta \right)$ [124–127].

## 3.4  Theoretical analysis

Taking a specific case of the so-called $XY$-model, consisting of two qubits with the total Hamiltonian,

$$\mathcal{H}_{XY} = \frac{h\nu_0}{2}\sigma_1^z \otimes 1_2 + 1_1 \otimes \frac{h\nu_0}{2}\sigma_2^z + \frac{hJ}{2}\left(\sigma_1^x \otimes \sigma_2^y - \sigma_1^y \otimes \sigma_2^x\right). \tag{3.10}$$

Here, $H_1 = \frac{h\nu_0}{2}\sigma_1^z \otimes 1_2$, $H_2 = 1_1 \otimes \frac{h\nu_0}{2}\sigma_2^z$ with $\nu_0$ the frequency of the qubits, and $\sigma_i, i = x, y, z$ are the standard Pauli matrices. The last term, denoted by $H_{12}$, represents the interaction between the qubits, with $J$ the coupling parameter. An important feature of this model is that $[H_{12}, H_1 + H_2] = 0$. This commutation implies that the change of energy for one qubit is exactly compensated by the other qubit, as there is no energy cost involved in turning on or off the interaction between the qubits. For such an 'energy-preserving' Hamiltonian $\Delta E_1 = -\Delta E_2 = Q$ is exact and the fluctuation symmetry holds for any value of coupling strength. As a consequence of this the average entropy production simply reduces to $\langle \Sigma \rangle = (\beta_1 - \beta_2)\langle Q \rangle$.

Experimentally the cumulants of heat exchange are computed from the composite density matrix [128]. Alternatively, one can also obtain the exact theoretical form of the cumulants from the CF $\chi_\tau(u)$ (see Eq. 3.9), using the expression in Eq. (3.10) as the total Hamiltonian for the heat exchange, $\mathcal{H}$. Initializing the composite system in a direct product state of the individual qubits, each prepared in a Gibbs thermal equilibrium state with a particular inverse-temperature ($\beta_1$ and $\beta_2$), utilizing Eq. 3.9 and with some algebraic manipulations of the Pauli matrices, yields [123]

$$\begin{aligned}
\chi_\tau(u) &= \Big[1 + \sin^2(2\pi J\tau)\big\{f_1(\nu_0)\left(1 - f_2(\nu_0)\right)\big(e^{-ihu\nu_0} - 1\big) \\
&\quad + f_2(\nu_0)(1 - f_1(\nu_0))\big(e^{ihu\nu_0} - 1\big)\big\}\Big],
\end{aligned} \tag{3.11}$$

where $f_i(\nu_0) = (e^{\beta_i h\nu_0} + 1)^{-1}$, $i = 1, 2$. For compactness, from here onwards we identify these functions as $f_{1,2}$. It is easy to verify that the above CF satisfies the exchange fluctuation symmetry $\chi_\tau(u) = \chi_\tau(-u + i\Delta\beta)$ for arbitrary values of $J$, $\tau$, $\beta_1$, $\beta_2$, and $\nu_0$. Expressions for the average heat current and the associated noise are derived by taking successive derivatives of $\ln \chi_\tau(u)$ with respect to $iu$. We write down the first three cumulants, useful for the analysis of the TUR,

$$\langle Q \rangle_\tau = h\nu_0 \mathcal{T}_\tau(J) \Big[ f_2 - f_1 \Big],$$

$$\langle Q^2 \rangle_\tau^c = (h\nu_0)^2 \Big[ \mathcal{T}_\tau(J) \Big( f_1(1-f_2) + f_2(1-f_1) \Big) - \mathcal{T}_\tau^2(J) \left( f_2 - f_1 \right)^2 \Big],$$

$$\langle Q^3 \rangle_\tau^c = (h\nu_0)^3 \, \mathcal{T}_\tau(J)(f_1 - f_2) \Big[ 1 - 3\,\mathcal{T}_\tau(J) \big( f_1(1-f_2) + (1-f_1)f_2 \big)$$

$$+ 2\,\mathcal{T}_\tau^2(J)(f_1 - f_2)^2 \Big]. \tag{3.12}$$

Here, $\mathcal{T}_\tau(J) = \sin^2\left( 2\pi J\tau \right)$. These results are exact and the ratio $\Delta\langle Q^2 \rangle_\tau^c / \langle Q \rangle_\tau$ can be obtained using the closed-form expressions of the cumulants above. Throughout the work, these exact expressions were compared with the experimental measurements.

The expression for the ratio $\Delta\langle Q^2 \rangle_\tau^c / \langle Q \rangle_\tau$ was also obtained using a perturbative approach using Eq. 3.3 only to quadratic order of $\Delta\beta$ [129]. This was done to more conveniently obtain the regions of violation of S-TUR. We now explore these regions of violation using a two qubit liquid NMR system.

## 3.5 Experimental setup and results

To experimentally study heat exchange between two qubits we use liquid-state NMR spectroscopy of the $^{19}F$ and $^{31}P$ nuclei in the molecule Sodium fluorophosphate dissolved in $D_2O$. Experiments are performed in 500MHz Bruker NMR spectrometer at ambient temperature. As shown in Fig. 3.1(a), $^{19}$F and $^{31}$P are identified as the two qubits, 1 and 2, exchanging heat under the desired coupling Hamiltonian, Eq. 3.10. As the sample is in the liquid state, the molecules can be considered identical with intermolecular interactions averaged out due to motional averaging (see Ch.1). All the experimental procedures: initialization of the system and the heat-exchange, are completed in time scales much shorter than the relaxation time of the nuclei. The internal Hamiltonian $H_{\text{int}}$ of the two spins—in the rotating frame of the radio frequency (RF) pulses—can be written as

$$H_{\text{int}} = \frac{\pi}{2} J_{12}\sigma_1^z\sigma_2^z, \tag{3.13}$$

where $J_{12} = 868$ Hz is the scalar coupling between the $^{19}$F and $^{31}$P nuclei in the molecule Sodium fluorophosphate, whose structure is shown in fig. 3.1(a). The NMR active spin-1/2, $^{19}$P and $^{31}$P nuclei in the molecule, labelled as qubit 1 and qubit 2, respectively are coupled by Hamiltonian
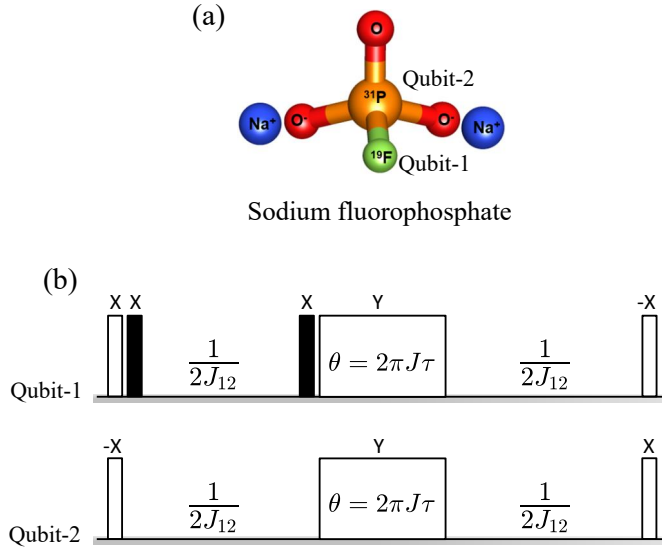
**Figure 3.1:** (a) Molecular structure of the two-qubit NMR spin system, Sodium fluorophosphate. The NMR active spin-1/2, $^{19}F$ and $^{31}P$ nuclei in the molecule, labelled as qubit-1 and qubit-2 respectively, are coupled by the Hamiltonian Eq. 3.13 with the coupling strength $J_{12} = 868\,Hz$. (b) Pulse sequence to realize heat exchange coupling Hamiltonian, $\mathcal{H}_{XY}$ in Eq. 3.10. The pulses are applied on qubits 1 and 2 in a time ordered manner from left to right. The black and white narrow solid bars represent $\pi$ and $\pi/2$ pulses, respectively, with the phases mentioned above them. $1/2J_{12}$ represents the free evolution delay under the internal Hamiltonian, $H_{int}$, given Eq. 3.13. The white box represents the $\theta$ (in rads) angle pulse about y-axis.

in eq. 3.13. The desired coupling Hamiltonian, $\mathcal{H}_{XY}$, under which the spins exchange heat is realized from the internal Hamiltonian $H_{\mathrm{int}}$ with the RF pulses displayed in fig. 3.1(b). The pulses are applied on qubits 1 and 2 in a time ordered manner from left to right. The black and white narrow solid bars represent $\pi$ and $\pi/2$ pulses, respectively, with the phases mentioned above them. $1/2J_{12}$ represents the free evolution delay during which the systems evolves under the Hamiltonian $H_{\mathrm{int}}$. The white box represents the $\theta$ (in rads) angle pulse about y-axis. The net effect of the pulse sequence is that the two spins evolve under the coupling Hamiltonian $\mathcal{H}_{XY}$ for a duration $\tau$ that is specified by the $\theta$ angle rotation about y-axis, as shown in fig. 3.1(b).

To start with, the two qubits are initialized in a psuedoequilibrium state $\rho_1 \otimes \rho_2$, where $\rho_i = \exp\left[-\beta_i H_i\right]/\mathcal{Z}_i$ is a Gibbs thermal state with inverse pseudo spin temperatures $\beta_i$ and $\mathcal{Z}_i$ the partition function. For simplicity, we set $\beta_2 = 0$ in all our measurements. Qubit 1 is prepared at a higher inverse temperature $\beta_1$ by initializing it in a pseudopure state (PPS) of $|0\rangle\langle0|$, followed by applying pulses between 0 and $\pi/2$, and a pulse field gradient (PFG). The purpose of the PFG is to destroy coherences produced by 0 to $\pi/2$ angle pulses. The qubits—prepared at two different
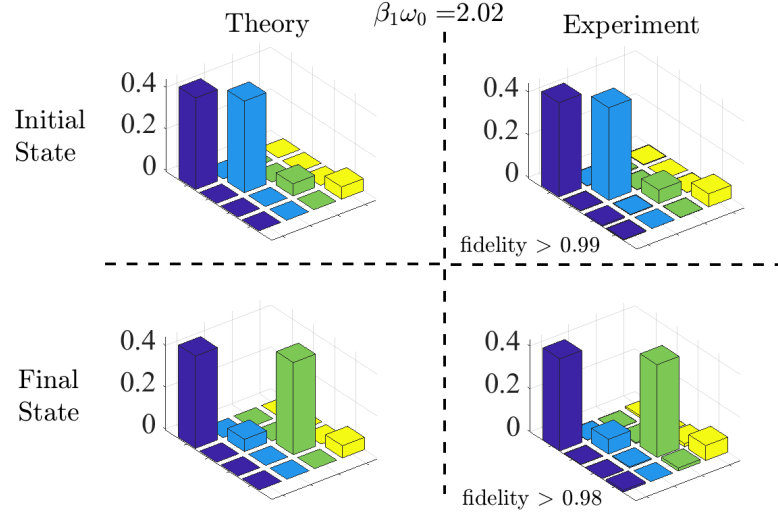
**Figure 3.2:** Quantum state tomography for the real components of the density matrix elements for both initial and final states, for the evolution parameters $J\tau = 1/4$, $\beta_2 = 0$, $\nu_0 = \pi/20$, $\beta_1\omega_0 = 2.02$

pseudoequilibrium states—are made to exchange heat under the coupling Hamiltonian $\mathcal{H}_{XY}$ for different time interval $\tau$ and different $\beta_1$. Following the coupling period, we perform QST of the final state (in addition to the QST of the initial pseudoequilibrium state). Fig. 3.2 provides both the theoretical and experimental quantum state tomography results for a particular realization. Only the real components of the initial and final density matrix of the composite system is shown as the imaginary part is vanishingly small. The two qubit tomography sequence consists of six independent experiments and measurements and the states were realized with the fidelity of more than 98. From Eq. 3.8 achieve the cumulants of heat exchange.

In Figs. 3.3 and 3.4 we present two cases, displaying agreement and violation, respectively, of the S-TUR. First, in Fig. 3.3 we set $J\tau = 1/8$. According to the theoretical analysis, the S-TUR is valid (to the lowest perturabtive order) when the skewness is positive, or $\mathcal{T}_\tau(J) = 1/2 < 2/3$ (obtained by perturbative approach [129]). Indeed, we find in Fig. 3.3(a) that both $R_1(\tau)$ (see Eq. 3.3) and $\Delta\beta\frac{\langle Q^2\rangle_\tau^c}{\langle Q\rangle_\tau} - 2$ are positive for all $\Delta\beta$. In Fig. 3.3(b), we compare the different bounds on the relative uncertainty $\frac{\langle Q^2\rangle_\tau^c}{\langle Q\rangle_\tau^2}$, experimentally as well as theoretically, and show that the S-TUR provides the tightest bound. Next, Fig. 3.4(a) shows the results for $J\tau = 1/4$, for which according to the perturbative analysis [129], violations of the S-TUR are expected to occur already in the quadratic order of $\Delta\beta$, as $\mathcal{T}_\tau(J) = 1 > 2/3$ . Indeed, clearly one can see a violation for $0 < \beta_1\omega_0 < 3.2$. Furthermore, the third cumulant, $\langle Q^3\rangle_c$, is negative in this region,

which indicate the region of violation using Eq. 3.2 and 3.3. The theoretically predicted lowest value for the S-TUR for this model is $\Delta\beta\frac{\langle Q^2\rangle^c_\tau}{\langle Q\rangle_\tau} \approx 1.86$, and we experimentally reach a value very close to this number. The violation of the S-TUR can also be seen in Fig. 3.4(b): The S-TUR bound ($2/\langle\Sigma\rangle$) appears *above* the ratio $\frac{\langle Q^2\rangle^c_\tau}{\langle Q\rangle^2_\tau}$, and it is greater than the other, looser bounds. Measurements again closely match the theoretical curves.

A complete analysis of the TUR as a function of the heat exchange duration $\tau$ and for a fixed $J = 1$ Hz, is presented in Fig. 3.5. We display the first three cumulants and note that the relative uncertainty is reduced (violation of S-TUR) within a certain region of parameters: The minimum value of the S-TUR precisely appears when the fluctuation of the heat exchange are reduced, below the value of the first cumulant. As expected, the skewness is found to be negative in this region.
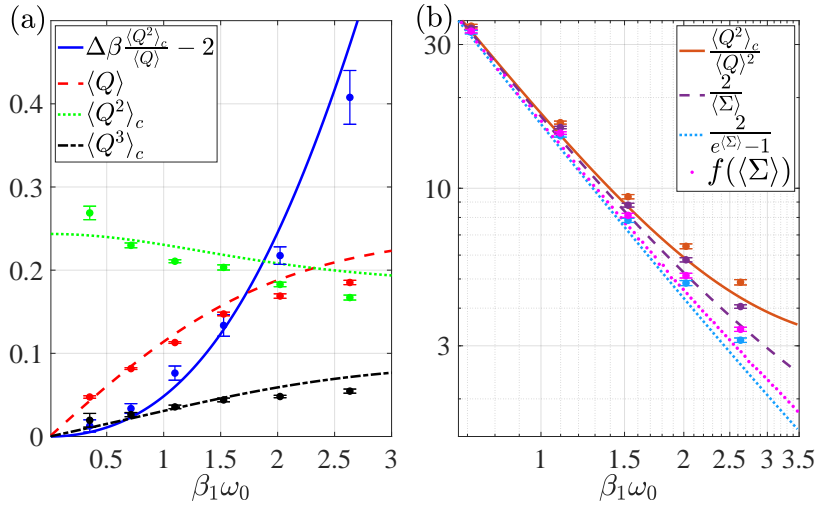


**Figure 3.3:** (a) First three cumulants of heat exchange, along with a measure for the S-TUR, as a function of the inverse temperature of qubit 1 $\beta_1$; $\beta_2 = 0$. Measurements (symbols) are constructed with the help of Eq. 3.8, and are compared to the theory (lines), Eq. 3.12. (b) Comparison between different bounds, showing that the S-TUR provides the tightest lower bound to $\frac{\langle Q^2\rangle^c_\tau}{\langle Q\rangle^2_\tau}$. Experimental results are obtained from state tomography, yielding $\langle Q\rangle_\tau$, which is used to calculate the entropy production. Theoretical results are based on Eq. 3.12. Parameters are $J\tau = 1/8$ and $\nu_0 = \pi/20$ ($\omega_0 = 2\pi\nu_0$).

## 3.6 Summary

We experimentally examined the TUR for heat exchange by realizing the XY-model, performing quantum state tomography and extracting the heat exchange cumulants. We found that the S-
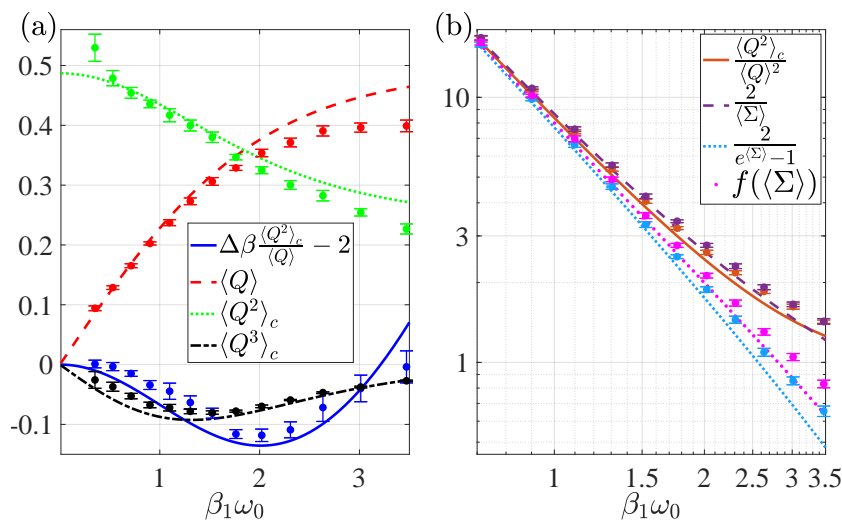
**Figure 3.4:** Same as Fig. 3.3 but at $J\tau = 1/4$ leading to $\mathcal{T}_\tau(J) > 2/3$, therefore the violation of the S-TUR.

TUR provides a tight bound up to a certain threshold value for the qubit-qubit coupling parameter $\sin^2(2\pi J\tau)$, beyond which the bound is invalidated. As predicted theoretically, the validity of the S-TUR crucially depends on the sign of the third cumulant. Generalized versions of the TUR are satisfied throughout in our system, as expected, since these (weak) bounds are derived from the universal fluctuation relations, which is satisfied in our experimental setup. Nevertheless, a most interesting observation is that the tighter S-bound is in fact also satisfied over a wide range of the coupling value $J\tau$. The S-TUR thus contains practical information: The condition to invalidate it pinpoints to regimes of favourable performance for heat machines, operating with high constancy *and* little dissipation.
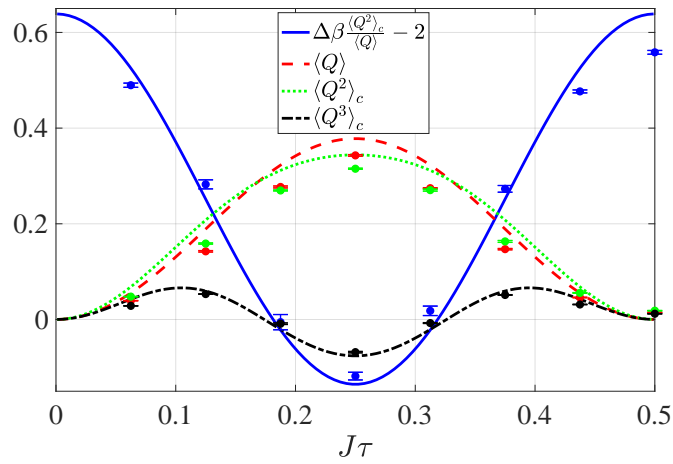
**Figure 3.5:** Cumulants of heat exchange and the S-TUR as a function of $J\tau$ for $J = 1$ Hz, $\beta_1\omega_0 = 2.02$ and $\beta_2 = 0$. Other parameters are the same as in Fig. (3.3).

# CHAPTER 4

# Experimental localisation of quantum entanglement through monitored classical mediator

### Abstract

Quantum entanglement is a form of correlation between quantum particles that cannot be increased via local operations and classical communication. It has therefore been proposed that an increment of quantum entanglement between probes that are interacting solely via a mediator implies non-classicality of the mediator. Indeed, under certain assumptions regarding the initial state, entanglement gain between the probes indicates quantum coherence in the mediator. Going beyond such assumptions, there exist other initial states which produce entanglement between the probes via only local interactions with a classical mediator. In this process the initial entanglement between any probe and the rest of the system "flows through" the classical mediator and gets localised between the probes. In this chapter we utilise liquid-state NMR spectroscopy, to demonstrate the optimal growth of quantum correlations between two nuclear spin qubits interacting through a mediator qubit in a classical state. In other words, we demonstrate maximal entanglement gain between two quantum probes via a classical mediator. We additionally monitor, i.e., dephase, the mediator in order to emphasise its classical character. Results indicate the necessity of verifying features of the initial state if entanglement gain between the probes is used as a figure of merit for witnessing non-classical mediator. Such methods were proposed to have exemplary applications in quantum optomechanics, quantum biology and quantum gravity.

### Reported in

**Soham Pal**, Priya Batra, Tanjung Krisnanda, Tomasz Paterek, and T. S. Mahesh, *Experimental localisation of quantum entanglement through monitored classical mediator,* Quantum 5, 478 (2021).

# 4.1 Introduction

Quantum entanglement is widely recognised as a resource "as real as energy" [130]. Yet, limits on establishing entanglement between remote particles were systematically studied only recently and with surprising results. Protocols in which the distant particles get entangled by exchanging ancillary particles can establish remote entanglement without ever communicating it, i.e., no entanglement with the ancillaries [131–135]. It is now understood that entanglement gain in these schemes is not bounded by the communicated entanglement, but rather by communicated quantum discord [136–141], a form of quantum correlation that persists in many disentangled states [142–144].

In another route to producing remote entanglement, the exchange of quantum particles is replaced by continuous interactions of distant systems (probes) with a third object, a mediator. In this scenario the theory predicts that not only the probes can get entangled without ever entangling the mediator [131], but also that they can even get entangled in the absence of any quantum discord between the probes and the mediator [145]. This lack of discord is a strong notion of classicality which means that the mediator can be measured at any time without disturbing the whole multipartite system. It is the same notion as "classical communication" in the framework of local operations and classical communication at the core of entanglement theory [136, 137, 146], but generalised to continuous in time interactions. In practical terms, the probes get entangled even if the mediator is continuously monitored or dephased.

It is an observation of this effect, for a discrete number of measurements on the mediator, that is reported here corroborating with the theoretical characterisation of maximal amount of entanglement that can be established in this way [147]. Moreover, in our experiments the monitoring measurement is the same at all times, which reinforces classicality of the mediator being at all times in one of two distinguishable states (correlated to the probes). Additionally to observing exotic effect of multipartite entanglement our results have practical implications. The scenario where two objects are coupled via a mediator is common in science. For example, entanglement gain between the probes has been proposed as a witness of quantum mediator in various scenarios [148], such as in condensed matter [149], optomechanics [145], quantum gravity [145, 150, 151] or quantum biology [152]. Present results emphasise that these methods must verify features of the initial state in order to validate their implications, i.e., non-classicality of the mediating

system.

## 4.2 Classicality and Non-classicality

This section gives a brief explanation about what is meant by classical and non-classical objects in this chapter, with respect to a particular measurement. The definition of classicality or non-classicality of the system in question is based on the type of quantum correlation, quantum discord, it shares with another system. Quantum discord is a type of quantum correlation **error**, which is more general than entanglement i.e., all entangled states have quantum discord, but not the other way around. Discord in bipartite system is measurement dependent and a bipartite state, $\rho_{ab}$, is said to have non-zero discord, with measurements on '$b$', if the net state, $\rho_{ab}$ can not be written in a form,

$$\rho = \sum_i p_i \rho_a \otimes |b_i\rangle\langle b_i|. \tag{4.1}$$

Where $\{|b_i\rangle\}$ form an orthonormal basis. Such a state is often referred as a 'Quantum-Classical' state, as it can be seen easily that there exists a set of projective measurements $\{\prod_i^b\}$, where $\prod_i^b = |b_i\rangle\langle b_i|$, on the sub-system '$b$' such that, $\sum_i \prod_i^b \rho \prod_i^b = \rho$. The measurement on the sub-system '$b$' leaves the over-all system unchanged. In such a case, subsystem '$b$' is said to be in a classical state. Thus if discord of a bipartite system, with measurement on sub-system '$b$', is zero, one can say the system is in a Quantum-Classical state and sub-system '$b$' is in a classical state. Please note that this is not symmetric as, performing the same measurements on sub-system '$a$' does not guarantee invariance of the net system state. It is important to understand here that classicality is not just the property of the subsystem, but rather a property of the net system as a whole. If a single system is in question, one can always find a measurement basis which leaves it unchanged, and thus a single system is always in classical state in some reference basis. When this basis of measurement changes with time, it can be safely argued that the system generates quantum coherences. To conclude, classicality or non-classicality of a sub-system is related to it's ability to share quantum correlations with the other sub-system. If the sub-system shares zero quantum correlation (zero discord) with the other sub-system, it can be safely remarked that the it is in a 'classical' state.
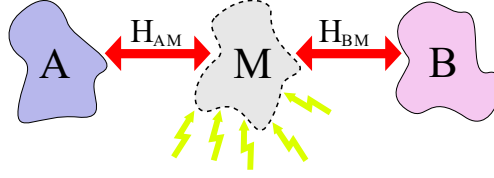
## 4.3 Theoretical example



**Figure 4.1:** Schematic for the tripartite system. Probes $A$ and $B$ are coupled to the mediator $M$ by a coupling Hamiltonian in Eq. 4.3. The mediator $M$ is measured in a specific basis, ($\sigma_x$ basis), during as well as at the end of the evolution.

The simplest example of the discussed phenomenon involves three qubits (spin-$\frac{1}{2}$ systems) in the following initial state [145]:

$$\rho_0 = \frac{1}{2}|\psi_+\rangle\langle\psi_+| \otimes |+\rangle\langle+| + \frac{1}{2}|\phi_+\rangle\langle\phi_+| \otimes |-\rangle\langle-|, \tag{4.2}$$

where the first two qubits are the probes $A$ and $B$, and the third qubit is the mediator $M$. Kets $|\pm\rangle$ denote the eigenstates of $\sigma_x^M$ Pauli matrix, whereas $|\psi^+\rangle = \frac{1}{\sqrt{2}}(|01\rangle + |10\rangle)$ and $|\phi^+\rangle = \frac{1}{\sqrt{2}}(|00\rangle + |11\rangle)$ are the two Bell states. Since one could dephase the mediator in the $\sigma_x^M$ basis without perturbing the total state, the mediator is said to be in a classical form. Note also that initially the probes are not entangled as their state is an even mixture of two Bell states [153]. This system evolves under Hamiltonian ($\hbar = 1$ throughout):

$$\mathcal{H} = \omega(\sigma_x^A + \sigma_x^B) \otimes \sigma_x^M, \tag{4.3}$$

where each probe individually interacts with the mediator via a coupling constant $\omega$, but not directly with each other. It is easy to see that the state of the mediator is stationary and hence it remains classical at all times. Furthermore, at all times, it is one and the same measurement i.e., dephasing along $\sigma_x^M$ basis, that keeps the total state invariant. As discussed in the previous section, this invariance of the total state under repeated measurement of the mediator, implies that $M$ stays in a classical state. Yet entanglement between the probes increases and they become even maximally entangled [145].

At first sight this example might be surprising as it seems that entanglement between the probes is increased by local interactions with a classical mediator, in contradiction to the very

definition of entanglement [154]. We stress that there is no contradiction as already in the initial state each individual probe is entangled with the rest of the system. One can show that the corresponding entanglement, as quantified by negativity [155], is given by $E_{A:BM} = E_{B:AM} = 1/2$, which is the amount of entanglement in maximally entangled state of two qubits. The subsequent evolution localises this entanglement to the probes. It is the essence of our demonstration that this localisation can be done via the classical mediator even if it is measured or dephased.

## 4.4 Optimality

In [147] we show how the relative entropy of entanglement in a tripartite system, with a classical mediator, is bounded by the mutual information between the mediator and rest of the system, $\mathcal{E}_{A:BM} - \mathcal{E}_{A:B} \leq I_{AB:M}$. We further use this bound to show that for a tripartite system the maximum entangled that can be localised, through a classical mediator, between the rest of the subsystem is bounded as follows:

$$\mathcal{E}_{A:B}(t) - \mathcal{E}_{A:B}(0) \leq I_{AB:M}(0), \tag{4.4}$$

where $\mathcal{E}_{A:B}$ denotes the relative entropy of entanglement [156] and $I_{AB:M}$ is the mutual information [7]. We emphasise that the entanglement gain between the probes is <u>not</u> bounded by entanglement or discord with the mediator, but rather the total correlation, including classical [157, 158], with the mediator is the relevant figure of merit. The theoretical example presented above realises the upper bound in Eq. 4.4. It is straightforward to verify that the mediator is initially correlated with $I_{AB:M}(0) = 1$ and maximally entangled state has relative entropy of entanglement $\mathcal{E}_{A:B}(t) = 1$. Therefore, the implemented protocol localises as much entanglement as possible.

## 4.5 Experimental setup

We use liquid-state NMR spectroscopy of $^{13}$C, $^1$H and $^{19}$F in dibromofluoromethane dissolved in acetone with linear topology, H - C - F (see Fig. 4.2(a)). Nuclei of hydrogen and fluorine are identified as probes $A$ and $B$, respectively, whereas carbon nucleus is naturally the mediator $M$. Experiments were performed in 500 MHz Bruker NMR spectrometer at room temperature. The sample consists of identical and fairly isolated dibromofluoromethane molecules and all the dynamics of the three-qubit system is completed before any significant environmental in-
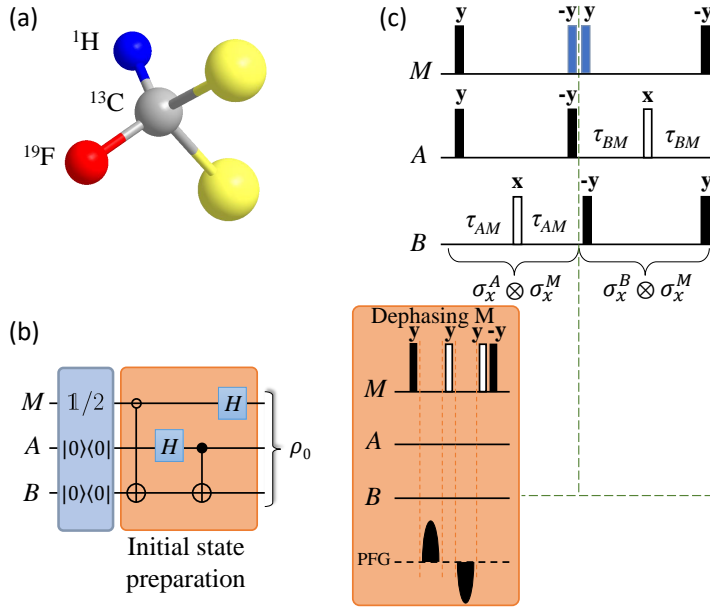
**Figure 4.2:** (a) Molecular structure of dibromofluoromethane. We identify $^1$H and $^{19}$F nuclei as probe qubits and $^{13}$C as the mediator qubit. (b) Preparing the initial state as in Eq. 4.2 using CNOT and Hadamard gates as shown. (c) Pulse sequences used to evolve the system under the coupling Hamiltonian of Eq. 4.3. The solid and empty bars represent $\pi/2$ and $\pi$ pulses with phases shown above them. The blue pulses cancel each other for the no-dephasing case. Dephasing of $M$ is realized by introducing pulses shown in the orange box in the positions marked by the dashed lines. Here PFG represents pulsed-field gradient along $\pm z$ axis. The delays $\tau_{AM} = 1/(4J_{AM})$ and $\tau_{BM} = 1/(4J_{BM})$.

fluences [40, 72, 159]. The longitudinal and transverse relaxation time constants are longer than 2 s and 0.2 s, respectively. The internal Hamiltonian of the three spin system in a frame rotating about the Zeeman field with individual Larmor frequencies reads:

$$
H_0 = \frac{\pi}{2} \Big( J_{AM}\, \sigma_z^A \otimes \sigma_z^M + J_{BM}\, \sigma_z^B \otimes \sigma_z^M +
$$
$$
J_{AB}\, \sigma_z^A \otimes \sigma_z^B \Big), \tag{4.5}
$$

with $J_{AM} = 224.5$ Hz , $J_{BM} = -310.9$ Hz, and $J_{AB} = 49.7$ Hz being the corresponding coupling constants between the nuclei. The qubits in the molecular system have internal dynamics that directly couples the probes $A$ and $B$. The effects of this coupling must be canceled if we are to claim generation of entanglement between the probes via classical mediator only. Thus, during experiments, to evolve the system under the interaction Hamiltonian $\mathcal{H}$ in Eq. 4.3 we switch off the internal interaction between spins $A$ and $B$ by applying suitable refocusing pulses as will be explained later.

In general, the quantum state of our three-qubit NMR system is of the form $(1 - \epsilon)\frac{1}{8}\mathbb{1} + \epsilon\,\rho$, where $\frac{1}{8}\mathbb{1}$ describes the background population, $\rho$ is the so-called deviation density matrix and $\epsilon$ is the purity factor, which is in the order of $10^{-5}$. Nevertheless the NMR experiments are sensitive to the deviation density matrix and from now on whenever we refer to the "state" of the system we mean the pseudopure state characterized by the deviation density matrix. Starting from a three qubit thermal equilibrium state of longitudinal magnetization at room temperature, we prepare the state corresponding to $|00\rangle\langle00| \otimes \mathbb{1}/2$, written in the order $ABM$, using a similar pulse sequence as given in [160, 161]. The initial state $\rho_0$, Eq. 4.2, is then obtained by the succession of gates given in Fig. 4.2(b). All gates are implemented using radio frequency pulses resonant with the nuclei. The open CNOT gate is realised with the help of Krotov optimisation technique [162] with fidelity exceeding 0.99 using push-pull optimization of quantum controls [162]. The fidelity of the produced initial state to the ideal one is more than $97\%$.

Fig. 4.2(c) shows the pulses used to realize the interaction Hamiltonian, $\mathcal{H}$ in Eq. 4.3. In our experiments we have set the strength of the coupling constant $\omega = 1$ rad/s. The solid bars and empty bars represent $\pi/2$ and $\pi$ pulses, respectively. The first half of the pulse sequence evolves the system under the coupling between $M$ and $A$. Since we have $\sigma_z \otimes \sigma_z$ coupling in our system to start with (see Eq. 4.5), the $(\pi/2)_y$ pulses transform the $z$-basis to $x$-basis which then evolves under $\sigma_z \otimes \sigma_z$ coupling. Since the Hamiltonian in Eq. 4.3 is a sum of two commuting terms, we first evolve the entire system under $\sigma_x^A \otimes \sigma_x^M$ followed by the evolution under $\sigma_x^B \otimes \sigma_x^M$ for the same amount of time, i.e, the physical time rescaled by the coupling strengths $J_{AM}$ and $J_{BM}$. As all the three qubits are coupled to each other, we decouple $B$ during the first half of the evolution by refocusing it using a $\pi$ pulse, as shown in Fig. 4.2(c). The net effect is that the system only evolves under $AM$ coupling, whereas $B$ remains unaltered. The same is repeated in the second half of the evolution with $A$ being refocused and the system evolving under $BM$ coupling. We repeat the experiment with the same initial conditions and different duration of dynamics in order to illustrate how entanglement accumulates between the probes. The probes in principle gain maximal entanglement at $\omega t = \pi/8$. Finally, we obtain the deviation density matrices via full state tomography using eleven detection experiments [163].

To make the claim that the mediator $M$ is classical even stronger, we introduce another set of experiments in which we dephase (measure) the mediator qubit in between and at the end of the

evolution. The pulse sequence implementing the dephasing of $M$ is depicted in the orange box of Fig. 4.2(c). In contrast to the previous set of experiments, just after the realization of $\sigma_x^A \otimes \sigma_x^M$ the mediator qubit $M$ is dephased in $x$-basis. The selective dephasing of the mediator is achieved by a pair of opposite pulsed-field-gradients (PFGs) separated by a $\pi$-pulse on the mediator. The PFGs cancel each other for the probes $A$ and $B$, whereas they add-up for $M$. A $\pi$-pulse on $M$ is applied to undo the spin-flip caused by the previous $\pi$-pulse. Finally, measurement along $x$-basis is realized by simply rotating the basis using $(\pi/2)_y$ and $(\pi/2)_{-y}$ pulses as shown.
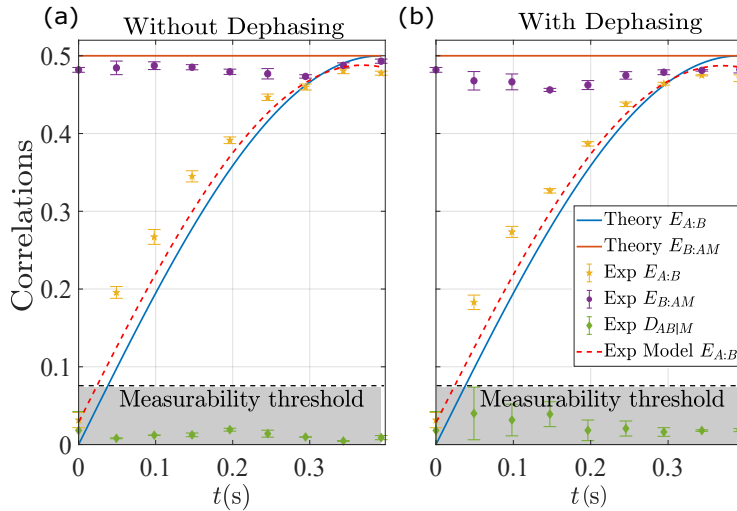
## 4.6 Results and discussion



**Figure 4.3:** Summary of experimental findings. Solid lines show noiseless theoretical predictions: blue for $E_{A:B}$ and red for $E_{B:AM}$. The corresponding experimental data is marked with yellow bars and purple bars, respectively. Green bars show measured discord $D_{AB|M}$, all within experimentally established region of vanishing discord (grey, see main text). Dashed red lines present $E_{A:B}$ within a model considering the RF inhomogeneity errors in the experiments. (a) without dephasing and (b) with dephasing the mediator qubit.

From the experimentally measured three-qubit deviation density matrices we compute various quantum correlations such as discord between the two probes and mediator, $D_{AB|M}$, quantum entanglement between the probes, as measured by the negativity $E_{A:B}$, as well as the negativity $E_{B:AM}$. The quantum discord is calculated following the definition of Ollivier and Zurek [143]. Recall that discord is not a symmetric quantity and our $D_{AB|M}$ denotes discord as measured on the mediator. It should also be stressed that due to small admixture of the deviation density matrix,

the ensemble averaged NMR signals mask genuine entanglement [164]. From this perspective one can think of our experiment as NMR simulation of entanglement localization via classical mediator.

The measured discord and entanglement are presented in Fig. 4.3 for datasets without and with dephasing the mediator. The gray-shaded region represents measurability threshold of discord owing to experimental errors. This threshold is obtained from measurements of discord for experimental thermal equilibrium state. Ideally this state has vanishing discord but experimental imperfections in state tomography give rise to residual values. The amount of discord $D_{AB|M}$ calculated for evolved deviation density matrices (green data points) all lie well within this experimental precision limit of discord. We thus conclude that the mediator was classical at all times during the evolution. At the same time quantum entanglement between the probes $E_{A:B}$ consistently grows. While experimentally established entanglement does not exactly match noiseless prediction based on Hamiltonian in Eq. 4.3, given by the blue solid line, the dashed red line follows experimental findings more closely. This line is a prediction of a model that takes into account inhomogeneity of the radio frequency pulses in the NMR spectrometer used to realize the evolution under the Hamiltonian in Eq. 4.3. It is interesting to note that the entanglement between each probe with rest of the system, $E_{B:AM}$ or $E_{A:BM}$, remains invariant throughout the evolution. We demonstrated that an increment of quantum entanglement between two probes coupled via a mediator in general does not signify a non-classical mediator.

We note that the process demonstrated here is different from, e.g., entangling two spins via dipole-dipole interaction. The Hamiltonian of the latter directly couples magnetic moments of the two particles and hence it is not surprising that entanglement grows. In contradistinction, we study tripartite system with an explicit mediator. Even if the dipole-dipole interaction is rewritten in the form where the mediator is clearly distinguished, our theory shows that one has to begin with entanglement $E_{A:BM}$ or $E_{B:AM}$ in order to localise it.

Perhaps the most interesting application for revealing non-classicality of mediators is witnessing quantum gravity through entanglement between nearby masses [145, 150, 151]. Estimations with concrete experimental arrangements show that in order to observe gravitational entanglement the masses need to be cooled down near the ground state of their traps [150, 165–167]. In such a case the masses are close to a pure state and hence they are initially almost uncorrelated

from the rest of the world. This can be quantitatively measured by the sum of their von Neumann entropies and in principle leaves a small room for the initial $E_{A:BM}$ or $E_{B:AM}$ entanglement. If the final gravitational (relative entropy of) entanglement between the masses exceeds this initial sum, the produced entanglement cannot be the result of the localisation of the initial entanglement, analogously to the phenomenon demonstrated in the present work, and hence quantum discord with the field is witnessed during the process [145].

# CHAPTER 5

## Discrete Time Crystalline behaviour in NMR spin systems

**Abstract**

Study of out-of-equilibrium driven quantum systems led to the introduction of Time crystals as a new phase of matter. Since its conception in 2012 by the Frank Wilczek, tremendous amount of work, both theoretically and experimentally, has been done towards understanding this exotic behaviour. We experimentally study the response of star-shaped clusters of initially unentangled nuclear spin-$\frac{1}{2}$ moments in solid and liquid NMR samples to an inexact $\pi$-pulse sequence, and show that an Ising coupling between the centre and the satellite spins in the liquids and long-range dipolar coupling in solids, result in robust period-two magnetization oscillations. The period is stable against bath-effects but the amplitude decays with a time scale that depends on the inexactness of the pulse. Simulations reveal a semiclassical picture where the rigidity of the period is due to a randomizing effect of the Larmor precession under the magnetization of surrounding spins. The time scales with stable periodicity increase with net initial magnetization even in the presence of perturbations, indicating a robust temporal ordered phase for large systems with finite magnetization per spin. In the case of solids we further observe the robustness of the Discrete Time Crystalline (DTC) behaviour under gradual removal of the dipolar interactions by selective decoupling of the spins and by Magic Angle Spinning (MAS).

**Partially reported in**

**Soham Pal**, Naveen Nishad, T S Mahesh, and G J Sreejith , *Temporal Order in Periodically Driven Spins in Star-Shaped Clusters,* Phys. Rev. Lett. 120, 180602 (2018).

## 5.1   Introduction

Spontaneous symmetry-breaking is a central notion in many body physics, allowing us to explain several natural phenomena such as formation of a magnet or ice crystals. While there are many

systems in which the underlying spatial symmetries are broken resulting in various crystalline phases, and a few classical systems that exhibit spontaneous temporal oscillations, it was only recently that the possibility of spontaneous breaking of time translation symmetry in quantum systems was considered. The initial proposals [168] for realizing a spontaneous breaking of continuous time translation symmetry were later shown to be forbidden in static equilibrium systems [169, 170]. However, in the attempt to understand quantum thermodynamics of driven systems, it was realized that an externally driven, disordered, interacting spin system can stabilize a phase which spontaneously breaks the discrete time translation ($\mathbb{Z}$) symmetry of the system to a subgroup $\mathbb{Z}_n$ [171–174]. These driven, interacting and disordered systems have a sharp notion of phase i.e., when driven by Hamiltonian with a period of $T$, $\mathrm{H}(t) = \mathrm{H}(t + T)$, these systems break the underlying symmetry of the Hamiltonian and oscillate with a period which is an integral multiple of the $T$. The phenomenon was soon experimentally realized in trapped cold-atom systems that mimic a long range interacting disordered spin-half chain [175], and in dense collections of randomly interacting nitrogen vacancy spin impurities embedded in diamond [176, 177]. While this work was under review, similar observations were also realized in other solid NMR experiments[178].

In this work, we report on the observation of robust period two oscillations of magnetization in a cluster of nuclear spins in a star-shaped geometry in liquid samples and highly disordered solid state NMR spin system cluster. For the case of liquids we use three different spin clusters, with varying number of satellite spins. The central spin interacts with $N = 3$, 9 and 36 surrounding satellite spins via Ising interactions mediated by the electron cloud in the molecule. The satellite spins do not interact with each other. Where as in the case of solids we use a highly disordered spin cluster sample with a huge range of dipolar couplings (inter as well as intra-molecular). These spins are subjected to simultaneous $\pi$ flips and delays by a Hamiltonian of period $T$. Spins in each molecule show magnetization oscillations of period-two, half the frequency of the underlying Hamiltonian, breaking the symmetry of the Hamiltonian, when subjected to a sequence of the above mentioned transverse $\pi$-pulses (pulses that rotate every up/down spin by $\pi$ radians). However the interactions within the cluster result in the period rigidly locking on to this half frequency, even under a sequence of inexact $\pi$ pulses (pulses that rotate by an amount $\pi - e$). Simulations of an isolated cluster show that the period is robust even in the presence of small
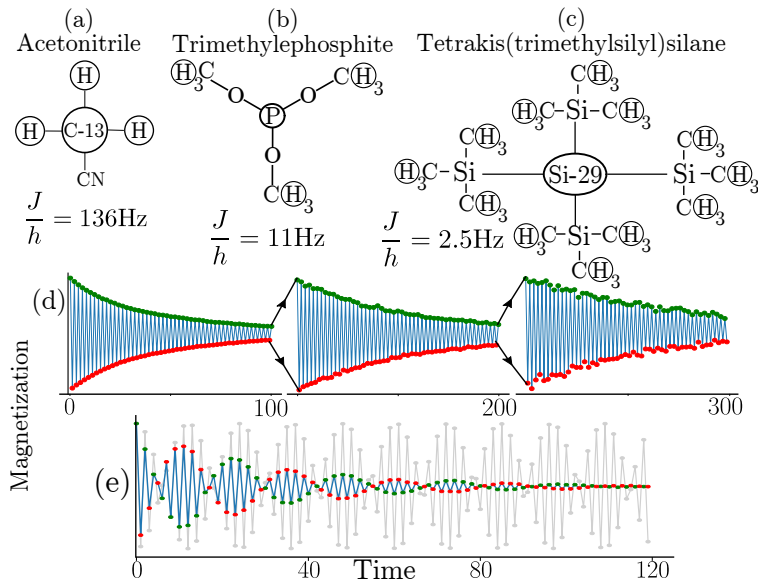
**Figure 5.1:** Molecules used in the experiments - acetonitrile (a), trimethyl phosphite (TMP) (b) and tetrakis(trimethylsilyl)silane (c) with the 4, 10 and 37 NMR active nuclei encircled. (d) Experimentally measured magnetization $\langle S_i^z \rangle$ of satellite spins of TMP for the pulse sequence in Eq. 5.1 with $JT/\hbar = 6.5$ and $\theta = \pi - 0.1$. Red/green dots show the magnetization at odd/even time steps. For visibility in the plot, the $y$ axis has been rescaled at every $100^{\text{th}}$ time step. (e) Blue line shows experimentally measured magnetization oscillations of free/non-interacting spins of protons in acetonitrile which contain a spinless $C - 12$ central spin, at a pulse angle $\theta = \pi - 0.27$. Gray lines indicate the expected response in the absence of a bath.

perturbations and disorder that break the symmetries of the model. In what follows we describe the liquid and solid state systems, the experiments performed and the results in details.

## 5.2 DTC behaviour in liquids

For the present work we perform nuclear magnetic resonance (NMR) experiments on acetonitrile, trimethyl phosphite (TMP) and tetrakis(trimethylsilyl) silane (TTSS) containing $4, 10$ and $37$ spins [Fig 5.1 (a-c)] [179]. The experiments are performed on ensembles of $\sim 10^{15}$ molecules with a distribution of initial states, described by a direct product density matrix. High precision ensemble average magnetization measurements of central/satellite spins can be performed using free-induction decay signals. Period-two oscillation of individual spins result in corresponding oscillations of the ensemble average magnetization. Control experiments performed on molecules that contain a spinless isotope at the center show oscillations with frequencies that linearly vary with the deviation $e$, showing that the robustness of the period originates from interaction with

the central spin. In the following, unless units are made explicit, frequencies are in units where the time period $T = 1$.

## 5.2.1  Model and numerical results

The unitary operator evolving the state of the cluster between successive steps is given by

$$U\left(J,\theta;t\right) = \exp\left[-\frac{\imath Jt}{\hbar}S_0^z\textstyle\sum_{i=1}^{N-1}S_i^z\right] \text{ for } t \in [0,T)$$

$$U\left(J,\theta;T\right) = \exp\left[-\imath\theta\textstyle\sum_{i=1}^{N-1}S_i^x\right]\exp\left[-\frac{\imath JT}{\hbar}S_0^z\textstyle\sum_{i=1}^{N-1}S_i^z\right] \tag{5.1}$$

where $J$, $T$ and $\theta$ are the Ising interaction strength, time period and the rotation angle characterizing the pulse. $S_i^\mu$ are spin operators. Site index $i = 0$ labels the central spin (See Ref [40],and Ch. 1 for a description of liquid-state NMR which realizes the unitary)

We will label the deviation from $\pi$ pulse by $e = \pi - \theta$. To simplify the discussion below, it is useful to temporarily switch to a toggling frame of reference in which the basis of every spin rotates by an angle $\pi$ about the $x$-axis after each pulse. On account of the $\mathbb{Z}_2$ symmetry of the model, the unitary operator in the rotating basis retains the same form as in Eq. 5.1 but with a reduced pulse angle $e = \pi - \theta$, *i.e.,* the spins in the rotating basis see a unitary operator $U(J, -e; t)$. A constant $z$-magnetization of all spins in the rotating basis picture corresponds to a period-two oscillation of all physical spins. Numerical simulations indeed show that a finite magnetization is maintained under a sequence of weak pulses (pulse angle $-e$). Presented below is a semiclassical picture inferred from numerical simulations (Fig 5.2).

For simplicity, we will consider the time evolution starting from a fully polarized initial state under a sequence of small pulses $\theta = -e$ (corresponding to $\theta = \pi - e$ experienced by the physical spins). During $0 < t < T$, the spins do not evolve as the state is an eigenstate of the unitary evolution (Eq. 5.1). At time $t = T$, the pulse rotates every spin by an angle $e$ away from $z$-axis as shown on the Bloch sphere (see Fig-5.2). During $T < t < 2T$, the central spin which is tilted away from the $z$-axis evolves under the Hamiltonian $H \approx -J\left\langle M_\mathrm{s}\right\rangle S_0^z$ where $M_\mathrm{s}$ is the net $z$ magnetization of the satellite spins resulting in a Larmor-like precession as shown in Fig-5.2(d). The orientation of the central spin at $t = 2T^-$ depends on the amount of precession $\frac{JT\langle M_\mathrm{s}\rangle}{\hbar}$. The $e$ pulse at $t = 2T$ now brings the spin vector to a polar angle $0 < \theta < 2e$. Owing to the precession, the successive $e$ pulses can now cancel each other. In contrast, in a set of non-interacting spins
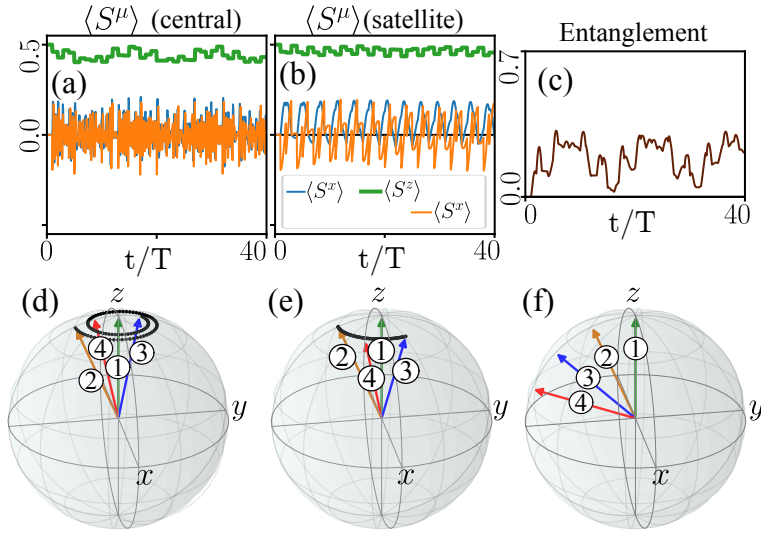
**Figure 5.2:** Numerical simulations of spins in the rotating basis. (a-b) Time dependence of the expectation values of the three spin components of a satellite (a) and central (b) spin for a system with $N = 8$ spins, $\frac{JT}{\hbar} = 4$ and pulse angle $\theta = e = 0.4$. Initial state is the fully $z$-polarized state. (c) Entanglement entropy of the central spin. (d) Bloch sphere representing the spin components of a central spin (of a 6 spin cluster) at times $t = 0, T^+, 2T^-$ and $2T^+$; $+/-$ labels the time just after/before the pulse. Sequence of intermediate dots track the evolution between time $t = T$ and $2T$. (e) Same as (d) but for a satellite spin. (f) Bloch vectors for a single isolated spin at successive time steps.

the angles always add constructively leading to a steady increase in the polar angle ($ne$ after $n$ pulses - Fig-5.2(f)). Thus the randomizing effect of the interaction induced Larmor precession, causes the polarization of the central spin to survive longer than that of an isolated spin. We expect the same effect to be seen also on the surrounding spins except that they precess under the magnetization of the central spin alone resulting in a slower precession of the satellite spins compared to the central spin (Fig-5.2(f)). Constant sign of the Bloch-vector component $\langle S^z \rangle$ in the rotating basis implies a period two oscillation of the physical spin orientation (Fig-5.2(a,b)).

Such a semiclassical picture assumes that the central spin is not maximally entangled with the surrounding spins, as otherwise the Bloch vector may vanish in length even when the polar angle is conserved. As shown in Fig-5.2(c), the von Neumann entropy of the central spin stays below maximum ensuring finite Bloch vectors. Simulations of the small systems at much longer time scales using exact diagonalization indicate that entanglement of the system does not rise for time scales that increase exponentially with system size (Fig-5.3(c,d)).

In the following, we will use the physical spin basis and to explore the stability of the period to perturbations other than $e$, we numerically simulated a pure spin system with a time independent
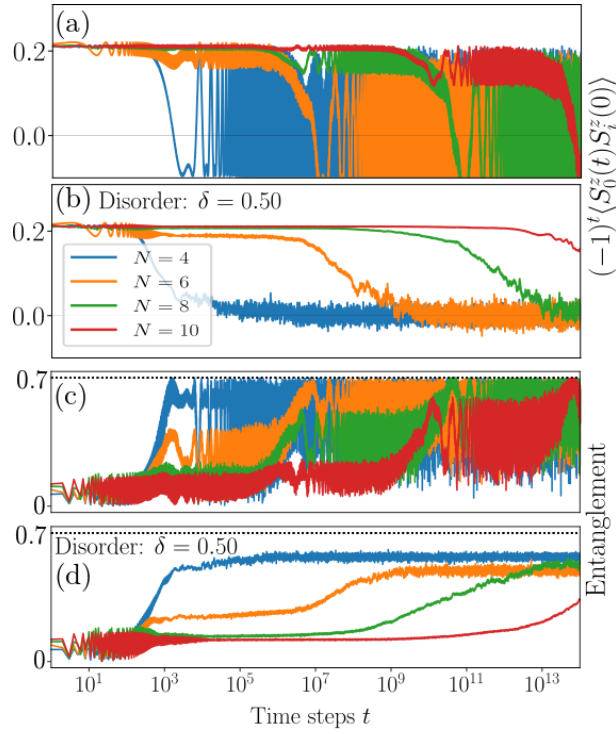
**Figure 5.3:** (a,b) Time dependence of cross correlation (multiplied by $(-1)^t$) between the central spin $S_0^z$ and a satellite spin $S_i^z$ from simulations of systems of different sizes ($JT/\hbar = 4, e = 0.05, \psi = R_x(\pi/8)\,|\uparrow\uparrow\ldots\rangle$, $R_x(\pi/8)$ being the rotation of all spins by $\pi/8$ about $x$). Disorder strengths are 0 (a,c) and 0.5 (b,d). (c,d): Entanglement entropy of the central spin. Disorder averaging has been performed in (b,d).

perturbation to the Hamiltonian of the form $\sum_i h_i^x S_i^x + h_i^z S_i^z$. The quenched disorder $h_i^x$ and $h_i^z$ were picked uniformly from $[-\delta/2, \delta/2]$ and $[0, \delta]$ (in units where $T/\hbar = 1$). To compare the response of different system sizes, we fix the average magnetization per spin. We found that in all cases, the time scale in which there was a dominant period-two oscillation appeared to grow exponentially with system size (Fig-5.3). Similar increase in time scales were also observed in simulations with disorder free perturbations of the form $h_z \sum S_i^z$ and $J_x \sum S_i^x S_{i+1}^x$. The time scales with stable period are higher when the initial state of the spin cluster had a larger total magnetization. Slow heating and stability in this disorder free system is likely to be associated with a prethermal regime similar to that in Ref [[180],[181]]. However, unlike the high frequency case discussed there, the experiments here are performed at low frequencies ($JT > 1$). Cross correlation between the central and satellite spins (Fig-5.3(a,b)) show that different spins oscillate in synchrony suggesting that the robustness of the period is a collective behaviour of all spins.

For small $e$ and the $\mathbb{Z}_2$ symmetric unitary (Eq-5.1), origin of the period-two oscillations at finite deviation $e$ can be understood in a manner similar to that described in Ref [172]. The Floquet unitary describing the periodic drive commutes with the parity operator $P = \prod 2S_i^x$ and therefore the quasienergy eigenstates have a parity quantum number $\pm 1$. The quasienergy states of the system at $\theta = 0$ occur in degenerate quasienergy pairs of opposite parity $\psi_\pm = |\sigma_0, m\rangle \pm |-\sigma_0, -m\rangle$, where $|\sigma_0, m\rangle$ is a state with central and satellite spins in an eigenstate of $S_0^z$ and $\sum_{i=1}^{N-1} S_i^z$ with eigenvalues $\sigma_0$ and $m$. At small finite pulse angle $\theta = e$, the quasienergy-degeneracy is broken in a manner that depends on the magnetization $|m|$ as $\sim e^{2|m|+1}$. In the presence of a sequence of inexact $\pi$ pulses $\theta = \pi - e$, the unitary is $U(J, \pi - e; T) = P U(J, -e; T)$ for which the states $\psi_\pm$ have quasienergies separated by $\pi + \mathcal{O}(e^{2|m|+1})$. A polarized direct product initial state $|\sigma_0, m\rangle$ is a symmetric or antisymmetric linear combination of the states $\psi_\pm$. As a result, the unitary for inexact $\pi$ pulses acts on such a polarized state to flip the orientation of all the spins at each time step:

$$U |\sigma_0, m\rangle = U(\psi_+ \pm \psi_-) \sim \psi_+ \pm e^{-i\pi} \psi_- = |-\sigma_0, -m\rangle$$

resulting in a period-two magnetization oscillation. Better degeneracies of the higher magnetization initial states explains why initial states with larger magnetization shows stable periodicity for longer time scales. Subleading ocillations of other frequencies originate from mixing of $\psi_\pm$ with

states of smaller magnetizations.

## 5.2.2 NMR setup

The spin systems used for the experiments - Acetonitrile, TMP and TTSS are prepared in the solvents dimethyl sulfoxide/deuterated chloroform. The experiments are carried out at 300 K in a Bruker 400 MHz NMR-spectrometer equipped with an UltraShield superconducting magnet of strength 9.39 T. The unitary of Eq-5.1 is realized in a doubly rotating frame [40]. The $\theta$ pulses are realized by simultaneous resonant, short duration radio-frequency pulses on all spins. The pulse duration can be tuned to control $\theta$. Interaction parameter $JT/\hbar$ can be set by tuning the time period $T$. After $n$ pulses, any residual transverse magnetization is destroyed using a pulsed-field-gradient (PFG) and the final magnetization $\langle S^z \rangle$ is rotated into the transverse direction with the help of a $\pi/2$ detection pulse. The NMR signal is then detected as the oscillatory emf induced in a probe coil due to the precessing transverse magnetization about the Zeeman field [38]. During each period, the measurement was performed immediately after the pulse.

Initial states in the experimental ensemble of $\sim 10^{15}$ molecules can be described by mixed state of the form $\rho = \prod_{i=0}^{N-1} \otimes \rho_i$, where $\rho_i = \frac{1}{2}(\mathbb{I} + \epsilon \sigma_i^z)$, and the purity $\epsilon \approx 10^{-5}$, $\sigma^z$ being the Pauli matrix. The purity is inferred from the thermal equilibrium distribution at the magnetic field strength inside the spectrometer. Note that while the ensemble average magnetization is small, the ensemble contains sub-ensembles of all possible initial magnetizations $-N/2 \leq M \leq N/2$, with a marginally higher fraction (parameterized by $\epsilon$) with positive sign. Clusters with finite magnetization $|M|$ show stable periodic-two oscillations which collectively reflect in the ensemble average measurements.

## 5.2.3 Results and Discussion

Fig-5.4 shows the measured satellite spin magnetizations in TMP and acetonitrile for an interaction parameter $\frac{JT}{\hbar} = 20.7$ ($J/h = 11$ Hz, $T = 0.3$ s). Magnetization oscillations on TMP (Fig-5.4 (a,b,c)) show a clear peak at frequency half (subharmonic peak), whose height decreases with increase in the deviation $e$, vanishing at $e \approx 0.4\pi$ in agreement with the simulations. There are no discernible peaks in the spectrum at frequencies $\frac{\pi \pm e}{2\pi}$ expected from non-interacting spins. Fourier transforms were taken using standard FFT algorithms applied to the data from the chosen time
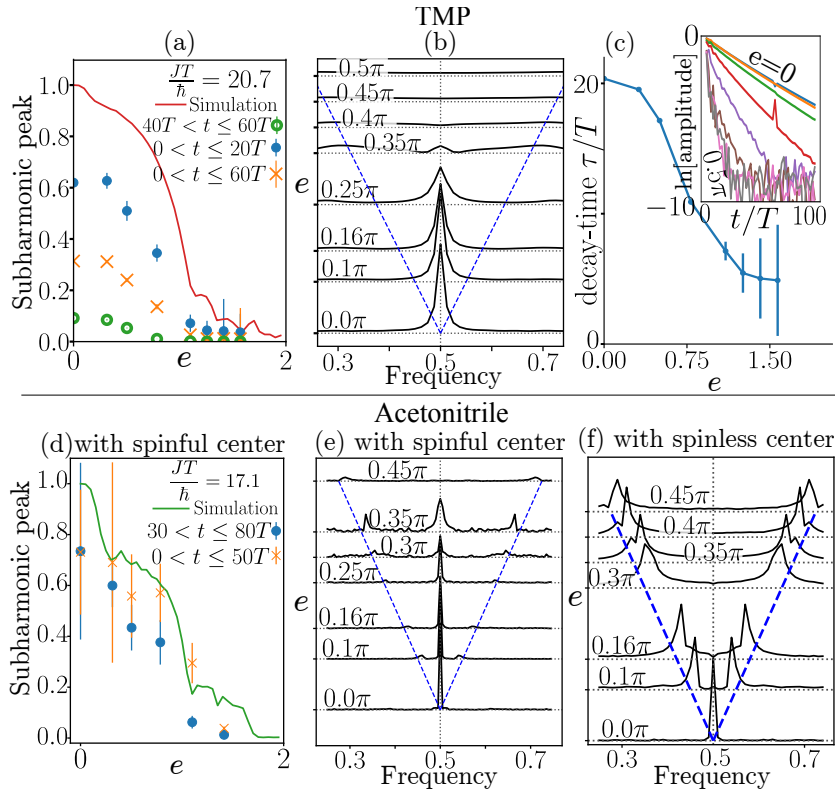
**Figure 5.4:** Experimentally measured satellite spin magnetization $\sum_{i=1}^{N-1} \langle S_i^z \rangle$. (a,d): Magnitude of the subharmonic peak upon varying $e$ in TMP and Acetonitrile. Solid continuous lines show results from simulations. Different markers indicate Fourier transforms of experimental measurements in different time windows. (b): Waterfall plot of the Fourier spectrum (time-window $0 < t < 80T$) of the experimentally observerd magnetization of TMP at different deviations $e$. Dashed blue lines indicate the location of peaks expected for a free spin. (c): Variation of the decay time of the experimentally observerd magnetization amplitude with $e$ for TMP. (e,f): Same as (b) but for acetonitrile with a spinfull C-13 (e) and spinless C-12 (f) atom at the center.

window. For comparability, magnetization data was normalized such that initial magnetization was 1.

The RF pulses have $\pm 5\%$ distribution of $\theta$ values around the nominal value, due to the spatial inhomogeneity of the RF field over the volume of the sample. The experimental system suffers from decoherence due to coupling to an external thermal bath. This could explain the decay of the oscillation amplitudes with time [182]. Apart from this decay, the magnitude of the subharmonic peaks in each time window match the simulations. Interestingly the decay time decreases steadily with $e$ (Fig 5.4 (c)).

Acetonitrile sample contains a mixture with $99\%$ of the molecules carrying a spinless C-12 and $1\%$ of the molecules containing spinful C-13 atom in the methyl group. Although NMR signal
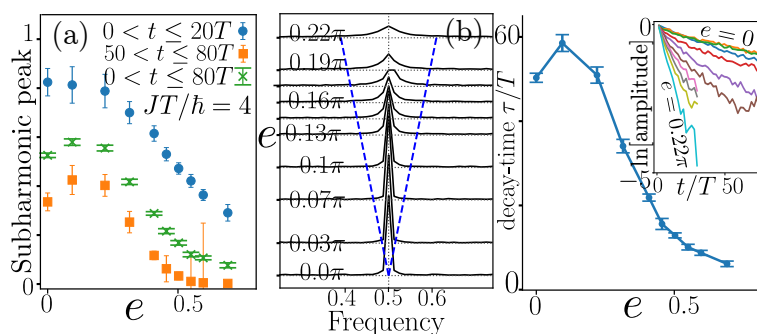
**Figure 5.5:** Experimental values of central spin magnetization $\langle S_0^z \rangle$ in TTSS. (a): Subharmonic peak strength as a function of the deviation $e$. Different markers indicate Fourier transforms in different time windows. (b): Waterfall plot of the Fourier spectrum of the experimentally observed central spin magnetization at different $e$. Blue dashed line shows the location of the Fourier peaks expected for free spins. (c): Decay time scale as a function of $e$. Inset shows a semi log plot of the amplitude of magnetization as a function of time.

has contributions from the satellite spins of both isomers, their contributions can be separated in the frequency domain of the induced emf oscillations during the final measurement process thanks to the presence or absence of interaction with the central spin, and thus they can be analysed separately. Experiments on acetonitrile were performed at the parameter $\frac{JT}{\hbar} \approx 17.1$ ($J/h = 136$Hz, $T = .02$s). Figure 5.4(e) shows the Fourier transforms of magnetization of the satellite spins in acetonitrile that contain a spinfull C-13 central atom. Figure 5.4(f) shows the Fourier transform of the magnetization of the satellite spins in molecules containing a spinless C-12 central atom. In the absence of a central spin with which the satellites can interact, they oscillate like isolated spins with a frequency that varies linearly with $e$. Absence of stable period in this non interacting system clearly shows that the stability of period observed in other clusters arise from interactions. Fig-5.5 shows the results for magnetization measurements of the central Si-29 spin of the TTSS molecule which has $N = 36$ satellite spins around the central atom. Experiments were performed at $JT/\hbar \approx 4$ ($J/h = 2.5$Hz, $T = 0.25$s).

## 5.3 DTC behaviour in Solids

For this, we choose the molecule Di-tert-butyl-phosphine oxide in powdered solid state with interacting spins in the molecules. The predominant interaction (inter as well as intra-molecular) in this amorphous solid sample is dipole-dipole interaction. The molecules in the sample contain two species of spin-1/2 nuclei, $^{13}$C and $^{1}$H, of our interest. The topology of the molecule is such
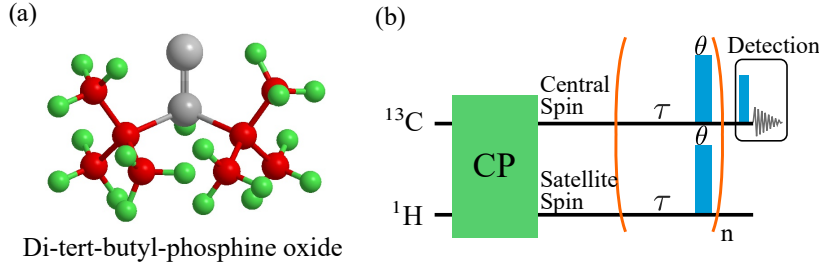
**Figure 5.6:** Molecular structure- Di-tert-butyl-phosphine oxide (a). The pulse sequence for observing DTC behaviour is shown in (b). The green box (CP) indicates the cross-polarization technique used transfer polarization from $^1$H to $^{13}$C nuclei.

that $^{13}$C nuclei are surrounded by $^1$H nuclei. Due to the restricted motion of the molecules in solids unlike liquids, the dipolar interactions don't average out [38, 40]. As a result the central and satellite spins interact with spins of other molecules in the sample as well (inter-molecular dipolar interaction). The form of the dipolar interaction Hamiltonian between $i^{th}$ and $j^{th}$ spin, under secular approximation [40], for homonuclear and heteronuclear case can be written as,

$$\mathcal{H}_{ij}^{dip} = d_{ij}\left(3S_i^z S_j^z - \hat{\mathbf{S}}_i.\hat{\mathbf{S}}_j\right)$$
$$\mathcal{H}_{ij}^{dip} = \bar{d}_{ij} 2S_i^z S_j^z, \tag{5.2}$$

respectively, where $d_{ij} = \bar{d}_{ij}\frac{1}{2}(3\cos^2\Theta_{ij} - 1)$ is the secular dipolar coupling and $\bar{d}_{ij} = \frac{\mu_0}{4\pi}\frac{\gamma_i\gamma_j\hbar}{r_{ij}^3}$ is the dipole coupling constant [40]. The $\gamma_i$ and $\gamma_j$ are the gyromagnetic ratios of the two spins and $\mu_0 = 4\pi \times 10^{-7}$Hm$^{-1}$ is the magnetic constant. $r_{ij}$ and $\Theta_{ij}$ are the distance between the two spins and the angle between the vector joining the two spins and the static magnetic field, B$_0$ (see Fig. 5.10). The total dipolar Hamiltonian can then be written as

$$\mathcal{H}^{dip} = \sum_{i>j}\mathcal{H}_{ij}^{dip}. \tag{5.3}$$

Solid state NMR provides a 3D spin network with plethora of disorder and interactions between the spins. Thus, it's a natural test bed for observing DTC behaviour. In what follows we drive the $^{13}$C and $^1$H nuclear spins in this 3D spin network under a periodic Hamiltonian, consisting of evolution under interactions (Eq. 5.3) for a duration of $\tau$ followed by a $\theta = \pi - \epsilon$ angle pulse on nuclei about *x*-axis. Here $\epsilon$ is the error introduced in radians. The pulse sequence for the

same is is shown in Fig. 5.6(b). The unitary operator for such an evolution is shown below.

$$U\left(D_{ij}, \theta; t\right) = \exp\left[-it\mathcal{H}^{dip}\right] \text{ for } t \in [0, \tau)$$

$$U\left(D_{ij}, \theta; \tau\right) = \exp\left[-i\theta\sum_i S_i^x\right] \exp\left[-it\mathcal{H}^{dip}\right] \qquad (5.4)$$

It will be seen that the system breaks the symmetry of the underlying Hamiltonian and oscillates with half its frequency. We test the robustness of such a DTC order by varying the time of free evolution, $\tau$. To see the explicit dependence of DTC order on interaction we further remove the effect of strong interaction in the system by decoupling the $^1$H nuclear spins. As mentioned previously, dipolar interactions are orientation dependent. For a particular orientation of the spins with the magnetic field, dipolar interaction completely vanish. This orientation angle is preferably known as the 'Magic angle' in NMR literature [39, 183]. As will be seen, we use this procedure to study the DTC order by spinning the sample at different spinning rates along this orientation to gradually get rid of interactions in the system.

### 5.3.1 Experimental Results

In this section we present the experimental results of the above mentioned periodically driven system. We observe the dynamics of $^{13}$C $z$-magnetization in the highly disordered 3D-spin cluster subjected to a periodic drivings of form shown in Eq. 5.4. Starting from an initial thermal state, owing to the low natural abundance of $^{13}$C, we first transfer polarization from $^1$H to $^{13}$C employing a Cross-Polarization (CP) pulse sequence, which uses a Hartmann-Hann kind of matching for polarization transfer [39, 184]. After the transfer, starting from a $z$-polarized $^1$H and $^{13}$C state, we repeatedly evolve the system under the unitary given in Eq. 5.4, consisting of free evolution under the coupling Hamiltonian, followed by $\theta$ angle pulse about $x$-axis on both $^{13}$C and $^1$H nuclei for different values of $\tau$, with a fixed value of $\theta = \pi - \epsilon$, with $\epsilon = 0.2\pi$.

#### 5.3.1.1 Experiments without spinning

Figure. 5.7 shows the experimental results for the oscillations of normalized $z$-mag ($M_z = \sum_{i_C}\langle S_{i_C}^z\rangle$) of $^{13}$C under the periodic driving (Eq. 5.4) for different values of evolution time, $\tau$ ($y$-axis), and its corresponding Fourier transform. The blue line corresponds to $\theta = \pi$ pulses, where as the red line corresponds to $\theta = \pi - \epsilon$ pulse being applied on $^{13}$C and $^1$H spins. For
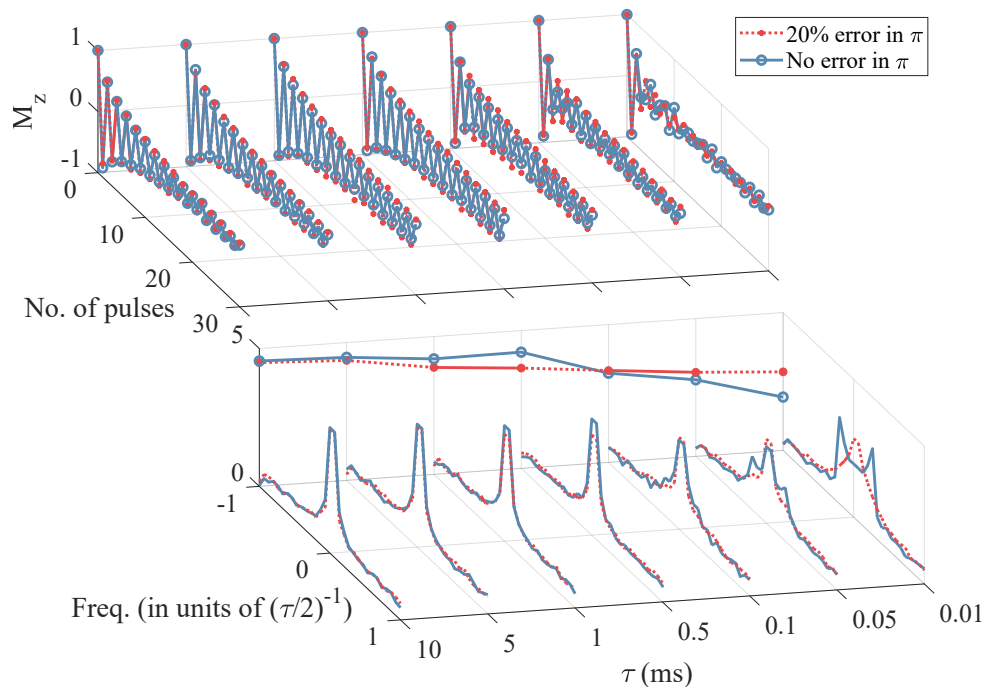
**Figure 5.7:** Experimentally measured $z$-magnetization, $M_z = \sum_{i_C} \langle S^z_{i_C} \rangle$, and its Fourier transform for $^{13}$C nuclear spins in di-tert-butyl-phosphine oxide for the pulse sequence in Eq. 5.4 for different values of evolution time, $\tau$. The number of pulses and $\tau$ are presented in the $x$-axis is and the $y$-axis respectively. The blue and red lines correspond to $\theta = \pi$ and $\theta = \pi - 0.2\pi$ pulses respectively. The corresponding height of the Fourier transform peaks have been plotted in the $yz$-plane.
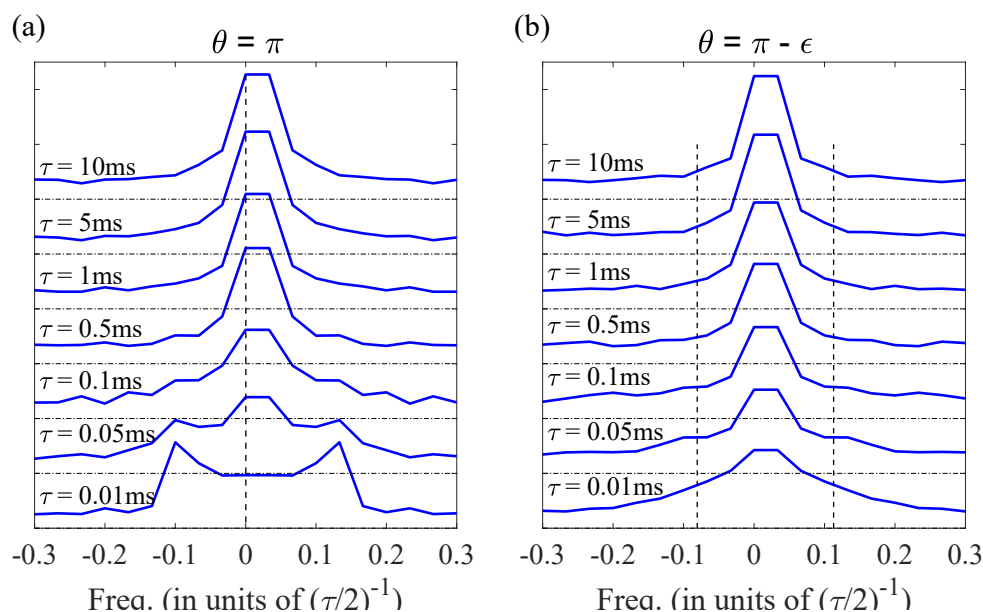
**Figure 5.8:** Waterfall plot for Fourier transform of the $z$-magnetization oscillation of $^{13}$C, with $\theta = \pi$ (a) and with $\theta = \pi - 0.2\pi$. The black dashed line represent the theoretical position of the peaks in the absence of interactions in both cases.

the intermediate values of $\tau$ it can be seen that the oscillations of both the blue (without error) and red (with 20% error) lines are quite indistinguishable. Where as for lower values of $\tau$, time crystalline behaviour is hardly observed. But as we increase the interaction time, $\tau$, we observe emergence of DTC order. Also, we observe that there is an optimal value of $\tau$ for which DTC is prominent, $\tau = 1ms$ being the best in our case. For clarity, peak height of the Fourier transform have been plotted in the $yz$-plane.

Fig. 5.8(a) and (b) shows the waterfall plot for the Fourier transform of the signal for $\theta = \pi$ and $\theta = \pi - 0.2\pi$, respectively. It is clearly seen that the peak height increases with the increase in $\tau$ and there are no prominent peaks at $\pm\epsilon/2\pi$ for these values of $\tau$, expected for non-interacting spins. The black dashed lines Fig. 5.8 represent the position of such peaks in the case of non-interacting spins. One point to note here is that, even though the red line corresponds to no error in the pulse, it still decays away like the one with error, the blue line. This can be explained by the fact that for solid state pulse sequences the hard $\pi$ pulses are far from perfect due to the effect of chemical shift anisotropy and homonuclear dipolar coupling in the solid sample.

To make the fact clear that the DTC signature is coming into the picture due to the interactions present in the sample, we perform a control experiment in which we selectively decouple
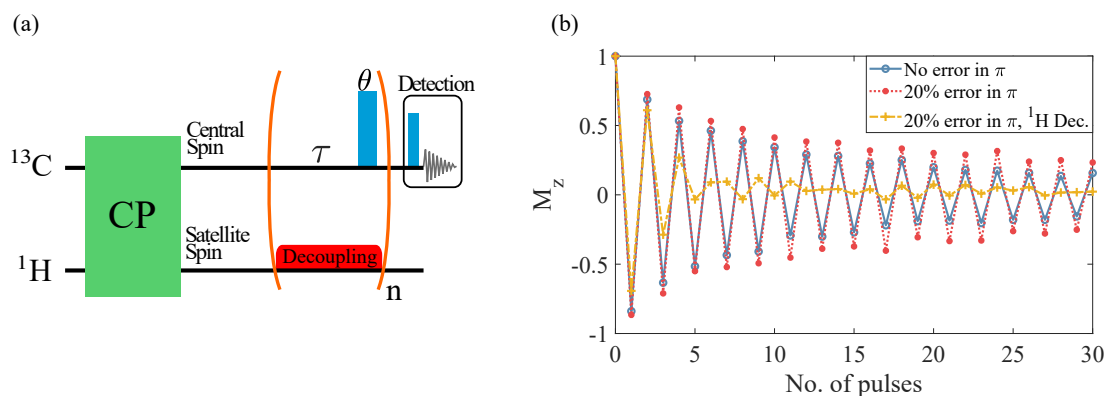
**Figure 5.9:** (a) The pulse sequence for experiment with $^1$H decoupling. (b) Experimental data of $z$-Magnetization oscillations for: $\theta = \pi$ (blue) without $^1$H decoupling, $\theta = \pi - 0.2\pi$ without decoupling $^1$H nuclei (red) and with $^1$H decoupled (yellow).

the $^1$H nuclei by combination of pulses on them and then observe the $z$-magnetization of $^{13}$C. Figure.5.9(a) and (b), respectively, show the pulse sequence and corresponding experimental signal. Both dotted red line and broken yellow lines have 20% error in them but the later is with $^1$H nuclei (partially) decouple. One can see the stark contrast in the period two oscillations of the blue and green line. This clearly indicates that interaction is a key ingredient for robust period two oscillation (DTC).

### 5.3.1.2 Experiments with spinning

In this set of experiments we avoid decoupling $^1$H, as done in the previous case. Instead we use Magic Angle Spinning (MAS) to get rid of the strong dipolar interactions. From Eq. 5.2 it is evident that the dipolar interaction strength depends upon the orientation of the sample w.r.t the static magnetic field, B$_0$. It can be shown that for $\Theta = 54.74°$ the secular dipolar interaction term, $d_{ij}$, vanishes. Thus, we spin the solid sample rapidly about an axis oriented at $54.74°$ (Magic Angle) w.r.t the static magnetic field in the spectrometer (see Fig. 5.10), at varying spinning rate to gradually remove the dipolar interaction in the system as we drive the system under the pulse sequence shown in Fig. 5.6(b). Spinning the solid sample fast enough removes the anisotropic dipolar interactions and further orientation of the sample to 'Magic angle' gets rid of remaining the dipolar coupling in the system.

Figure 5.11 shows the $^{13}$C $z$-magnetization oscillation for $\theta = \pi$ (blue line) and $\theta = \pi - 0.2\pi$
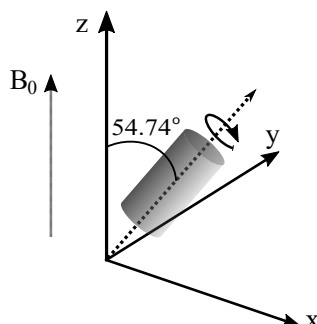
**Figure 5.10:** Schematic diagram for Magic Angle Spinning (MAS). $B_0$ is the static magnetic field applied along $z$-axis. The shaded cylinder is the capsule containing the sample. It is oriented at the indicated angle and rotated at varying spinning rates.
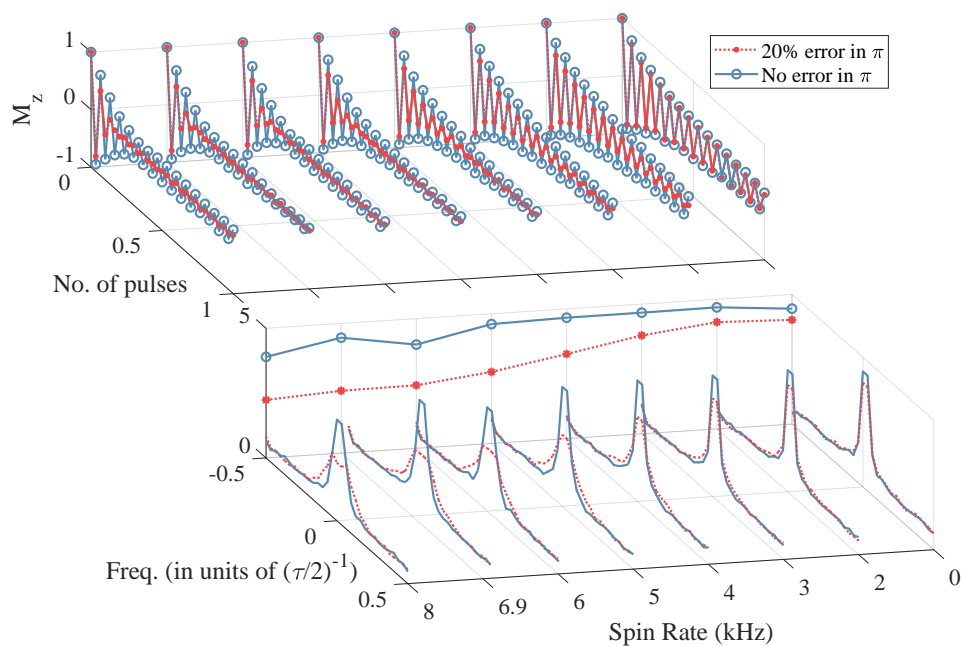


**Figure 5.11:** Experimentally measured $z$-magnetization, $M_z = \sum_{i_C} \langle S_{i_C}^z \rangle$, and its Fourier transform for $^{13}$C nuclear spins in di-tert-butyl-phosphine oxide for the pulse sequence in Eq. 5.4 for different 'Magic Angle Spinning' rate with $\tau = 1$ms. The number of pulses and spinning rate are presented in the $x$-axis and the $y$-axis respectively. The blue and red lines correspond to $\theta = \pi$ and $\theta = \pi - 0.2\pi$ pulses respectively. The corresponding height of the Fourier transform peaks have been plotted in the $yz$-plane.
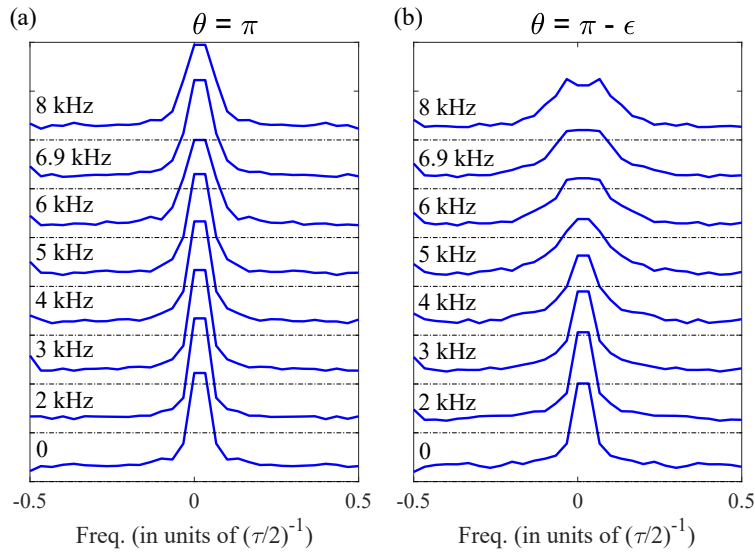
**Figure 5.12:** Waterfall plot for Fourier transform of the $z$-magnetization oscillation of $^{13}$C, with $\theta = \pi$ (a) and with $\theta = \pi - 0.2\pi$ for different MAS rates, with delay $\tau = 1$ms.

(red line) pulses on both $^1$H and $^{13}$C nuclei, with delay $\tau = 1$ms (see Eq. 5.4), for different magic angle spinning rate. The $x$ and $y$ axis are no. of pulses and spinning rates respectively. The $z$-axis is normalized $z$-magnetization. As the spinning rate increases it is clearly seen in Fig. 5.11 that the period two $z$-magnetization oscillations progressively vanishes for the case of driving with $20\%$ error in the $\pi$ pulse (dotted red line), as compared to the $\theta = \pi$ (blue line). Furthermore, as the dipolar interaction vanishes with the increase in spinning rate, the $z$-magnetization oscillates like that of isolated spins and one can observe the appearance of sub-harmonic peaks in the Fourier transform plots. Appearance of such sub-harmonic peaks in this spinning case clearly shows that the instability of period observed in the clusters arise from the absence of interactions.

## 5.4 Summary

We have experimentally demonstrated that stable temporal order can be realized in liquid and solid state NMR spin-clusters. In the liquid case, absence of a stable period in the control experiment in C-12 acetonitrile shows that stability of the period requires interactions between the spins (as in C-13 acetonitrile). Though bath effects and other perturbations in the experiment lead to a magnetization decay with time, interestingly the period appears to be unaffected. Stability of the period in the spin cluster improves with increase in total initial magnetization. Therefore large

systems with finite initial magnetization per spin, should show a stable temporal ordered phase, as can be seen in the solid case. The stability of the oscillations in such systems can be interpreted as an error-correction on the pulse sequence and may find potential applications towards robust quantum information processing [185]. We also show that the gradual removal of interactions from the system lead to destruction of the robust period two oscillations.

# CHAPTER 6

# Outline

There has been a growing interest in understanding the dynamics of various quantum systems and controlling them to an extent where one can use these systems to realise quantum devices and explore new quantum technologies. Theoretically a lot of work has been done towards this and it is imperative that we experimentally delve deeper into the various properties displayed by these quantum systems and bridge the gap between the existing theoretical work and their demonstration, realisation and verification. In the last few decades Nuclear Magnetic Resonance or NMR has been proven to be a versatile and useful test bed for controlling and manipulating quantum systems, nuclear spins, to explore these new properties. In this thesis we use NMR on nuclear spin clusters to better understand the thermal properties of these driven and non-equilibrium quantum systems and try to throw light over the implications quantum correlations can have over these systems.

We start with a brief description of the pre-requisites for the thesis in Ch. 1. Here we are introduced to the basic understanding of qubits, their properties and the various techniques used in this thesis to control and manipulate them. Based on the concepts introduced in this chapter we start with the first work in Ch. 2. This chapter deals with the preparing and controlling two coupled nuclear spin-1/2 quantum systems to exchange *heat* with each other when coupled via two different types of coupling. We briefly introduce the theoretical work done by Christopher Jarzynski and D. K. Wójcik on exchange fluctuation theorem and experimentally demonstrate the validity of their relation. We also probe into the region of validity of this relation and experimentally demonstrate the breakdown of this relation in strong-coupling regime, as predicted in their original work. We further try to see the effects of quantum correlation in the heat flow between these quantum systems and demonstrate the reversal of *arrow of time* in the presence of certain type of correlation i.e., heat flowing from cold to hot quantum system. As a result we demonstrate the use of quantum correlations as a resource to perform thermodynamic work. In Ch. 3 we further continue to explore the dynamics of heat flow between two quantum systems by experimentally

studying the newly derived thermodynamic uncertainty relations or TURs for out-of-equilibrium quantum systems. These relations provide a bound for the precision of measured quantum heat flow using the entropy produced during the non-equilibrium dynamics. We perform experiments on a two-qubit NMR spin system and measure the heat flow in the presence of different coupling, their strengths and initial preparation of the two quantum systems. We test various theoretical bound put forward in the last few years and experimentally probe the regions validity and violation. These two chapters together provide an in depth study of the thermal process of heat flow in quantum systems which is a step towards realising quantum thermal devices.

Having used quantum correlations in the heat exchange process in the previous chapter, in Ch. 4 we further investigate the localisation of quantum correlation. Just like heat, we try to see how quantum correlation, in our case quantum entanglement, flows and localises in a tripartite spin chain of three qubits. This chapter helps us understand the correlation and their dynamics across coupled systems which can be used for a resource in various quantum thermodynamic process. As most of the thermodynamic processes, of practical interest, take place in the out-of-equilibrium systems, in the last chapter, Ch. 5, of the thesis we investigate a very interesting and recently theoretically predicted quantum many-body property of *time crystalline* behaviour. Here we see how interacting and disordered many-body systems spontaneously break the time translational symmetry and display robust period two oscillations. These systems have very recently been observed experimentally and can be used in implementation of robust gates and operations in quantum systems which are hard to control. Together I believe, this thesis tries to study the thermal properties of these out of equilibrium or driven quantum systems which will be useful towards implementation and development of quantum devices. In future I would like to use the experiences and expertise from these NMR experiments performed on nuclear spin systems and implement them on solid state optical systems like Nitrogen Vacancy centres and work on implementation of quantum thermal devices.

# Bibliography

[1] Richard. P Feynmann. There's plenty of room at the bottom. Caltech Engineering and Science, 34:22–36, 1960.

[2] Frank Arute, Kunal Arya, Ryan Babbush, Dave Bacon, Joseph C Bardin, Rami Barends, Rupak Biswas, Sergio Boixo, Fernando GSL Brandao, David A Buell, et al. Quantum supremacy using a programmable superconducting processor. Nature, 574(7779):505–510, 2019.

[3] Emanuel Knill and Raymond Laflamme. Power of one bit of quantum information. Physical Review Letters, 81(25):5672, 1998.

[4] Tomoyuki Morimae, Keisuke Fujii, and Joseph F Fitzsimons. Hardness of classically simulating the one-clean-qubit model. Physical review letters, 112(13):130502, 2014.

[5] David Deutsch and Richard Jozsa. Rapid solution of problems by quantum computation. Proceedings of the Royal Society of London. Series A: Mathematical and Physical Sciences, 439(1907):553–558, 1992.

[6] P Shor. Proceedings of the 35th annual symposium on the foundations of computer science, ieee. 1994.

[7] M. Nielsen and I. L. Chuang. Quantum Computation and Quantum Information. Cambridge University Press, 2000.

[8] Ivan Oliveira, Roberto Sarthour Jr, Tito Bonagamba, Eduardo Azevedo, and Jair CC Freitas. NMR quantum information processing. Elsevier, 2011.

[9] Adriano Barenco, Charles H Bennett, Richard Cleve, David P DiVincenzo, Norman Margolus, Peter Shor, Tycho Sleator, John A Smolin, and Harald Weinfurter. Elementary gates for quantum computation. Physical review A, 52(5):3457, 1995.

[10] Rolf Landauer. Irreversibility and heat generation in the computing process. IBM journal of research and development, 5(3):183–191, 1961.

[11] Charles H Bennett and Rolf Landauer. The fundamental physical limits of computation. Scientific American, 253(1):48–57, 1985.

[12] Charles H Bennett. Demons, engines and the second law. Scientific American, 257(5):108–117, 1987.

[13] Charles H Bennett. Notes on landauer's principle, reversible computation, and maxwell's demon. Studies In History and Philosophy of Science Part B: Studies In History and Philosophy of Modern Physics, 34(3):501–510, 2003.

[14] Leo Szilard. "U about the decrease in entropy in a thermodynamic system during interventions by intelligent beings. magazine for "u r physics, 53(11-12):840–856, 1929.

[15] Sybren Ruurds De Groot and Peter Mazur. Non-equilibrium thermodynamics. Courier Corporation, 2013.

[16] Antoine Bérut, Artak Arakelyan, Artyom Petrosyan, Sergio Ciliberto, Raoul Dillenschneider, and Eric Lutz. Experimental verification of landauer's principle linking information and thermodynamics. Nature, 483(7388):187–189, 2012.

[17] Shoichi Toyabe, Takahiro Sagawa, Masahito Ueda, Eiro Muneyuki, and Masaki Sano. Experimental demonstration of information-to-energy conversion and validation of the generalized jarzynski equality. Nature physics, 6(12):988–992, 2010.

[18] Sang Wook Kim, Takahiro Sagawa, Simone De Liberato, and Masahito Ueda. Quantum szilard engine. Physical review letters, 106(7):070401, 2011.

[19] Carl M Bender, Dorje C Brody, and Bernhard J Meister. Unusual quantum states: non–locality, entropy, maxwell's demon and fractals. Proceedings of the Royal Society A: Mathematical, Physical and Engineering Sciences, 461(2055):733–753, 2005.

[20] John PS Peterson, Roberto S Sarthour, and Raymond Laflamme. Implementation of a quantum engine fuelled by information. arXiv preprint arXiv:2006.10136, 2020.

[21] Jung Jun Park, Kang-Hwan Kim, Takahiro Sagawa, and Sang Wook Kim. Heat engine driven by purely quantum information. Physical review letters, 111(23):230402, 2013.

[22] Kavan Modi, Tomasz Paterek, Wonmin Son, Vlatko Vedral, and Mark Williamson. Unified view of quantum and classical correlations. Physical review letters, 104(8):080501, 2010.

[23] Harold Ollivier and Wojciech H Zurek. Quantum discord: a measure of the quantumness of correlations. Physical review letters, 88(1):017901, 2001.

[24] Claude Elwood Shannon. A mathematical theory of communication. ACM SIGMOBILE mobile computing and communications review, 5(1):3–55, 2001.

[25] Ingemar Bengtsson and Karol Życzkowski. Geometry of quantum states: an introduction to quantum entanglement. Cambridge university press, 2017.

[26] L Henderson and V Vedral. Classical, quantum and total correlations. Journal of Physics A: Mathematical and General, 34(35):6899–6905, aug 2001.

[27] Asher Peres. Separability criterion for density matrices. Phys. Rev. Lett., 77:1413–1415, Aug 1996.

[28] G. Vidal and R. F. Werner. Computable measure of entanglement. Phys. Rev. A, 65:032314, Feb 2002.

[29] Albert Messiah. Quantum mechanics: volume II. North-Holland Publishing Company Amsterdam, 1962.

[30] D. J. Evans, E. G. D. Cohen, and G. P. Morriss. Probability of second law violations in shearing steady states. Phys. Rev. Lett., 71:2401, 1993.

[31] D. J. Evans and D. J. Searles. Equilibrium microstates which generate second law violating steady states. Phys. Rev. E., 50:1645, 1994.

[32] Giovanni Gallavotti and Ezechiel Godert David Cohen. Dynamical ensembles in stationary states. Journal of Statistical Physics, 80(5):931–970, 1995.

[33] C. Jarzynski. Nonequilibrium equality for free energy differences. Phys. Rev. Lett., 78:2690, 1997.

[34] G. E. Crooks. Entropy production fluctuation theorem and the nonequilibrium work relation for free energy differences. Phys. Rev. E., 60:2721, 1999.

[35] Hal Tasaki. Jarzynski relations for quantum systems and some applications. arXiv preprint cond-mat/0009244, 2000.

[36] Joonhee Choi, Hengyun Zhou, Soonwon Choi, Renate Landig, Wen Wei Ho, Junichi Isoya, Fedor Jelezko, Shinobu Onoda, Hitoshi Sumiya, Dmitry A Abanin, et al. Probing quantum thermalization of a disordered dipolar spin ensemble with discrete time-crystalline order. Physical review letters, 122(4):043603, 2019.

[37] James O'Sullivan, Oliver Lunt, Christoph W Zollitsch, MLW Thewalt, John JL Morton, and Arijeet Pal. Dissipative discrete time crystals. arXiv preprint arXiv:1807.09884, 2018.

[38] John Cavanagh, Wayne J Fairbrother, Arthur G Palmer III, and Nicholas J Skelton. Protein NMR spectroscopy: principles and practice. Elsevier, 1995.

[39] Charles P Slichter. Principles of magnetic resonance, volume 1. Springer Science & Business Media, 2013.

[40] M. H. Levitt. Spin dynamics: basics of nuclear magnetic resonance. John Wiley and Sons, 2001.

[41] GL Long, HY Yan, and Yang Sun. Analysis of density matrix reconstruction in nmr quantum computing. Journal of Optics B: Quantum and Semiclassical Optics, 3(6):376, 2001.

[42] Garett M Leskowitz and Leonard J Mueller. State interrogation in nuclear magnetic resonance quantum-information processing. Physical Review A, 69(5):052302, 2004.

[43] Isaac L Chuang, Neil Gershenfeld, Mark G Kubinec, and Debbie W Leung. Bulk quantum computation with nuclear magnetic resonance: theory and experiment. Proceedings of the Royal Society of London. Series A: Mathematical, Physical and Engineering Sciences, 454(1969):447–467, 1998.

[44] David G Cory, Amr F Fahmy, and Timothy F Havel. Ensemble quantum computing by nmr spectroscopy. Proceedings of the National Academy of Sciences, 94(5):1634–1639, 1997.

[45] Neil A Gershenfeld and Isaac L Chuang. Bulk spin-resonance quantum computation. science, 275(5298):350–356, 1997.

[46] Kavita Dorai, Anil Kumar, et al. Implementing quantum-logic operations, pseudopure states, and the deutsch-jozsa algorithm using noncommuting selective pulses in nmr. Physical Review A, 61(4):042306, 2000.

[47] D. G. Cory, M. D. Price, and T. F. Havel. Nuclear magnetic resonance spectroscopy: An experimentally accessible paradigm for quantum computing. Physica D, 120:82, 1998.

[48] Ushio Sakaguchi, Hiroshi Ozawa, and Toshio Fukumi. Method for effective pure states with any number of spins. Physical Review A, 61(4):042313, 2000.

[49] C. Bustamante, J. Liphardt, and F. Ritort. The nonequilibrium thermodynamics of small systems. Rev. Mod. Phys., 58:43, 2005.

[50] G. Gallavotti and E. G. D. Cohen. Dynamical ensembles in nonequilibrium statistical mechanics. Phys. Rev. Lett., 74:2694, 1995.

[51] D. J. Evans and D. J. Searles. The fluctuation theorem. Adv. Phys., 51:1529, 2002.

[52] C. Jarzynski and D. K. Wöjcik. Classical and quantum fluctuation theorems for heat exchange. Phys. Rev. Lett., 92:230602, 2004.

[53] U. Seifert. Entropy production along a stochastic trajectory and an integral fluctuation theorem. Phys. Rev. Lett., 95:040602, 2005.

[54] S. R. Williams, D. J. Searles, and D. J. Evans. Nonequilibrium free-energy relations for thermal changes. Phys. Rev. Lett., 100:250601, 2008.

[55] D. J. Evans, S. R. Williams, and D. J. Searles. A proof of clausius' theorem for time reversible deterministic microscopic dynamics. J. Chem. Phys., 134:204113, 2011.

[56] M. Esposito, U. Harbola, and S. Mukamel. Nonequilibrium fluctuations, fluctuation theorems, and counting statistics in quantum systems. Rev. Mod. Phys., 81:1665, 2009.

[57] M. Campisi, P. Hänggi, and P. Talkner. Colloquium: Quantum fluctuation relations: Foundations and applications. Rev. Mod. Phys., 83:771, 2011.

[58] P. Hänggi and P. Talkner. The other qft. Nat. Phys., 11:108, 2015.

[59] C. Jarzynski. Equalities and inequalities: Irreversibility and the second law of thermodynamics at the nanoscale. Annu. Rev. Condens. Matter Phys., 2:329, 2011.

[60] K. Saito and Y. Utsumi. Symmetry in full counting statistics, fluctuation theorem, and relations among nonlinear transport coefficients in the presence of a magnetic field. Phys. Rev. B., 78:115429, 2008.

[61] D. Andrieux, P. Gaspard, T. Monnai, and S. Tasaki. The fluctuation theorem for currents in open quantum systems. New. J. Phys., 11:043014, 2009.

[62] U. Seifert. Stochastic thermodynamics, fluctuation theorems, and molecular machines. Rep. Prog. Phys., 75:126001, 2012.

[63] G. Huber, F. Schmidt-Kaler, S. Deffner, and E. Lutz. Employing trapped cold ions to verify the quantum jarzynski equality. Phys. Rev. Lett., 101:070403, 2008.

[64] L. Mazzola, G. De Chiara, , and M. Paternostro. Measuring the characteristic function of the work distribution. Phys. Rev. Lett., 101:070403, 2008.

[65] R. Dorner, S. R. Clark, L. Heaney, R. Fazio, J. Goold, and V. Vedral. Extracting quantum work statistics and fluctuation theorems by single-qubit interferometry. Phys. Rev. Lett., 110:230601, 2013.

[66] M. Campisi, R. Blattmann, S. Kohler, D. Zueco, and P. Hanggi. Employing circuit qed to measure non-equilibrium work fluctuations. New J. Phys., 15:105028, 2013.

[67] J. Goold, U. Poschinger, and K. Modi. Measuring the heat exchange of a quantum process. Phys. Rev. E., 90:020101, 2014.

[68] J. P. S. Peterson, R. S. Sarthour, A. M. Souza, I. S. Oliveira, J. Goold, K. Modi, D. O. Soares-Pinto, and L. C. Céleri. Experimental demonstration of information to energy conversion in a quantum system at the landauer limit. Proc. R. Soc., 472:20150813, 2016.

[69] J. P. S. Peterson, T. B. Batalhäo, M. Herrera, A. M. Souza, R. S. Sarthour, I. S. Oliveira, and R. M. Serra. Experimental characterization of a spin quantum heat engine. Phys. Rev. Lett., 123:240601, 2019.

[70] M. Campisi, P. Talkner, and P. Hänggi. Influence of measurements on the statistics of work performed on a quantum system. Phys. Rev. E., 83:041114, 2011.

[71] G. T. Landi and D. Karevski. Fluctuations of the heat exchanged between two quantum spin chains. Phys. Rev. E., 93:032122, 2016.

[72] J. Teles, E. R. DeAzevero, J. C. C. Freitas, R. S. Sarthour, I. S. Oliveira, and T. J. Bonagamba. Quantum information processing by nuclear magnetic resonance on quadrupolar nuclei. Phil. Trans. R. Soc. A, 370:4770, 2012.

[73] N. Khaneja and et al. Optimal control of coupled spin dynamics: Design of nmr pulse sequences by gradient ascent algorithms. J. Magn. Res., 172.2:296 – 305, 2005.

[74] VS Manu and Anil Kumar. Singlet-state creation and universal quantum computation in nmr using a genetic algorithm. Physical Review A, 86(2):022324, 2012.

[75] A. Abragam and W. G. Proctor. Spin temperature. Phys. Rev., 109:1441, 1958.

[76] P. Solinas and S. Gasparinetti. Probing quantum interference effects in the work distribution. Phys. Rev. A., 94:052103, 2016.

[77] M. P.-Llobet, E. Bäumer, K. V. Hovhannisyan, M. Huber, and A. Acin. No-go theorem for the characterization of work fluctuations in coherent quantum systems. Phys. Rev. Lett., 118:070601, 2017.

[78] K. Micadei, J. P. S. Peterson, A. M. Souza, R. S. Sarthour, I. S. Oliveira, G. T. Landi, T. B. Batalh ao, R. M. Serra, and E. Lutz. Reversing the direction of heat flow using quantum correlations. Nat. Commun., 10:2456, 2019.

[79] H. M. Friedman, B. K. Agarwalla, O. Shein-Lumbroso, O. Tal, and D. Segal. Thermodynamic uncertainty relation in atomic-scale quantum conductors. Phys. Rev. B., 101:195423, 2020.

[80] A. C. Barato and U. Seifert. Thermodynamic uncertainty relation for biomolecular processes. Phys. Rev. Lett., 114:158101, Jun 2015.

[81] Todd R. Gingrich, Jordan M. Horowitz, Nikolay Perunov, and Jeremy L. England. Dissipation bounds all steady-state current fluctuations. Phys. Rev. Lett., 116:120601, 2016.

[82] M. Polettini, A. Lazarescu, and M. Esposito. Tightening the uncertainty principle for stochastic currents. Phys. Rev. E., 94:052104, 2016.

[83] P. Pietzonka, A. C. Barato, and U. Seifert. Universal bounds on current fluctuations. Phys. Rev. E., 93:052145, 2016.

[84] C. Hyeon and W. Hwang. Physical insight into the thermodynamic uncertainty relation using brownian motion in tilted periodic potentials. Phys. Rev. E., 96:012156, 2017.

[85] J. M. Horowitz and T. R. Gingrich. Proof of the finite-time thermodynamic uncertainty relation for steady-state currents. Phys. Rev. E., 96:020103, 2017.

[86] K. Proesmans and C. V. den Broeck. Discrete-time thermodynamic uncertainty relation. EPL, 119:20001, 2017.

[87] T. R. Gingrich, G. M. Rotskoff, and J. M Horowitz. Inferring dissipation from current fluctuations. J.Phys. A: Math. Theor., 50:184004, 2017.

[88] P. Pietzonka, F. Ritort, and U. Seifert. Finite-time generalization of the thermodynamic uncertainty relation. Phys. Rev. E., 95:012101, 2017.

[89] J. P. Garrahan. Simple bounds on fluctuations and uncertainty relations for first-passage times of counting observables. Phys. Rev. E., 95:032134, 2017.

[90] A. Dechant. Multidimensional thermodynamic uncertainty relations. J. Phys. A: Math. Theor., 52:035001, 2019.

[91] G. Falasco, M. Esposito, and J.-C. Delvenne. Unifying thermodynamic uncertainty relations. New J. Phys., 22, 2020.

[92] P. P. Potts and P. Samuelsson. Thermodynamic uncertainty relations including measurement and feedback. Phys. Rev. E., 100:052137, 2019.

[93] T. Koyuk, U. Seifert, , and P. Pietzonka. A generalization of the thermodynamic uncertainty relation to periodically driven systems. J. Phys. A: Math. Theor., 52:02LT02, 2018.

[94] Katarzyna Macieszczak, Kay Brandner, and Juan P. Garrahan. Unified thermodynamic uncertainty relations in linear response. Phys. Rev. Lett., 121:130601, 2018.

[95] A. Dechant and S i. Sasa. Current fluctuations and transport efficiency for general langevin systems. J. Stat. Mech., page 063209, 2018.

[96] I. Di Terlizzi and M. Baiesi. Kinetic uncertainty relation. J. of Phys. A: Math. and Theor., 52:02LT03, 2018.

[97] H.-M. Chun, L. P. Fischer, and U. Seifert. Effect of a magnetic field on the thermodynamic uncertainty relation. Phys. Rev. E., 99:042128, 2019.

[98] S. Kheradsoud, N. Dashti, M. Misiorny, P. P. Potts, J. Splettstoesser, and P. Samuelsson. Power, efficiency and fluctuations in a quantum point contact as steady-state thermoelectric heat engine. Entropy, 21:777, 2019.

[99] G. Guarnieri, G. T. Landi, S. R. Clark, and J. Goold. Thermodynamics of precision in quantum non-equilibrium steady states. Phys. Rev. Research, 1:033021, 2019.

[100] A. C. Barato, R. Chetrite, A. Faggionato, and D. Gabrielli. Bounds on current fluctuations in periodically driven systems. New J. Phys., 20:103023, 2018.

[101] Yoshihiko Hasegawa and Tan Van Vu. Fluctuation theorem uncertainty relation. Phys. Rev. Lett., 123:110602, 2019.

[102] Y. Hasegawa and T. V. Vu. Uncertainty relations in stochastic processes: An information inequality approach. Phys. Rev. E., 99:062126, 2019.

[103] M. L. Rosinberg and G. Tarjus. Comment on thermodynamic uncertainty relation for time-delayed langevin systems. arXiv preprint arXiv:1810.12467, 2018.

[104] K. Brandner, T. Hanazato, and K. Saito. Thermodynamic bounds on precision in ballistic multiterminal transport. Phys. Rev. Lett., 120:090601, 2018.

[105] D. Gupta and A. Maritan. Thermodynamic uncertainty relations in a linear system. Eur. Phys. J. B, 93:28, 2020.

[106] K. Ptaszynski. Coherence-enhanced constancy of a quantum thermoelectric generator. Phys. Rev. B., 98:085425, 2018.

[107] B. K. Agarwalla and D. Segal. Assessing the validity of the thermodynamic uncertainty relation in quantum systems. Phys. Rev. B., 98:155438, 2018.

[108] J. Liu and D. Segal. Thermodynamic uncertainty relation in quantum thermoelectric junctions. Phys. Rev. E., 99:062141, 2019.

[109] J. M. Horowitz and T. R. Gingrich. Thermodynamic uncertainty relations constrain nonequilibrium fluctuations. Nat. Phys., 16:15–20, 2020.

[110] Simone Pigolotti, Izaak Neri, Édgar Roldán, and Frank Jülicher. Generic properties of stochastic entropy production. Phys. Rev. Lett., 119:140604, 2017.

[111] A. M. Timpanaro, G. Guarnieri, J. Goold, and G. T. Landi. Thermodynamic uncertainty relations from exchange fluctuation theorems. Phys. Rev. Lett., 123:090604, 2019.

[112] H. Vroylandt, K. Proesmans, , and T. R. Gingrich. Isometric uncertainty relations. Journal of Statistical Physics, 178:1039–1053, 2020.

[113] W. Hwang and C. Hyeon. Energetic costs, precision, and transport efficiency of molecular motors. J. Phys. Chem. Lett., 9:513, 2018.

[114] M. Shreshtha and R. J. Harris. Thermodynamic uncertainty for run-and-tumble-type processes. EPL, 126:40007, 2019.

[115] R. Marsland III, W. Cui, and J. M. Horowitz. The thermodynamic uncertainty relation in biochemical oscillations. J. R. Soc. Interface, 16, 2019.

[116] S. Lee, C. Hyeon, and J. Jo. Thermodynamic uncertainty relation of interacting oscillators in synchrony. Phys. Rev. E., 98:032119, 2018.

[117] T. Van Vu and Y. Hasegawa. Uncertainty relation in the presence of information measurement and feedback control. arXiv preprint arXiv:1904.04111, 2019.

[118] K. Proesmans and J. M. Horowitz. Hysteretic thermodynamic uncertainty relation for systems with broken time-reversal symmetry. J. Stat. Mech., page 054005.

[119] S. Saryal, H. Friedman, D. Segal, and B. K. Agarwalla. Thermodynamic uncertainty relation in thermal transport. Phys. Rev. E., 100:042101, 2019.

[120] Todd R. Gingrich and Jordan M. Horowitz. Fundamental bounds on first passage time fluctuations for currents. Phys. Rev. Lett., 119:170601, 2017.

[121] Y. Hasegawa and T. Van Vu. Fluctuation theorem uncertainty relation. Phys. Rev. Lett., 123:110602, 2019.

[122] M. J. Hall L. Li and H. M. Wiseman. Concepts of quantum non-markovianity: A hierarchy. Phys. Rep., 759:1–51, 2018.

[123] S. Pal, T. S. Mahesh, and B. K. Agarwalla. Experimental demonstration of the validity of the quantum heat-exchange fluctuation relation in an nmr setup. Phys. Rev. A., 100:042119, 2019.

[124] B. K. Agarwalla, H. Li, B. Li, and J.-S. Wang. Exchange fluctuation theorem for heat transport between multiterminal harmonic systems. Phys. Rev. E., 89:052101, 2014.

[125] B. K. Agarwalla, B. Li, and J.-S. Wang. Full-counting statistics of heat transport in harmonic junctions: Transient, steady states, and fluctuation theorems. Phys. Rev. E., 85:051142, 2012.

[126] K. Saito and A. Dhar. Fluctuation theorem in quantum heat conduction. Phys. Rev. Lett., 99:180601, 2007.

[127] T. Denzler and E. Lutz. Heat distribution of a quantum harmonic oscillator. Phys. Rev. E., 98:051142, 2018.

[128] B. B. Wei. Relations between heat exchange and rényi divergences. Phys. Rev. E., 97:042107, 2018.

[129] Soham Pal, Sushant Saryal, Dvira Segal, T. S. Mahesh, and Bijay Kumar Agarwalla. Experimental study of the thermodynamic uncertainty relation. Phys. Rev. Research, 2:022044(R), 2020.

[130] R. Horodecki, P. Horodecki, M. Horodecki, and K. Horodecki. Quantum entanglement. Rev. Mod. Phys., 81(2):865, 2009.

[131] T. S. Cubitt, F. Verstraete, W. Dür, and J. I. Cirac. Separable states can be used to distribute entanglement. Phys. Rev. Lett., 91(3):037902, 2003.

[132] X.-D. Yang, A.-M. Wang, X.-S. Ma, F. Xu, H. You, and W.-Q. Niu. Experimental creation of entanglement using separable states. Chin. Phys. Lett., 22(2):279, 2005.

[133] A. Fedrizzi, M. Zuppardo, G. G. Gillett, M. A. Broome, M. Almeida, M. Paternostro, A. White, and T. Paterek. Experimental distribution of entanglement with separable carriers. Phys. Rev. Lett., 111(23):230504, 2013.

[134] C. E. Vollmer, D. Schulze, T. Eberle, V. Händchen, J. Fiurášek, and R. Schnabel. Experimental entanglement distribution by separable states. Phys. Rev. Lett., 111(23):230505, 2013.

[135] C. Peuntinger, V. Chille, L. Mista, N. Korolkova, M. Förtsch, J. Korger, C. Marquardt, and G. Leuchs. Distributing entanglement with separable states. Phys. Rev. Lett., 111(23):230506, 2013.

[136] A. Streltsov, H. Kampermann, and D. Bruß. Quantum cost for sending entanglement. Phys. Rev. Lett., 108(25):250501, 2012.

[137] T. K. Chuan, L. Maillard, K. Modi, T. Paterek, M. Paternostro, and M. Piani. Quantum discord bounds the amount of distributed entanglement. Phys. Rev. Lett., 109(7):070501, 2012.

[138] A. Streltsov, H. Kampermann, and D. Bruß. Limits for entanglement distribution with separable states. Phys. Rev. A, 90:032323, 2014.

[139] A. Streltsov, R. Augusiak, M. Demianowicz, and M. Lewenstein. Progress towards a unified approach to entanglement distribution. Phys. Rev. A, 92:012335, 2015.

[140] M. Zuppardo, T. Krisnanda, T. Paterek, S. Bandyopadhyay, A. Banerjee, P. Deb, S. Halder, K. Modi, and M. Paternostro. Excessive distribution of quantum entanglement. Phys. Rev. A, 93:012305, 2016.

[141] A. Streltsov, H. Kampermann, and D. Bruß. Lectures on general quantum correlations and their applications, chapter Entanglement distribution and quantum discord. Springer International Publishing, 2017.

[142] Leah Henderson and Vlatko Vedral. Classical, quantum and total correlations. Journal of physics A: mathematical and general, 34(35):6899, 2001.

[143] Harold Ollivier and Wojciech H Zurek. Quantum discord: a measure of the quantumness of correlations. Phys. Rev. Lett., 88(1):017901, 2001.

[144] K. Modi, A. Brodutch, H. Cable, T. Paterek, and V. Vedral. The classical-quantum boundary for correlations: discord and related measures. Rev. Mod. Phys., 84:1655, 2012.

[145] T. Krisnanda, M. Zuppardo, M. Paternostro, and T. Paterek. Revealing nonclassicality of inaccessible objects. Phys. Rev. Lett., 119:120402, 2017.

[146] C. H. Bennett, D. P. DiVincenzo, J. A. Smolin, and W. K. Wootters. Mixed-state entanglement and quantum error correction. Phys. Rev. A, 54:3824, 1996.

[147] Soham Pal, Priya Batra, Tomasz Paterek, and TS Mahesh. Experimental localisation of quantum entanglement through monitored classical mediator. arXiv preprint arXiv:1909.11030, 2020.

[148] Tanjung Krisnanda. Distribution of quantum entanglement: Principles and applications. arXiv:2003.08657., 2020.

[149] W. Y. Kon, T. Krisnanda, P. Sengupta, and T. Paterek. Nonclassicality of spin structures in condensed matter: An analysis of sr 14 cu 24 o 41. Physical Review B, 100(23):235103, 2019.

[150] S. Bose, A. Mazumdar, G. W. Morley, H. Ulbricht, M. Toros, M. Paternostro, A. A. Geraci, P. F. Barker, M. S. Kim, and G. Milburn. Spin entanglement witness for quantum gravity. Phys. Rev. Lett., 119:240401, 2017.

[151] C. Marletto and V. Vedral. Gravitationally induced entanglement between two massive particles is sufficient evidence of quantum effects in gravity. Phys. Rev. Lett., 119:240402, 2017.

[152] T. Krisnanda, C. Marletto, V. Vedral, M. Paternostro, and T. Paterek. Probing quantum features of photosynthetic organisms. npj Quant. Inf., 4:60, 2018.

[153] V. Vedral and M. B. Plenio. Entanglement measures and purification procedures. Phys. Rev. A, 57:1619, 1998.

[154] L. Gyongyosi. The correlation conversion property of quantum channels. Quant. Inf. Process., 13:467, 2014.

[155] G. Vidal and R. F. Werner. Computable measure of entanglement. Phys. Rev. A, 65:032314, 2002.

[156] V. Vedral, M. B. Plenio, M. A. Rippin, and P. L. Knight. Quantifying entanglement. Phys. Rev. Lett., 78:2275, 1997.

[157] B. Groisman, S. Popescu, and A. Winter. On the quantum, classical and total amount of correlations in a quantum state. Phys. Rev. A, 72:032317, 2005.

[158] K. Modi, T. Paterek, W. Son, V. Vedral, and M. Williamson. Unified view of quantum and classical correlations. Phys. Rev. Lett., 104:080501, 2010.

[159] J. Cavanagh, W. J. Fairbrother, A. G. Palmer, and N. J. Skelton. Protein NMR spectroscopy: Principles and practice. Elsevier, 1995.

[160] Avik Mitra, K. Sivapriya, and Anil Kumar. Experimental implementation of a three qubit quantum game with corrupt source using nuclear magnetic resonance quantum information processor. J. Magn. Res., 187.2(2):306–313, 2007.

[161] H. Katiyar, A. Shukla, R. K. Rao, and T. S. Mahesh. Violation of entropic leggett-garg inequality in nuclear spins. Phys. Rev. A, 87:052102, 2013.

[162] Priya Batra, VR Krithika, and TS Mahesh. Push-pull optimization of quantum controls. Physical Review Research, 2(1):013314, 2020.

[163] A. Shukla, K. R. K. Rao, and T. S. Mahesh. Ancilla-assisted quantum state tomogarphy in multiqubit registers. Phys. Rev. A, 87:062317, 2013.

[164] S. L. Braunstein, C. M. Caves, R. Jozsa, N. Linden, S. Popescu, and R. Schack. Separability of very noisy mixed states and implications for nmr quantum computing. Phys. Rev. Lett., 83:1054, 1999.

[165] A. Al Balushi, W. Cong, and R. B. Mann. Optomechanical quantum cavendish experiment. Phys. Rev. A, 98:043811, 2018.

[166] S. Qvarfort, S. Bose, and A. Serafini. Mesoscopic entanglement from central potential interactions. arXiv:1812.09776, 2018.

[167] T. Krisnanda, G. Y. Tham, M. Paternostro, and T. Paterek. Observable quantum entanglement due to gravity. npj Quant. Inf., 6:12, 2020.

[168] Frank Wilczek. Quantum time crystals. Phys. Rev. Lett., 109:160401, Oct 2012.

[169] Patrick Bruno. Comment on "quantum time crystals". Phys. Rev. Lett., 110:118901, Mar 2013.

[170] Haruki Watanabe and Masaki Oshikawa. Absence of quantum time crystals. Phys. Rev. Lett., 114:251603, Jun 2015.

[171] Vedika Khemani, Achilleas Lazarides, Roderich Moessner, and S. L. Sondhi. Phase structure of driven quantum systems. Phys. Rev. Lett., 116:250401, Jun 2016.

[172] Dominic V. Else, Bela Bauer, and Chetan Nayak. Floquet time crystals. Phys. Rev. Lett., 117:090402, Aug 2016.

[173] C. W. von Keyserlingk, Vedika Khemani, and S. L. Sondhi. Absolute stability and spatiotemporal long-range order in floquet systems. Phys. Rev. B, 94:085112, Aug 2016.

[174] N. Y. Yao, A. C. Potter, I.-D. Potirniche, and A. Vishwanath. Discrete time crystals: Rigidity, criticality, and realizations. Phys. Rev. Lett., 118:030401, Jan 2017.

[175] J. Zhang, P. W. Hess, A. Kyprianidis, P. Becker, A. Lee, J. Smith, G. Pagano, I.-D. Potirniche, A. C. Potter, A. Vishwanath, N. Y. Yao, and C. Monroe. Observation of a discrete time crystal. Nature, 543(7644):217–220, mar 2017.

[176] Soonwon Choi, Joonhee Choi, Renate Landig, Georg Kucsko, Hengyun Zhou, Junichi Isoya, Fedor Jelezko, Shinobu Onoda, Hitoshi Sumiya, Vedika Khemani, Curt von Keyserlingk, Norman Y. Yao, Eugene Demler, and Mikhail D. Lukin. Observation of discrete time-crystalline order in a disordered dipolar many-body system. Nature, 543(7644):221–225, mar 2017.

[177] Wen Wei Ho, Soonwon Choi, Mikhail D. Lukin, and Dmitry A. Abanin. Critical time crystals in dipolar systems. Phys. Rev. Lett., 119:010602, Jul 2017.

[178] Jared Rovny, Robert L Blum, and Sean E Barrett. Observation of discrete time-crystalline signatures in an ordered dipolar many-body system. arXiv preprint arXiv:1802.00126, 2018.

[179] Varad R. Pande, Gaurav Bhole, Deepak Khurana, and T. S. Mahesh. Strong algorithmic cooling in large star-topology quantum registers. Phys. Rev. A, 96:012330, Jul 2017.

[180] Dominic V. Else, Bela Bauer, and Chetan Nayak. Prethermal phases of matter protected by time-translation symmetry. Phys. Rev. X, 7:011026, Mar 2017.

[181] Dmitry A. Abanin, Wojciech De Roeck, and Fran çois Huveneers. Exponentially slow heating in periodically driven many-body systems. Phys. Rev. Lett., 115:256803, Dec 2015.

[182] Achilleas Lazarides and Roderich Moessner. Fate of a discrete time crystal in an open system. Phys. Rev. B, 95:195135, May 2017.

[183] IJ Lowe. Nuclear magnetic resonance spectra from a crystal rotated at high speed. Phys. Rev. Lett, 2:285–287, 1959.

[184] SR Hartmann and EL Hahn. Nuclear double resonance in the rotating frame. Physical Review, 128(5):2042, 1962.

[185] Soonwon Choi, Norman Y Yao, and Mikhail D Lukin. Quantum metrology based on strongly correlated matter. arXiv preprint arXiv:1801.00042, 2018.